DISCLAIMER OF QUALITY

Due to the condition of the original material, there are unavoidable flaws in this reproduction. We have made every effort possible to provide you with the best copy available. If you are dissatisfied with this product and find it unusable, please contact Document Services as soon as possible.

Thank you.

Pages are missing from the original document.

PAGE 43 IS MISSING

PAGE 61 IS MISSING

A STUDY OF THE SOLAR WIND FROM THE VOYAGER SPACECRAFT, 1977-1992

by

Louis Villanueva

B.S., Physics, Mathematics, Statistics
California State University, Hayward, 1987

Submitted to the Department of
Physics in Partial Fulfillment of
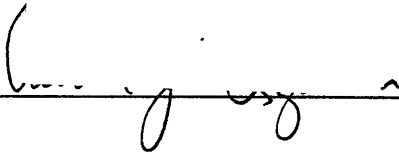the Requirements for the
Degree of

DOCTOR OF PHILOSOPHY
in Physics
at the

Massachusetts Institute of Technology

February, 1994

Signature of Author _____
<div align="right">Department of Physics
February 15, 1994</div>

Certified by _____
<div align="right">Alan J. Lazarus
Senior Research Scientist
Thesis Supervisor</div>

Accepted by _____
<div align="right">George F. Koster, Chairman
Graduate Committee
Department of Physics</div>

1

A STUDY OF THE SOLAR WIND FROM THE VOYAGER SPACECRAFT, 1977-1992

by

Louis Villanueva

ABSTRACT

A reanalysis was performed on the solar wind ion data from the Plasma Science (PLS) Instrument on each of the Voyager 1 and the Voyager 2 spacecraft. The analysis was carried out using an automated fitting routine created by the author. While the solar wind number density was confirmed to be proportional to r^{-2}, where r is the heliocentric distance, it was discovered that the thermal speed was proportional to $r^{-1/3}$. No systematic variation with distance was seen in the velocity.

Temporal variation in the solar wind parameters was sought using 11 years of Voyager data. The most prominent periods detected were 25.4 days (solar sidereal rotation) and 146.3 days which appears not to be correlated with observations of other solar phenomena.

The reanalysis included a program for detecting proton double streaming. The behavior of double streaming protons was compared to that of single stream protons and alpha particles. It is was found that the magnitude of the velocity difference between double streaming protons can be as large as twice the Alfvén speed. This is in contrast to alpha particles and protons whose difference in speed is bounded by the Alfvén speed.

Finally, it was discovered that the PLS instrument was capable of clearly detecting other ions, namely O^{+6} and O^{+7} during times of cool, low-speed, high density, plasma streams. The total oxygen flux densities were found to deviate from a linear relation with the alpha particle flux densities at low fluxes. Using the ratio of the O^{+6} and O^{+7} number densities, the author computed a temperature for the solar corona of 1.7×10^6 K, which is in good agreement with that found by others.

Thesis Supervisor: Dr. Alan J. Lazarus

Title: Senior Research Scientist

TABLE OF CONTENTS

Chapt 1

plas5:lav

Troff

Tue Feb 15 23:04:30 1994

lw664a / Plasma LW Plus (37-664)

```
lw664a plas5:lav  Job: Troff  Date: Tue Feb 15 23:04:30 1994

lw664a plas5:lav  Job: Troff  Date: Tue Feb 15 23:04:30 1994

lw664a plas5:lav  Job: Troff  Date: Tue Feb 15 23:04:30 1994

lw664a plas5:lav  Job: Troff  Date: Tue Feb 15 23:04:30 1994
```

Still need Fig #.4

CHAPTER 1

INTRODUCTION

1.1. The Solar Wind[1]

The Sun is a massive, luminous ball of gas. It is composed of about 90% hydrogen (by number) and 10% helium with a small fraction of heavier elements, such as carbon, oxygen, and iron. Within a region about 0.3 solar radii from the center of the Sun, the temperature and density are high enough (~10^7 K and 100 g/cm^3) to promote fusion of protons into helium nuclei. The energy released from this process diffuses outward as "hard" X-rays which are degraded into radiation of longer wavelengths by continuous absorption and emission of the photons by the gas surrounding the core. Above a distance of about 0.7 solar radii from the center, diffusion is not fast enough to transport energy out of the Sun so it is carried away by convection. As the hot gas rises, it becomes less dense until it is finally transparent, and the transported energy is radiated out into space. The region where is energy radiation occurs is the photosphere which is regarded as the visible surface of the Sun (Figure 1.1).

Above the photosphere lies a layer of transparent gas called the chromosphere (from the Greek *chroma*, meaning color). The chromosphere is so much dimmer than the photosphere that it can be seen only with the aid of a coronagraph (a device that uses

---

1 The information for Section 1.1 was taken from "Acceleration of the Solar Wind" by Aaron Barnes, *Reviews of Geophysics, 30,* 1/ February 1992.
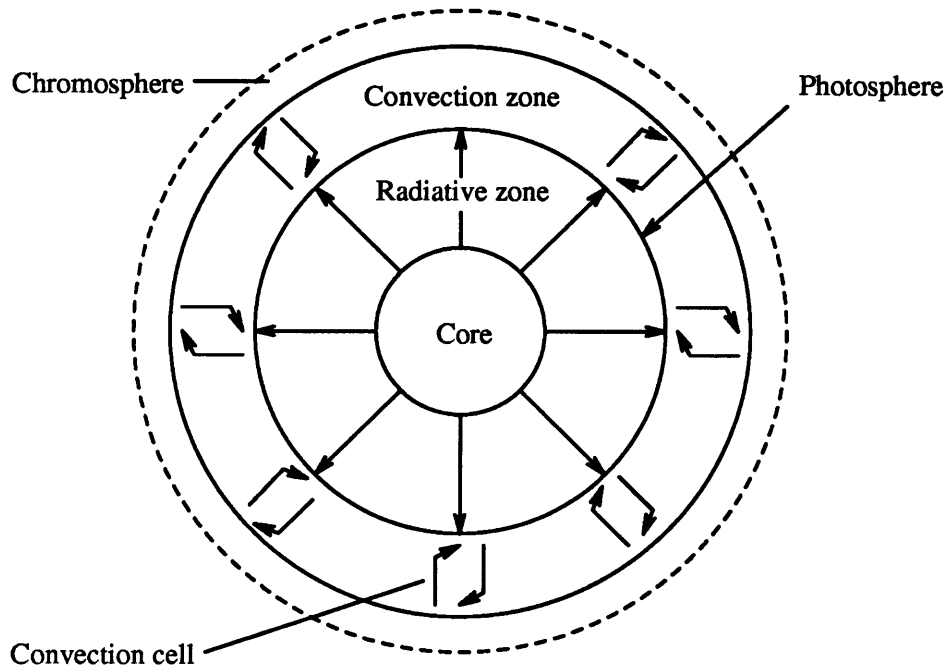
Figure 1.1. Diagram of the solar interior and the outer layers. Not explicitly shown in this schematic is the corona which extends many solar radii above the chromosphere.

a disk to occult the photosphere) or during a total eclipse of the Sun when it appears as a reddish fringe just beyond the Moon.

Above the chromosphere lies the corona (meaning "crown" in Latin). Like the chromosphere it is visible only with a coronagraph or during a total solar eclipse. It appears as a pearly white structure, parts of which can extend several solar radii from the edge of the Sun. The coronal temperature ranges from 1 to 2×10^6 K, and it is therefore a highly ionized plasma. As an example, spectral lines from iron with up to 12 electrons removed have been observed, and the lightest elements are fully ionized. Despite the corona's high temperature, it is not very dense (more of a "hot vacuum" by terrestrial standards) and a black body placed into the coronal gas and shielded

4

from the solar radiation would reradiate the heat absorbed from the gas at an equilibrium temperature range of 600 to 2000 K since the corona is optically thin.

The corona is a highly structured region of plasma. This structure is imposed by the solar magnetic field which extends from the solar surface out into the corona. Since the corona is a plasma, it is an excellent electrical conductor. As a result of this conductivity, the coronal plasma can move along but not across magnetic field lines. There are two types of magnetic field lines, "closed" and "open". Closed field lines are anchored at two points in the photosphere and extend into the corona as a loop or arch (a visible manifestation of these magnetic field loops can be seen in the motion of solar prominences). Open field lines are anchored at only one point in the photosphere and extend into interplanetary space. It is in these open field regions that the corona can expand outward in the form of the solar wind (Figure 1.2).

Open field lines
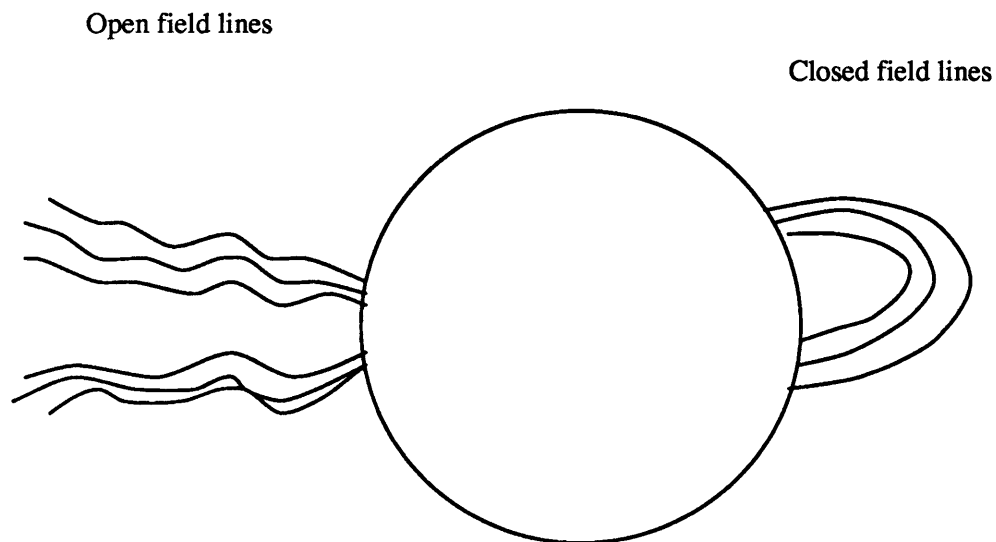
Closed field lines

Figure 1.2.   Two types of solar magnetic field lines. Closed field lines confine coronal plasma to the Sun. Open field lines allow the plasma to escape to become the solar wind.

The expanding coronal gas or solar wind fills interplanetary space. The solar magnetic fields embedded in the plasma are carried into space by the solar wind to form the interplanetary magnetic field (IMF). Beyond some 15-20 solar radii, the solar magnetic field is dominated by the solar wind flow which expands almost radially away from the Sun. Because of solar rotation, the point where the open field line is anchored to the Sun moves and as a result the interplanetary magnetic field has the form of a spiral (This spiral pattern is not unlike the one seen for water emanating from a rotating garden sprinkler). At the orbit of the Earth, one astronomical unit (AU) or about 1.5×10^8 km from the Sun, the interplanetary magnetic field makes an angle of about 45° to the radial direction. Further out the field is nearly transverse (i.e. ~90°) to the radial direction (Figure 1.3).
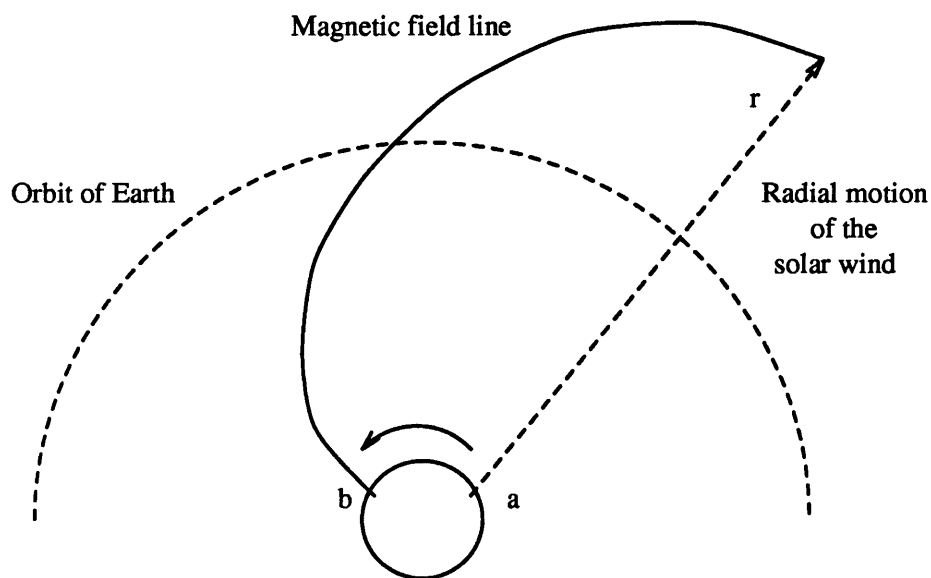
Figure 1.3.   Spiral structure of a magnetic field line. A parcel of solar wind eminates from the Sun (at a) dragging a magnetic field line with it. When the solar wind has moved out a distance, r, the anchor point of the field has moved to b which caused the field line to form an Archimedean spiral.

6

At 1 AU the average speed of the solar wind is about 400 km/s. This speed is by no means constant. The solar wind can reach speeds in excess of 900 km/s and can travel as slowly as 300 km/s. The average density of the solar wind at 1 AU is about 10 protons/cm^3 with large variations[2]. The solar wind confines the magnetic field of Earth and governs phenomena such as geomagnetic storms and aurorae. The solar wind confines the magnetic fields of other planets as well. As the solar wind expands, its density decreases as the inverse of the square of its distance from the Sun. At some large enough distance from the Sun (in a region known as the heliopause), the solar wind can no longer "push back" the fields and particles of the local interstellar medium and the solar wind slows down from 400 km/s to perhaps 20 km/s. The location of this transition region (called the heliospheric termination shock) is unknown at the present time, but from direct spacecraft measurements must be at more than 50 AU. In fact, recent observations of 3 kHz radiation from Voyagers 1 and 2 have been interpreted as coming from a radio burst at the termination shock. This burst is thought to have been triggered by an event in the solar wind observed by Voyager 2. From the time delay between this triggering event and the observation of the 3 kHz radiation, the distance of the termination shock has been put between 130 and 170 AU [*Gurnett et al.*, 1993]. Voyager 2 is currently heading away from the plane of the ecliptic and hopefully will encounter the termination shock before all contact with the spacecraft is lost by the year 2010.

---

2 The author finds that this average value is ~7cm^{-3}

1.2. The Voyager Spacecraft

In 1977, two spacecraft were launched toward the planet Jupiter. Voyager 2 was launched on August 20th, and Voyager 2 was launched on September 5th. Both space-craft encountered Jupiter in 1979. In 1980 Voyager 1 encountered Saturn and was deflected northward out of the plane of the ecliptic. In 1981 Voyager 2 also encountered Saturn and later went on to encounter Uranus in 1986 and Neptune in 1989. At Neptune, Voyager 2 was deflected southward from the ecliptic plane. At the time of this work the spacecraft is over 40 AU from the Sun, and it is continues to transmit data for analysis.

Between planetary encounters, the two spacecraft measured (and Voyager 2 still measures) the distribution of particles and magnetic fields in the solar system. This thesis is concerned with the positive ions that comprise the solar wind.

1.3. The Voyager Instrument

Each Voyager plasma science (PLS) instrument consists of four modulated Faraday cups, three of which (the A, B, and C cups) form the main sensor and are clustered around the spacecraft axis that points toward Earth and The main sensor is used for measurements of the solar wind (Figure 1.4). The fourth cup is oriented at right angles to the main sensor and is used to detect solar wind electrons and ions in plane-tary magnetospheres during encounters [*Bridge et al.*, 1977]. The normals of the main sensor cups are separated in azimuth by 120° and lie on a cone that makes a 20° angle with the Earth-pointing axis. The three cups allow determination of the components of

8

velocity along their normals, hence the determination of the velocity vector itself. The PLS instrument is an electrostatic analyzer and thus can establish only the energy per charge, E/q, of the ions it measures.

The Faraday cups of the main sensor have a series of nine wire-mesh "grids" that cover the aperture of each cup. A retard-

Figure 1.4. The PLS Instrument

ing potential is placed across some of the grids in a step wise manner. Only those ions whose kinetic energy exceeds the ion charge times the grid potential are allowed to enter the cup.

There are two modes of ion data: the low-resolution or L-mode data and the high-resolution M-mode data[3]. The energy steps for the L-mode spectra are rather large with an energy resolution of ~29%, whereas the M-mode spectra have an energy resolution of about 3.6%. There are also two modes of electron data E1 and E2, but this work is concerned exclusively with ion data from the M-mode and will not deal with electrons.

The Voyager data consists of current spectra that are a measure of the number of the various ions or electrons within some energy (or speed) interval. The Voyager

3 The initial plan was to have three modes for the ion data, L, M, and H (for low, medium, and high resolution). Unfortunately, creating an instrument with an energy resolution of ~1% proved untenable due to the energy spreads caused by the grids. So the M-mode became the high resolution mode.

spacecraft are capable of taking a spectrum once every 12 to 192 seconds.

The Voyager PLS experiment is capable of identifying protons and alpha particles in the solar wind. The instrument can also identify O^{+6} when the proton Mach number (ratio of solar wind proton bulk speed to proton thermal speed) is greater than ~15 but cannot in general separate O^{+7} from N^{+6} and C^{+5} (mass to charge ratios M/Q of 2.29, 2.33, and 2.40 respectively). In this respect, the Voyager PLS performance is comparable to that of the low-resolution M/Q mode of the ion composition instrument on ISEE 3 (3.6% in the range of 1.4 < M/Q < 5.8, see *Bochsler et al.* [1985]). If the solar wind is too warm, the widths of the He^{+2} and the unresolved O^{+7}, N^{+6}, and C^{+5} velocity distributions become so great that they mask the presence of the O^{+6} distribution (see Chapter 4).

The Voyager 1 PLS instrument suffered a temporary in-flight failure during the period between days 48 and 140 of 1978 resulting in a data gap during that period. Data from both Voyager instruments obtained after the Jupiter encounters (March and July of 1979 for Voyagers 1 and 2, respectively) exhibit increased noise levels at low ion fluxes, presumably as a result of the penetrating radiation in the Jovian magnetosphere (although the mechanism has never been identified). In addition, the noise is also worse in the spacecraft operational mode employed for planetary encounters and during much of the Jupiter to Saturn cruise. The noise causes some problems with the automated analysis described in Chapter 4.

After the Saturn encounter, the Voyager 1 instrument suffered a major failure on day

328 of 1980 and no useful data have been received from it since then. The Voyager 2 instrument has continued to function well up to the present time, nearly 17 years since launch. Protons are routinely measured, and solar wind alpha particles are detectable in regions of higher density. Even O^{+6} can be measured by averaging spectra.

1.4. The Voyager Data

This work is a result of a reanalysis of solar wind data from the Voyager 1 and Voyager 2 spacecraft. The data set consists of ~250,000 high resolution (M-mode) ion spectra taken 12 minutes apart (~25% of the all M-mode spectra). These data cover a time interval from day 250 of 1977 to day 365 of 1979 for Voyager 1 and from day 234 of 1977 to day 249 of 1989 for Voyager 2. Essential to the analysis has been the creation of an automated program which can process a year's worth of spectra in a day. The main part of the thesis is divided into three sections which are described below:

This work uses the results based on an abridged data set. This set consists entirely of M-mode spectra taken every 12 minutes apart. Although this is only about one-quarter of the total number of Voyager M-mode spectra, there still should be about 500,000 spectra to analyze. However, problems such as decreasing tracking coverage reduce this number to approximately 250,000.

The first part of the analysis consists of identifying the various ions in the spectra and their parameters. This is accomplished by assuming the ions of the solar wind are in a state of thermal equilibrium and therefore follow the Maxwell velocity distribution.

There are spectra clearly showing ions that are not Maxwellian distributed. In such cases, the non-Maxwellian distribution can be considered to be the sum of two (in some cases three) Maxwellian distributions.

With the assumption of Maxwellian distributions, one can compute parameters for the various ionic species. Those parameters are the number density, n, the velocity vector $\vec{v}$, and the thermal speed, w, which is related to the temperature of the ions (see Section 1.6.3).

Once the ionic parameters have been compiled from the ionic spectra, various analyses of those parameters can be performed. The two most basic are the variation of these parameters with time and with distance. Both of these will be discussed more fully in a later section. The bulk of my work will be a compilation of parameters for the ions H^+ and He^{+2}, the two most abundant ions in the solar wind.

1.5. The Structure of This Thesis

In Chapter 2, I discuss periodic variations of the solar wind which persist into the outer heliosphere (beyond 15 AU). The most notable structure is a ~26-day periodicity caused by solar rotation. In addition there are variations due to the 11-year solar cycle, and there is evidence of a ~154-day periodicity. This periodicity is most clearly seen in the radial component of the H^+ velocity. There is also marginal evidence for a periodicity of ~146 days which has not been reported before.

In Chapter 3 I deal with the difference between the velocity vectors of the H^+ and

He^{+2} ions. This difference should be aligned with the interplanetary magnetic field $\vec{B}$, and I have verified that this is the case. I have compiled extensive statistics to show that the magnitude of the velocity difference is constrained by the local Alfvén speed.

Also in Chapter 3, I look at double streaming events. These events are two populations of H$^+$ ions (and often accompanied by double streaming He^{+2} ions) traveling at different velocities. I have noted when and how often these events occur as well as under what conditions. This particular analysis had not been previously pursued with Voyager data.

In Chapter 4, I discuss the the detection by Voyager of ions other than H$^+$ and He^{+2}. The most prevalent is O^{+6} . The spectra also show the presence of O^{+7}, N^{+6}, and C^{+5}. The abundances of O^{+6} and O^{+7} have been measured (for distances up to ~5 AU), and the ratio of the number density of O^{+7} to that of O^{+6} has been used to determine an average coronal temperature of 1.7 x 10^{6}K which is in agreement with coronal temperatures derived by others (e.g. Bochsler and Geiss, 1989). As a side study, I investigated how the abundance of He^{+2} changes with the H$^+$ density. Such changes can be used to identify possible flare events.

Finally, I close this chapter with a brief description of the solar wind parameters, and their large scale behavior with distance from the Sun.

1.6. General Properties of the Solar Wind

To get an idea of the overall behavior of the solar wind, I have plotted the various parameters: number density, n; the radial velocity, vr; the tangential velocity, vt;, the normal velocity, vn; the thermal speed, w, with respect to the spacecraft distance from the Sun, r. Plots of these parameters, computed from Voyager 2 observations, are shown in Figure 1.5. I will discuss these parameters separately.

1.6.1. The Number Density n

The top panel in Figure 1.5 is the proton number density, n, plotted against the space-craft distance, r. The units of density (from here on the word "density" by itself will be understood to mean number density) are particles per cubic centimeter (cm^{-3}), and r is in astronomical units (AU) where 1 AU is the mean Earth-Sun distance (1.49×10^8 km). Due to the large change in the magnitude of the density over the distance plotted here, the scale of the density is logarithmic. One can see that, aside from some fluctuations, the density monotonically decreases with increasing heliospheric distance. If one looks at a log-log plot of n plotted against r (Figure 1.6), one can see that the relation is a power law:

$$n(r) = \frac{n_o}{r^m} \tag{1.1}$$

where n_0 is the density at 1 AU, and r is in AU. If the solar wind is expanding with a uniform radial velocity, the m = 2 by conservation of total particle number.

The observed values of m and n_0 were determined by first averaging the data in bins that were 0.1 AU wide. Equation (1.1) was transformed into a linear equation by

14
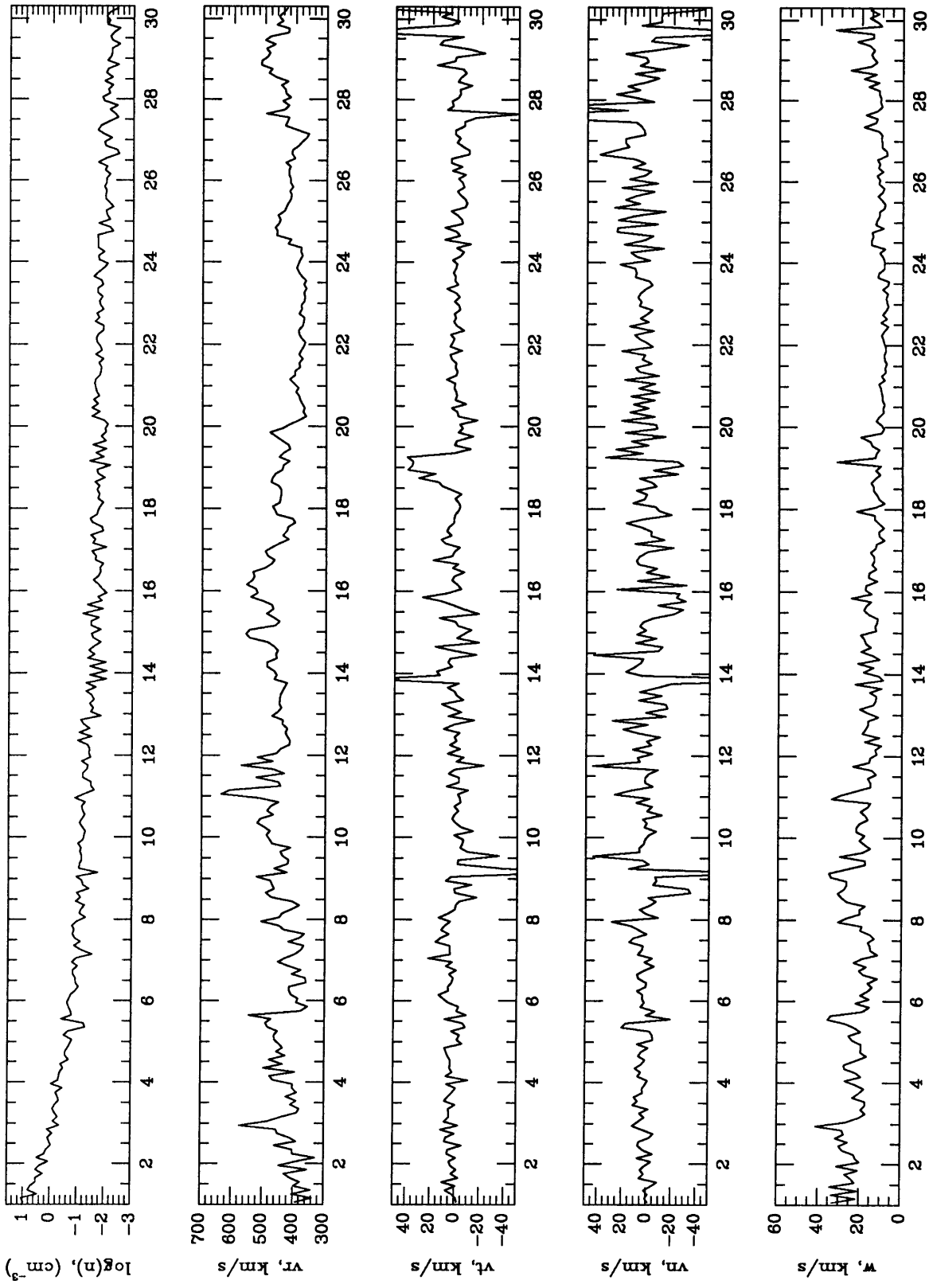
Figure 1.5. Solar wind parameters plotted against distance (AU).

15
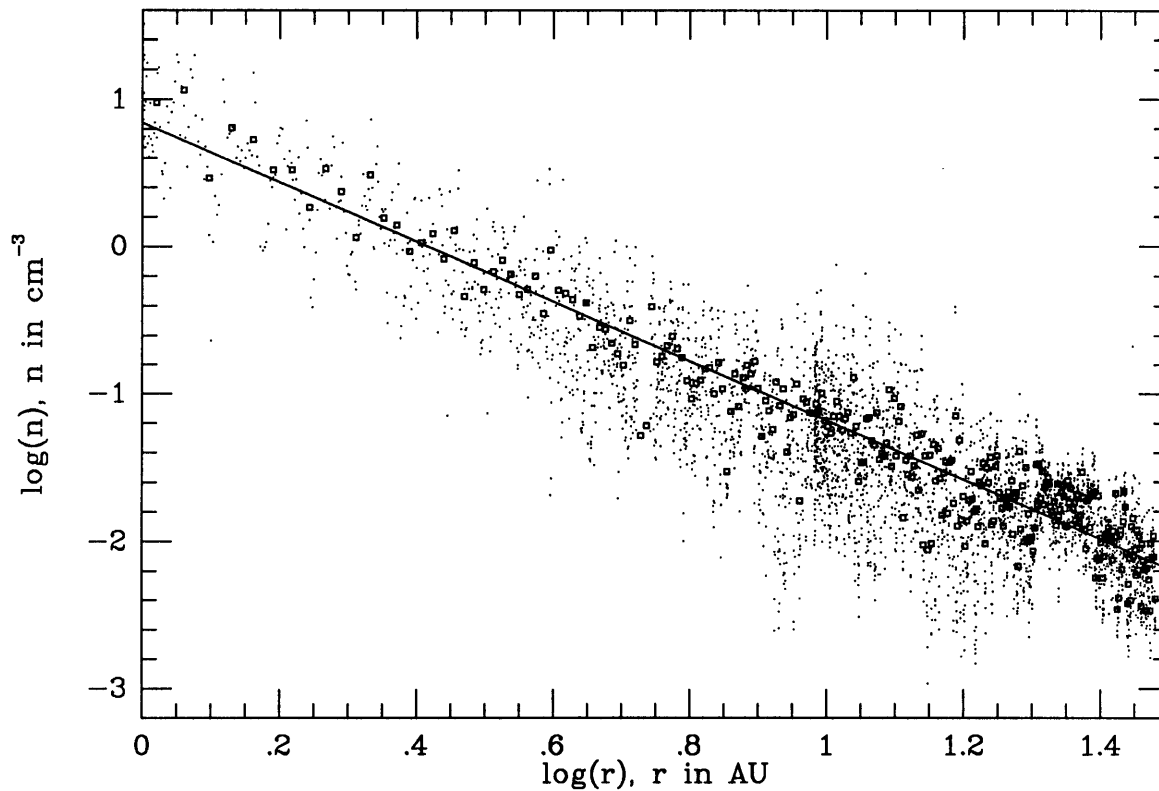
Figure 1.6 Power law relation of n with distance
Points are daily averages. Squares are radial averages.

taking the logarithm of both sides. A linear least squares fit was then performed on the transformed equation. The best fit values found were $n_0 = 6.92 \pm 0.64$, $m = -2.02 \pm 0.04$ (Voyager 2) and $n_0 = 7.31 \pm 1.20$, $m = -2.16 \pm 0.12$ (Voyager 1). The value deduced for m is in good agreement with that deduced from conservation of particle number.

1.6.2. The Velocity $\vec{v}$

Before discussing the velocity of the solar wind, I shall give a description of the coordinate system used in solar wind analysis. The system is called RTN because the three directions are the radial, tangential, and normal. To help establish these

16

directions imagine a point P located at some distance r from the Sun. Let the point be on a sphere of radius r centered on the Sun and extend the solar poles so that they intersect the sphere. The plane of the solar equator intersects this sphere and defines its equator.

Let the vector $\vec{r}$ be the vector that extends from the center of the Sun to the point P. The radial direction is then defined as a unit vector $\hat{r}$ that extends from P parallel to $\vec{r}$ and away from the Sun. The tangential direction, $\hat{t}$, is defined as a vector perpendicular to $\hat{r}$ and parallel to the solar equatorial plane with the positive direction in the direction of planetary motion (counterclockwise as viewed from above the solar north pole). The normal direction is defined as the vector $\hat{n}$ that forms a right-handed coordinate system with $\hat{r}$ and $\hat{t}$. If one introduces an auxiliary vector $\hat{z}$ one can formally define $\hat{t}$ and $\hat{n}$ as

$$\hat{t} = \frac{\hat{r} \times \hat{z}}{|\hat{r} \times \hat{z}|} \qquad \hat{n} = \frac{\hat{r} \times \hat{t}}{|\hat{r} \times \hat{t}|} \qquad (1.2)$$

These vectors are shown in Figure 1.7.

The second panel from the top in Figure 1.5 deals with the radial velocity, vr, which is the component of the solar wind velocity along the radial direction (vr should more properly called "radial speed", but "radial velocity" is the convention). The units of vr are km/s, and as one will note, it is the largest of the velocity components. The average solar wind speed is ~400 km/s and vary from ~300 km/s to over 800 km/s. There are large fluctuations in the radial velocity which start to decrease near 12 AU. These reduced fluctuations continue until about 20 AU when vr suddenly drops from an average value of ~450 km/s to around 400 km/s, then, near 24 AU, vr increases back to

17
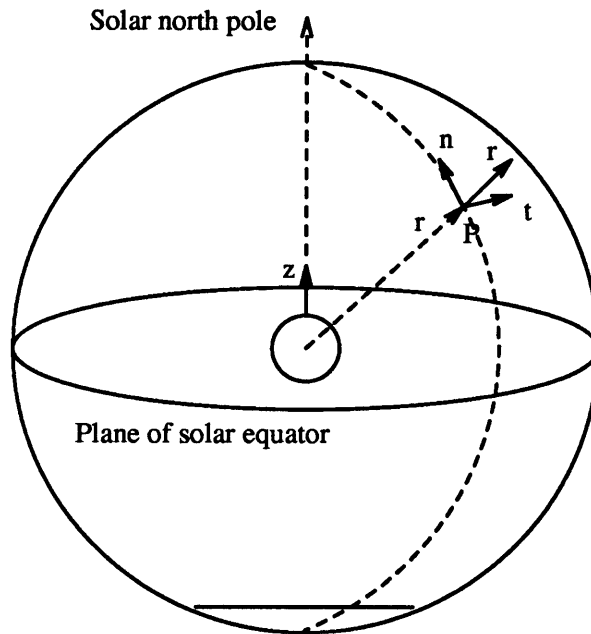
Figure 1.7. Diagram of the RTN coordinate system showing the relative orientation of the direction vectors.

about 450 km/s with a great reduction in fluctuations. The sudden decrease in vr at 20 AU is not due to distance, but rather to changes on the Sun from the solar cycle which is discussed in the next chapter.

The tangential velocity has an average value of 2 km/s with fluctuations as large as 50 km/s or more. These fluctuations sharply decrease and stay small for an interval that coincides with the "flat" region of vr discussed above. This behavior is no doubt due to the solar cycle as well.

The normal velocity also has an average value of 2.3 km/s with large fluctuations in value. From 20 AU to 25 AU, vn exhibits an obvious sinusoidal behavior which will

18

be investigated further in the next chapter.

1.6.3. The Thermal Speed w

The most probable thermal speed, w, is a measure of the random or thermal motion of the solar wind particles as seen in a frame moving with the bulk velocity of the plasma. The thermal speed is related to the ion (or kinetic) temperature, T, by

$$kT = \frac{1}{2}mw^2 \tag{1.3}$$

where k is Boltzmann's constant.

The thermal speed decreases with increasing distance from the Sun. However, this decrease is slower than the decrease for number density. This behavior of the thermal speed can be predicted if the solar wind is assumed to be like an ideal gas that is expanding adiabatically. The relation for the adiabatic expansion of an ideal gas is

$$PV^\gamma = P_oV_o^\gamma \tag{1.4}$$

where P is the internal pressure of the plasma, V is the volume, and γ is the ratio of the specific heats. One can consider the internal pressure as an energy density which is given by

$$\varepsilon = \frac{1}{2}nmw^2 \tag{1.5}$$

where n is the proton number density already discussed and m is the proton mass. The volume under consideration is a spherical shell of radius r, centered on the Sun, and of thickness $\Delta r \ll r$. If it is assumed that the solar wind is traveling at a constant radial velocity, then the thickness of the shell remains constant.

19
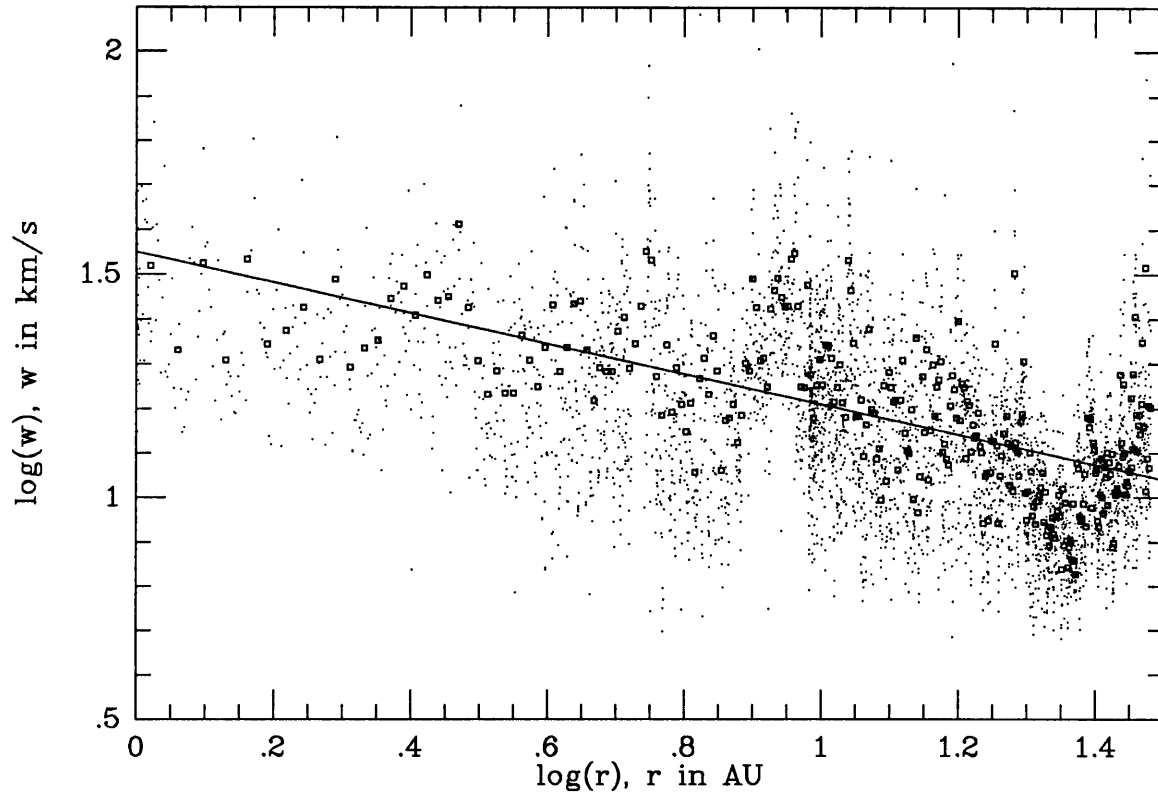
Figure 1.8 Power law relations of w with distance.
Points are daily averages. Squares are radial averages.

If Equation (1.5) is inserted into Equation (1.4) along with the volume of the shell and

the constant terms are eliminated, the resulting relation is

$$nw^2r^{2\gamma} = n_0w_0^2r_0^{2\gamma} \qquad (1.6)$$

The density can be eliminated be using its $1/R^2$ dependence. Once this is done the

remaining terms can be rearranged to yield

$$w = w_0\left[\frac{r_0}{r}\right]^p \qquad (1.7)$$

where $p = \gamma-1$. Thus the thermal speed follows a power law which can be seen from

Figure 1.8 (although the relation is not as obvious as it is for the density).

What can be predicted about the value of p? Since an expanding gas or plasma cools,

p must be greater than zero. Also, from the equipartition theorem, γ is $1+2/\nu$ (which implies $p=2/\nu$) where ν is the number of degrees of freedom which for an ideal gas is at least 3. So p should be less than or equal to 2/3.

I performed a linear regression of the thermal speed vs. distance from the Sun (using data binned by distance), and found that $p = 0.34\pm0.02$ (Voyager 2) and $p = 0.33\pm0.07$ (Voyager 1). This value of p indicates that the solar wind is cooling more slowly than an ideal gas, which has led researchers to consider phenomena such as stream-stream interactions that heat the solar wind by shock dissipation.

CHAPTER 2

Periodicities in the Solar Wind

2.1. Introduction

In Chapter 1, the variation of the mean solar wind parameters with respect to distance was examined. In this chapter the focus will be on temporal variations of these mean parameters. The variations sought were periodic behavior on the order of one to a few months, and the change of this behavior within an 11-year solar cycle.

Within the solar cycle I mainly searched for variations with a period of 25.4 days (the solar sidereal period [*The Astronomical Almanac*, 1994]). This period was first seen in the solar wind velocity through observations from Mariner 2 [*Neugebauer and Snyder*, 1966] and many other spacecraft since then. This period has also been clearly seen in other solar observations. For example, Donnelly and Puga have [1990] have found periodicities of 27 days in solar UV flux (1750-2900 Å) measurements, chromospheric EUV, X-ray (1-8 Å), and 10.3 cm (radio) flux. This periodicity is due to rotation of long-lived (i.e. lasting at least one rotation) features rotating with the solar rotation period.

Other solar observations have also revealed periodicities. For example, Bai et al. [1987, 1989] have found periodicities of 154 days in proton flare rates (and other

22

phenomena), and also periodicities of 129, 104, 78, and 51 days [*Bai et al.*, 1991]. Rieger et al. [1984] presented evidence for 154 day periodicity in hard solar flares, consistent with the period found by Lean and Bruckner [1989] of 155 and ~250 days in the sunspot blocking function (the diminution of solar luminosity due to the darker sunspots), Zurich sunspot number, 10.3 cm flux, and solar EUV emissions by Hoegy and Wolff [1989]. Gabriel et al. [1990]. have also found periodicities of 154 days and ~51 days in the solar proton rates during solar cycles 19, 20, and 21.

The solar cycle is well established by some 300 years of sunspot observations and auroral observations [see the review by *Silverman, 1990*] as well as cosmic ray monitoring [*Svalgaard and Wilcox*, 1974] and magnetic flux measurements.

The 11 years of Voyager data were too short to look for solar cycle variations in the solar wind, but the data sets are long enough to look for periods on the order of a month to a year. This chapter will be devoted to looking for periodicities in the solar wind with emphasis on variability due to solar rotation.

Since the periodicities sought were on the order of one to five months, the data derived from the individual spectra were combined into daily averages. These averages were corrected for spacecraft motion as detailed in the next section. Because there were missing data (see next section), these daily averages were subjected to a nonstandard spectral analysis which is discussed in Section 2.3. The results of this analysis are then given in Section 2.4.

2.2. Data Base

The data used were the solar wind parameters derived from ion spectra from Voyager 2 between day 234 of 1977 and day 249 of 1989. Not all the spectra were used. Those spectra in which the magnitude of the tangential velocity or the normal velocity exceeded 50 km/s were excluded from the analysis because the fitting routine was unstable for these spectra and parameters derived from them were deemed unreliable. In addition data are missing due to planetary encounters, gaps in spacecraft tracking, and spectra which cannot be fit.

Since the spacecraft is not at rest with respect to the Sun, any periodic solar signal will be distorted by the spacecraft's motion. Since the spacecraft is in the ecliptic plane (and roughly in the plane of the solar equator) during the time covered by this analysis, only motions in that plane need be considered. I consider separately the effects of radial motion (directly away from the Sun), and angular motion (around the Sun).

If there is a periodic (sinusoidal) variation in a solar wind parameter with frequency f, and if this parameter is plotted with respect to time, it will be seen to have a frequency f if the spacecraft is stationary with respect to the Sun. However, if the spacecraft is moving radially with constant speed v_{sc}, then the parameter will have an observed frequency of $(1-v_{sc}/V_{sw})f$, where V_{sw} is the solar wind speed, assumed to be radial and constant. This is nothing more than a Doppler shift of the frequency.

In order to recover the unshifted frequency, one simply multiplies the the time of the

observations t_n by the factor $(1 - v_{sc}/V_{sw})$. Now if one plots the parameter against $t_n(1 - v_{sc}/V_{sw})$, one will deduce that the variation has a frequency f.

Unfortunately, since neither the spacecraft speed nor the solar wind speed is constant, the procedure for "correcting" the time of the observations must be generalized. If one assumes the times of the spacecraft observations are uniformly spaced with spacing Δt, then $t_n = (n-1)\Delta t$ (assuming observations are started at t=0). If this form of the t_n is used then one can write (for n > 2)

$$t_n\left[1 - \frac{v_{sc}}{V_{sw}}\right] = t_n - \sum_{k=1}^{n-1} \frac{v_{sc}}{V_{sw}}\Delta t \tag{2.1}$$

The generalization of this equation is now

$$t_n - \sum_{k=1}^{n-1} \frac{v_{sc,k}}{V_{sw,k}}\Delta t_k \tag{2.2}$$

where $v_{sc,k}$ and $V_{sw,k}$ are, respectively, the spacecraft and solar wind radial speeds at time t_k and $\Delta t_k = t_k - t_{k-1}$ since the observations are not uniformly space in time.

In addition to its radial motion Voyager is also moving in longitude λ with an angular speed ω. Since some of the variations in the solar wind are due to the rotating Sun, the frequencies of the variations will also be Doppler shifted by a factor of $(1 - \omega/\Omega_\odot)$ where $\Omega_\odot$ is the sidereal angular speed of the Sun. The corrections of the observing times follows a form similar to that for radial motion:

$$\tau_n = t_n - \sum_{k=1}^{n-1} \frac{\omega_k}{\Omega_\odot}\Delta t_k \tag{2.3}$$

where ω_k is the angular speed of the spacecraft at time t_k.

The combination of Equations (2.2) and (2.3) yields the time correction that takes both

motions into account (for $n \geq 2$),

$$\tau_n = t_n - \sum_{k=1}^{n-1} \left[\frac{V_{sc,k}}{V_{sw,k}} + \frac{\omega_k}{\Omega_\odot} \right] \Delta t_k \qquad (2.4)$$

The corrections for spacecraft motion are performed on the individual ion spectra, which are then combined to form daily averages. The corrections result in a shifting of the spectra times. Each shift becomes larger as the distance from the Sun increases. The net effect is to compress the data by about 200 days. A plot of these "corrected" daily averages is shown in Figure 2.1.

2.3. Analysis

Four time intervals were chosen, each about 1000 days (~3 years) in length. The intervals were chosen to coincide with certain features of the data and roughly with various parts of solar cycles 21 and 22. Solar Cycle 21 runs from June 1974 to September 1986 with its maximum in December of 1979 [*Solar Geophysics Data*, 1981] (sunspot numbers) or August 1981 (total magnetic flux). For the purposes of this analysis, the maximum of Solar Cycle 21 is taken approximately as September 1980. This time corresponds to the onset of the anomalous warming in the normalized thermal speed and a change in the characters of the tangential and normal velocities. The end of Solar Cycle 21 is taken approximately as March 1986, a time at which the amplitudes of the normalized density and tangential velocity are suddenly reduced, the average radial velocity drops about 60 km/s, and the normal velocity starts to exhibit obvious sinusoidal behavior. The intervals chosen are: A=1977.64-1980.44,
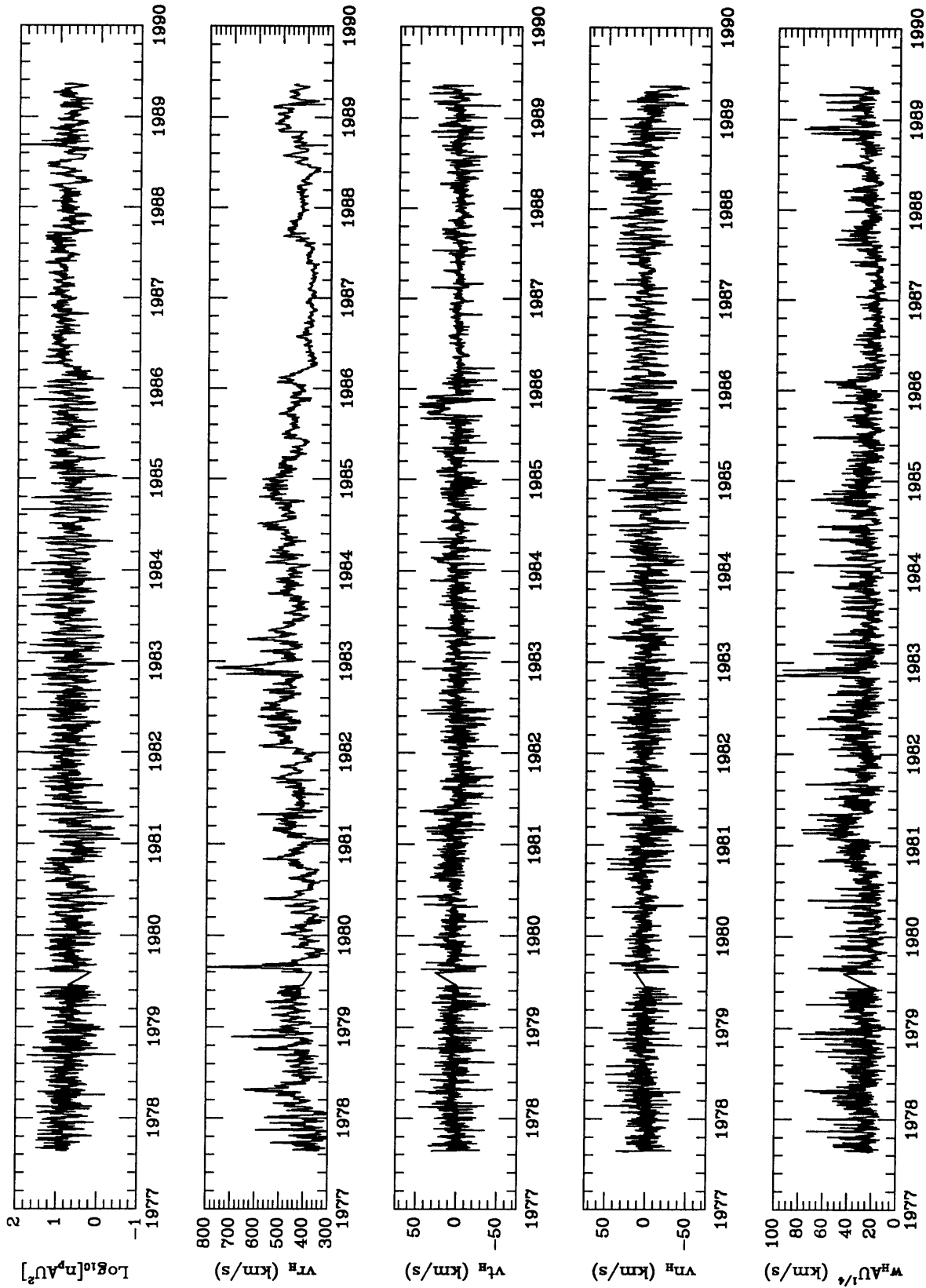
26

Figure 2.1. Solar wind parameters plotted against "corrected" year.

27

B=1980.44-1983.25, C=1983.25-1986.05, and D=1986.05-1988.85.

Due to planetary encounters, tracking gaps, and selection procedures, there were days for which there were no averages. Rather than replace the missing data with zeros or the mean and trying to get a power spectrum from the Discrete Fourier Transform (DFT), the corrected averages were treated as "an unevenly sampled time series" [Horne and Baliunas, 1986] and subjected to the Scargle "periodogram" [Scargle, 1982] (see Section 2.6 for a fuller explanation).

For each interval, the data were detrended using a fourth order polynomial in time. This procedure reduces the effects of slow variations in the data that are not sinusoidal (e.g. an average linear increase in the data). These variations would confound the results by contributing to the power at low frequencies. A periodogram was then constructed for each of the plasma parameters, normalized density, nR^2; radial velocity, vr; tangential velocity, vt; normal velocity, vn; and normalized thermal speed, $wR^{1/3}$. The particle density and thermal speed were normalized to remove the effects of distance shown in Section 1.5. The periodograms are shown in Figures 2.2 - 2.6. The horizontal lines across each periodogram are confidence intervals that indicate the probability, p, that a resulting period is due to chance. Table 2.1 lists the periods (in days) found in each interval with the letters a, b, or c indicating the significance of the period or periods. The most significant periods are labeled with a "c" which indicates $p < 0.001$; similarly "b" indicates $0.001 < p < 0.01$, and "a", $0.01 < p < 0.1$.

```
den

  a    9.85, 31.03




vr

  a    19.69, 23.27, 29.26, 78.77
  c    26.95, 128.00, 256.00




vt






vn

  b    8.56




w

  a    7.16, 10.04, 22.76, 128.00
  b    12.49
  c    26.95
```

Interval A (1977.64 — 1980.44)

```
den

  a    13.48, 17.96, 23.81, 29.26
  a   128.00
  c    17.36, 22.76



vr

  b    85.33
  c    64.00, 146.29, 256.00




vt

  a    22.26




vn

  a    10.77, 18.26, 23.81, 26.26
  b    20.08, 22.76




w

  a    35.31
  c    64.00, 146.29, 204.80
```

Interval B (1980.44 — 1983.25)

```
den

  b   27.68
  c   24.38, 26.26




vr

  a   64.00
  c  146.29, 204.80




vt

  a   85.33
  c   33.03, 204.80




vn

  a   21.33, 22.76, 34.13
  c   24.38, 26.26, 31.03




w

  a   33.03, 113.77
  b   30.12
  c   14.63, 26.26
```

Interval C (1983.25 — 1986.05)

```
den




vr

  c  146.29, 204.80




vt

  a   25.60, 33.03
  b   16.79




vn

  a   37.93
  b   40.96
  c   22.76, 24.98, 26.95, 31.12
  c   33.03
w

  a  102.40
  c  146.29, 204.80
```

Interval D (1986.05 — 1988.85)

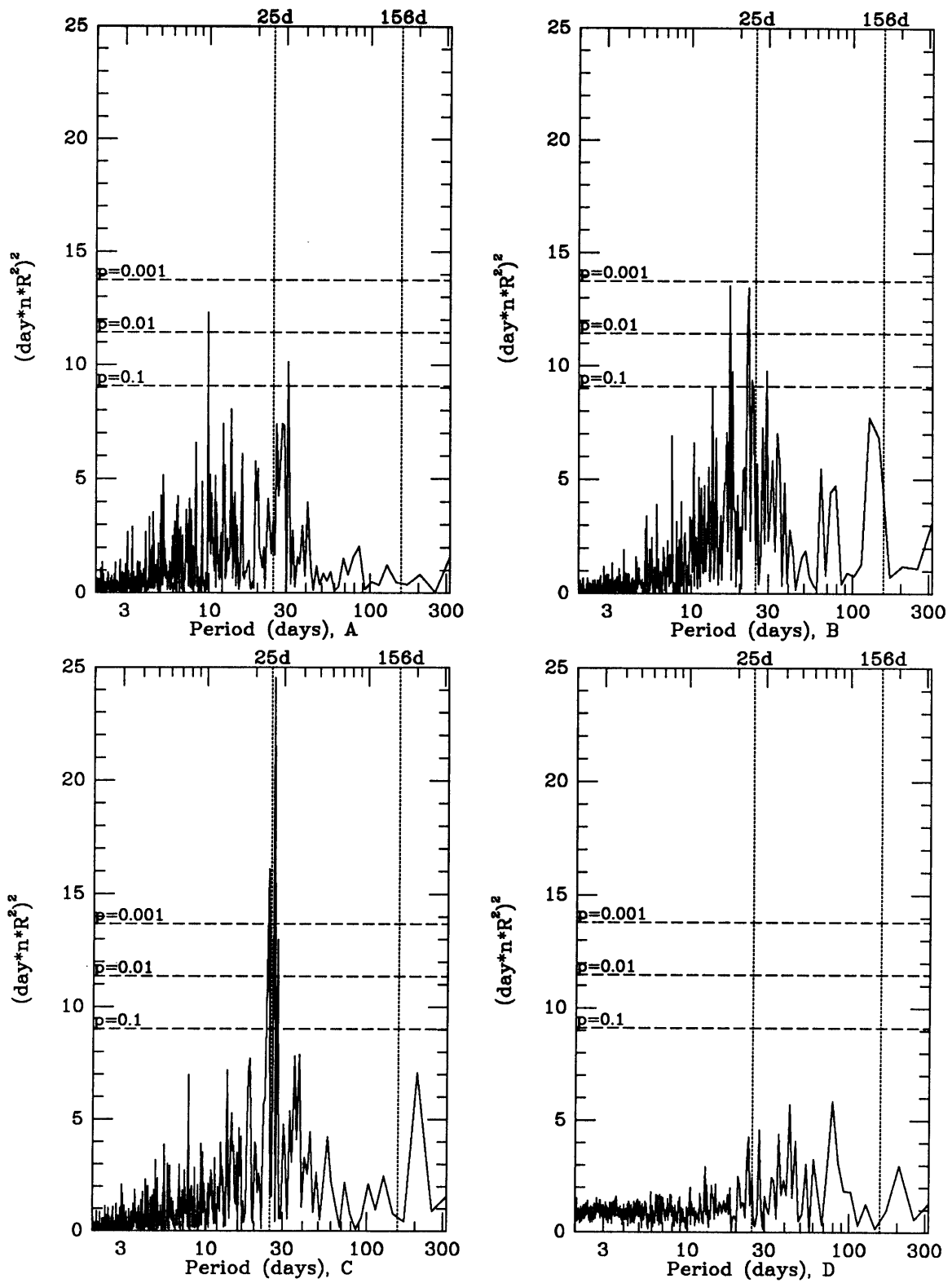Table 2.1   Significant periods (days) for Intervals A,B,C,D.

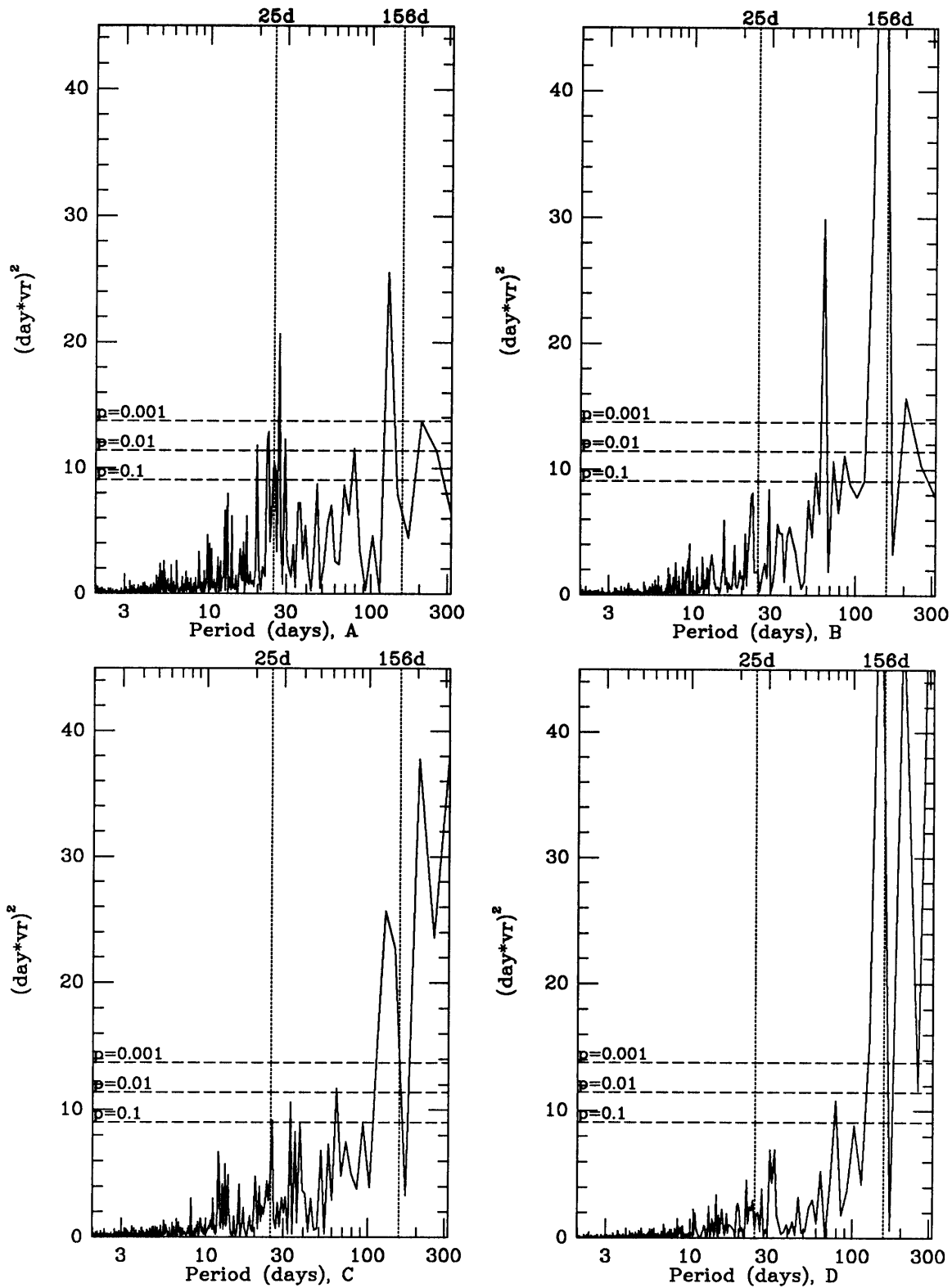Figure 2.2. Density periodograms. Intervals A,B,C,D.

Figure 2.3. Radial velocity periodograms. Intervals A,B,C,D.
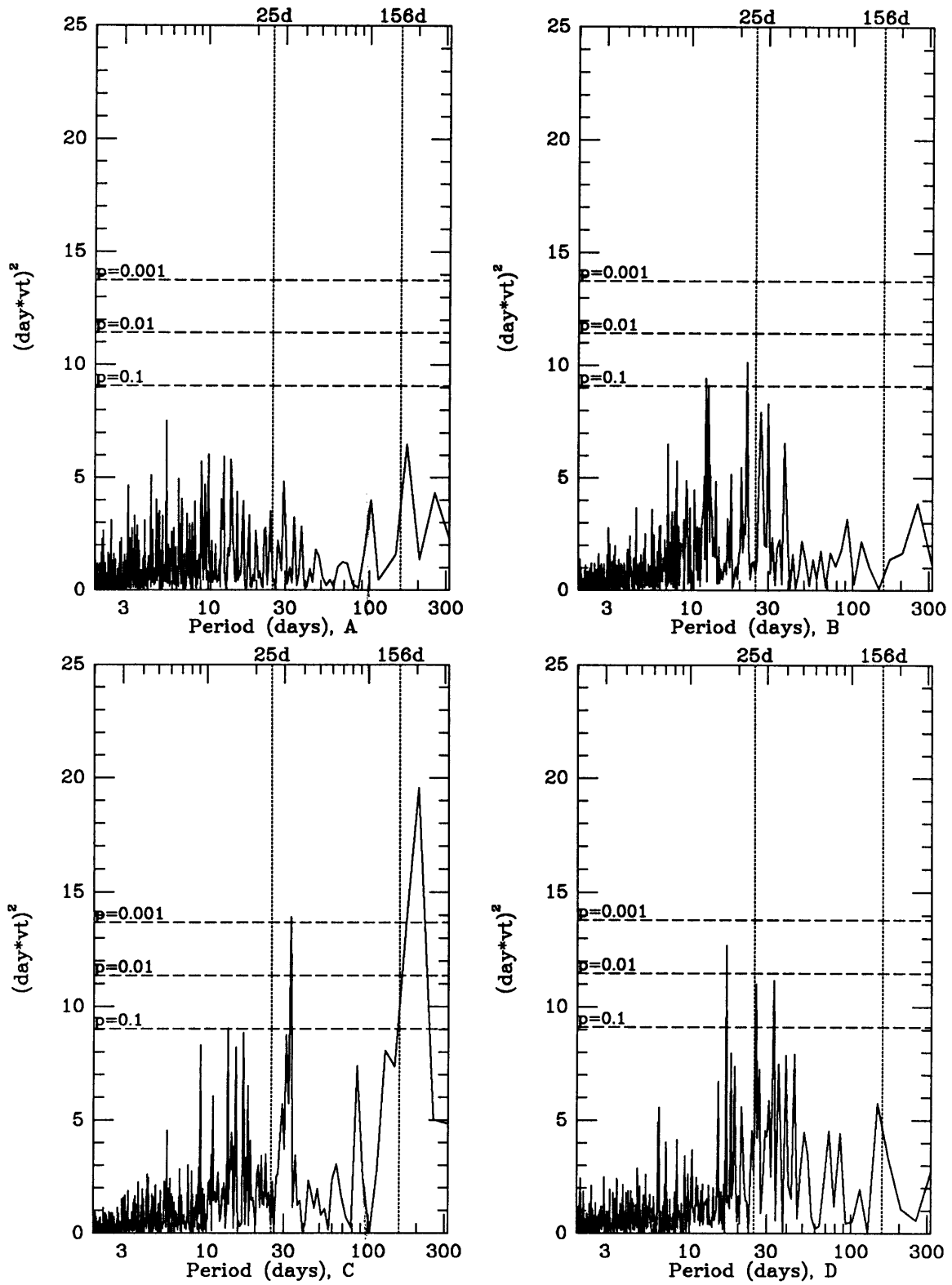
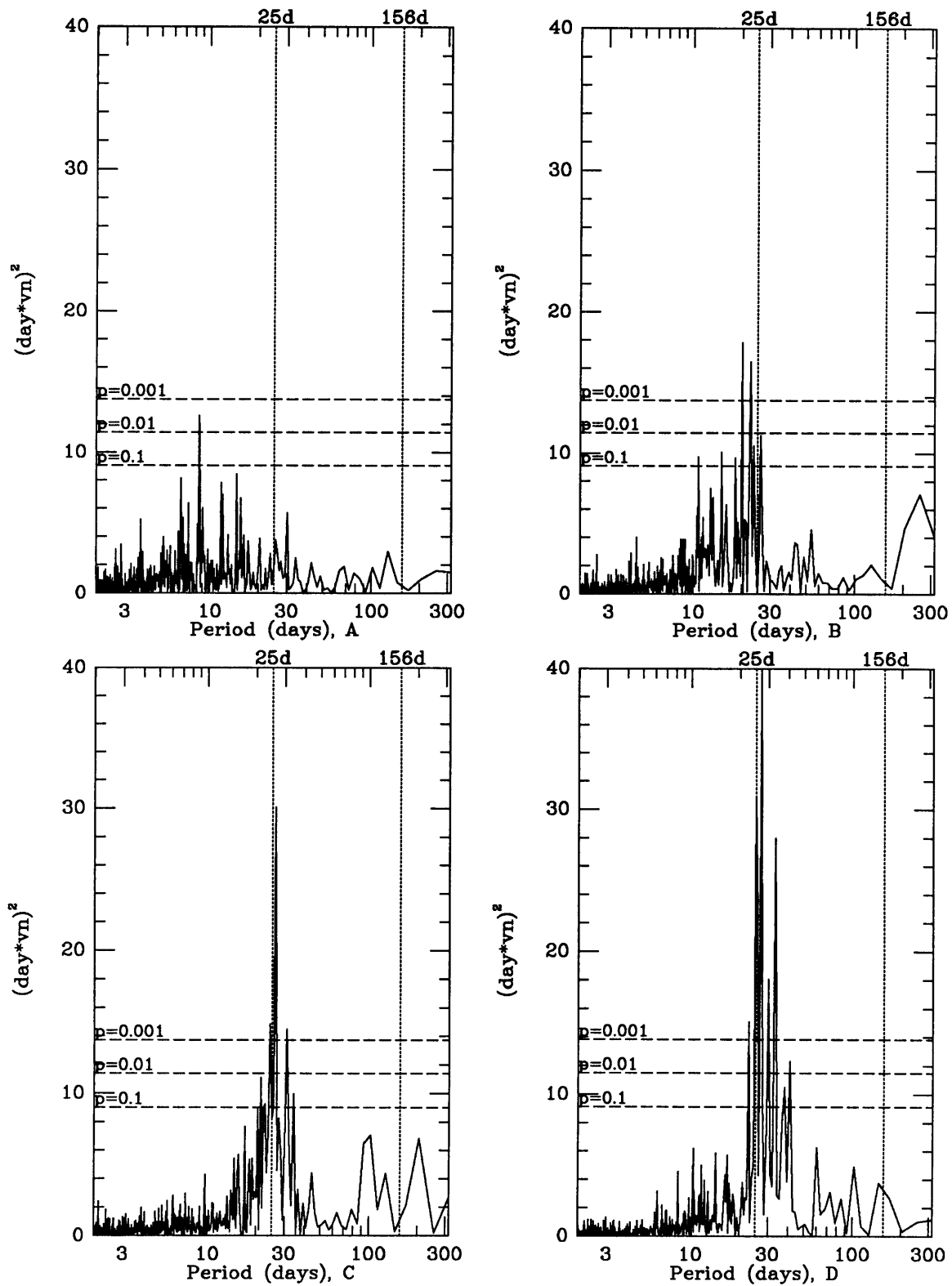Figure 2.4. Tangential velocity periodograms. Intervals A,B,C,D.

Figure 2.5. Normal velocity periodograms. Intervals A,B,C,D.
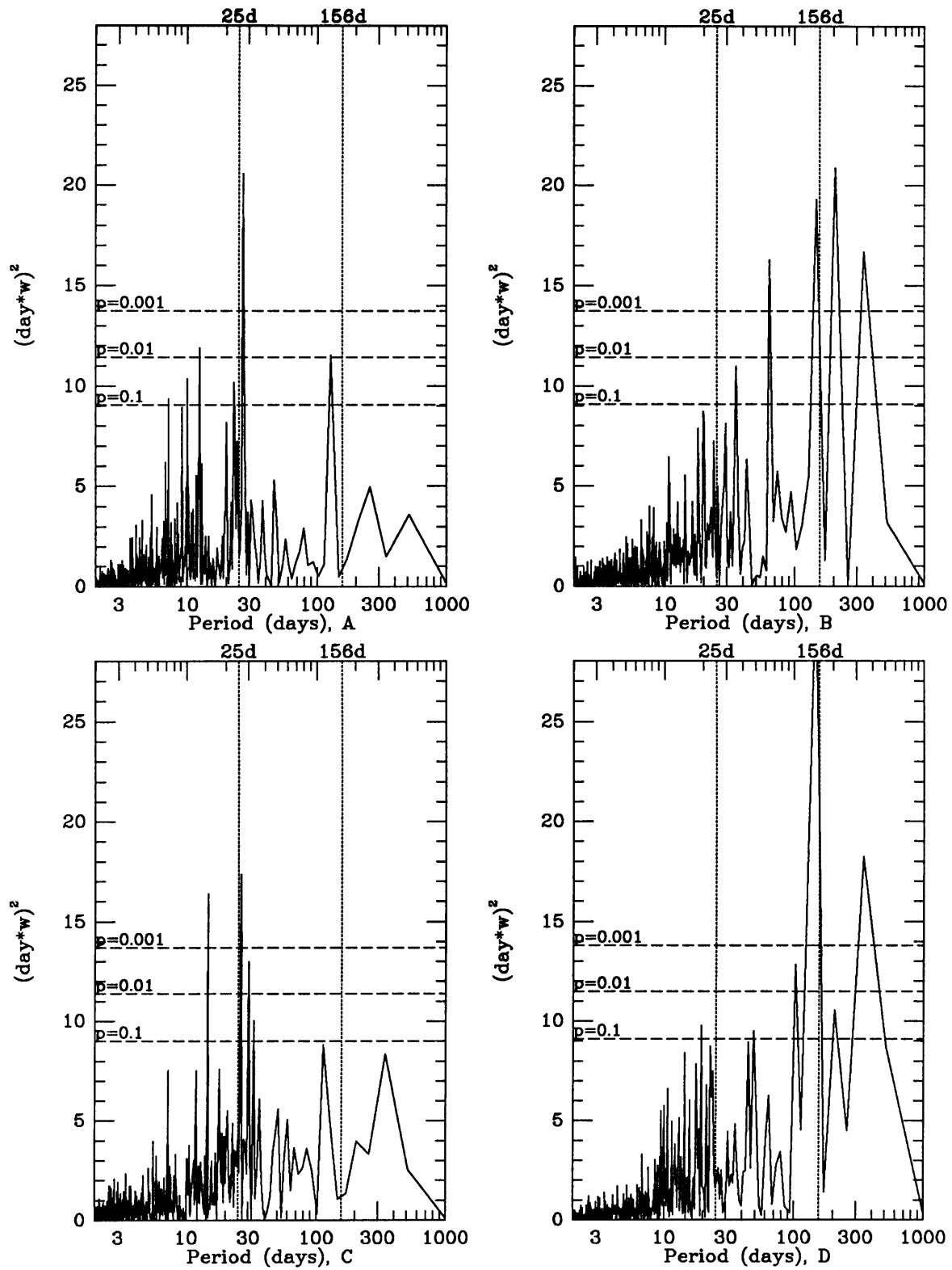
Figure 2.6. Thermal speed periodograms. Intervals A,B,C,D.

2.4. Expectations [4]

Since one is looking for the effects of solar modulation on the solar wind, one should first get a sense of the effects of the solar cycle on the corona of the Sun and possible effects on the solar wind. One can crudely divide the solar wind into a fairly constant low speed ($\leq \sim 450$km/s) part and a high speed part coming from long-lived structures on the Sun such as coronal holes, and transient structures such as coronal mass ejections (CMEs).

The Sun is surrounded by a magnetic field which directs the motion of plasma ejected near the photosphere. The charged particles flow along the field lines which can either be "open" or "closed". If the field lines are closed, they emerge from one region of the solar surface and enter at another. The structure of these closed field lines is dramatically illustrated in loop prominences. Open field lines create a "hole" through which the coronal plasma will leave the Sun and head out into space. These coronal holes are a major source of low-density, high-speed solar wind.

The structure of coronal holes varies with the solar cycle. During solar minimum when sunspot numbers are low and the total magnetic flux is small, coronal holes form at the poles and can extend toward or even beyond the solar equator. These holes can persist for many solar rotations, and as impose a large-scale, long-lived structure on the solar wind that co-rotates with the Sun. Therefore one would expect to see modulation of the solar wind by solar rotation most clearly during times of solar minimum.

---

4 The first four paragraphs of this section are based on *The Sun in Time*, Sonett et al. editors, The University of Arizona Press, 1991.

During solar maximum, the major source of high-speed solar wind observed near the ecliptic is not coronal holes, which shrink back toward the poles, but rather coronal mass ejections (CMEs). Material is ejected at random times from regions of the solar surface. The preponderance of CMEs destroys the time-independent structure of the solar wind, so detection of the solar rotation period would seem unlikely.

Therefore if coronal holes are the main source of high-speed, low-density solar wind during solar minimum, then one might expect to see rotational modulation in the normalized density and radial velocity in Interval A, since in this interval the Solar Cycle 21 is rising to its maximum (i.e. the co-rotational features on the solar surface have not completely disappeared). Since Interval B contains the time just after solar maximum, one would expect not to see solar modulation of the solar wind due to the presence of sporadic CMEs (assuming no equatorial extension of coronal holes). One might also expect not to see rotational modulation during Interval C since the declining phase of a solar cycle is known to be the most active phase in terms of CMEs and flares [*Hundhausen*, 1993]. Interval D contains the rising phase of Solar Cycle 22 and one would expect to see rotational modulation at this time. This expectation may be lessened by the fact that Voyager 2 is beyond the distance of the planet Uranus (~20 AU) during this last interval, and stream interactions may have erased the effects of rotational modulation [*Gazis*, 1989]. However, recent work by Richardson et al. [1994] show that between 1987 and the beginning of 1994 (when Voyager 2 moved from 20 to 44 AU from the Sun), there exists a 1.3 year periodicity exists in the radial velocity. The cause of this periodicity is unknown at this time.

2.5. Results

From Table 2.1, one sees that, contrary to expectations, there is evidence for modulation by solar rotation in all four intervals instead of only the first and last ones. In the Interval A one sees, as expected, values near the solar sidereal rotation period in the radial velocity. One also sees them in the normalized thermal speed, which is not surprising since higher thermal speeds are correlated with higher solar wind speeds [Ogilvie et al., 1980]. Curiously, for the normalized density there are no significant periods at the solar rotation period of 25.4 days.

In the Interval B there seems to be rotational modulation in the normalized density despite the fact that the maximum of Solar Cycle 21 is contained in this interval. There is also some evidence of modulation in the normal velocity although it is not the most significant. Note that as expected there is no evidence of rotation modulation in vr or in $wR^{1/3}$.

For Interval C the rotational modulation in nR^2 and vn is still present. Rather puzzling is that the solar rotational period is the most significant period present in the $wR^{1/3}$. The lack of a corresponding period in vr is troublesome especially since there is some additional variation going on at this time.

Finally in the Interval D, the solar rotation period is very evident in the normal velocity. The solar rotation period is also present in the tangential velocity. The other three parameters show no evidence of rotational modulation even though this interval contains the minimum of Solar Cycle 22 and modulation should occur for at least the

normalized density and the radial velocity.

Four other intervals (denoted E=1978.45-1979.56, F=1979.00-1981.74, F=1980.44-1986.05, and G=1986.26-1987.63) were chosen for investigation. The periodograms for the plasma parameters are shown in Figures 2.7 - 2.11. The significant periods are listed in Table 2.2. Interval E was chosen for the sinusoidal behavior exhibited by the radial velocity. The normalized thermal speed is lacking the 28.64 period present in the radial velocity. There are no significant periods near the solar rotation period in the other parameters. The interval F was chosen because it encompasses solar maximum when modulation by the Sun's rotation is not expected. However, as has been mentioned already, there appears to be significant modulation in the radial velocity, normalized thermal speed, and normalized density.

Interval G ranges from the the maximum of Solar Cycle 21 to the minimum of Solar Cycle 22 and shows rotational modulation in all parameters but the radial velocity. More will be said about this in the next paragraph. The last Interval H was chosen so that periodic behavior could be investigated in what appears to be a relatively "flat" stretch of the radial velocity. The most significant period is 167.00 days which may or may not be real (167 is about one-third of 500, the length of the interval in days). The most significant reliable period is one of 62.63 days and is also seen in the normalized density and the normalized thermal speed. While evidence for rotational modulation is seen in the normalized density, and the normal velocity, one should note that 62.63 is very close to 2.5 times 25.4, so the effects of rotational modulation may still be present for the radial velocity and normalized thermal speed.

```
den


vr

a  36.45, 44.56
c  23.59, 28.64


vt




vn

a   6.68
b   8.72


w

a  10.28, 12.15
c  23.59
```

Interval E (1978.45 − 1979.56)

```
den
a  11.77
b  17.88, 24.41
c  27.05


vr

a  66.73
c  27.05, 111.22, 143.00


vt

a  10.54


vn

a   8.86, 22.24


w

a  11.78, 24.41, 31.28
c  27.05, 143.00
```

Interval F (1979.00 − 1981.74)

```
den
a  16.52, 17.50, 18.62, 27.31
b  13.47, 23.54, 26.26
c  22.76, 24.38, 34.71

vr

a  51.20, 73.14, 93.09
b  56.89
c  64.00, 113.78, 146.27, 186.18
c  128.00
vt

c  29.68, 204.80



vn

a  10.72, 14.95, 20.28, 22.26
a  31.03, 186.18
b  18.29, 24.09
c  21.56, 23.01, 26.26
w

a  17.81, 19.69, 34.71
b  25.92, 64.00, 146.29, 186.18
```

Interval G (1980.44 − 1986.05)

```
den
a  15.66, 22.77
b  22.77, 62.63
c  27.83, 45.55


vr

a  16.70, 19.27
c  62.63, 167.00


vt

1  31.31



vn

a  41.75
b  22.77
c  25.05, 29.47 33.40


w

a  16.70, 22.77, 62.63
```

Interval H (1986.26 − 1987.63)

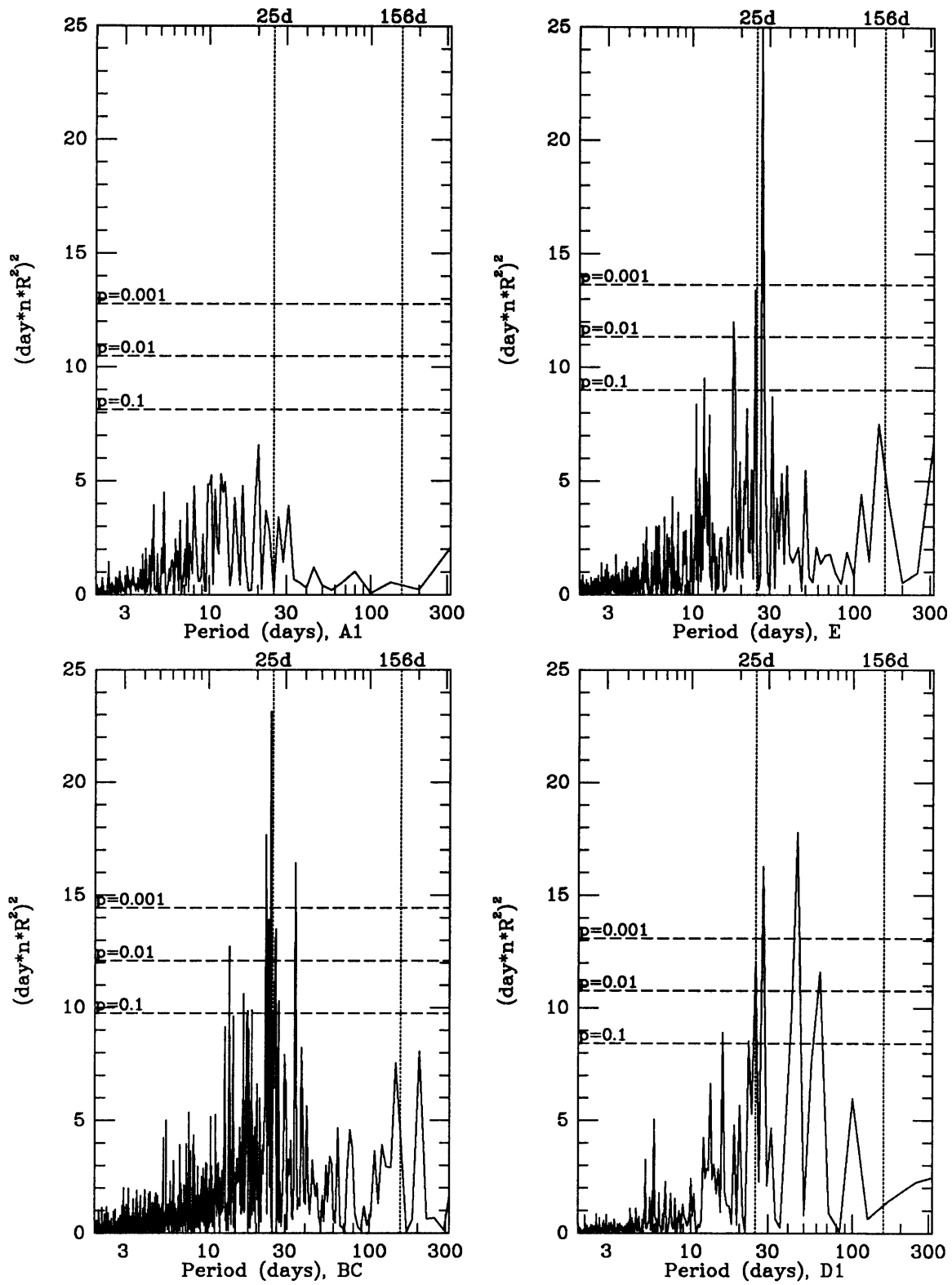Table 2.2   Significant periods (days) for Intervals E,F,G,H.

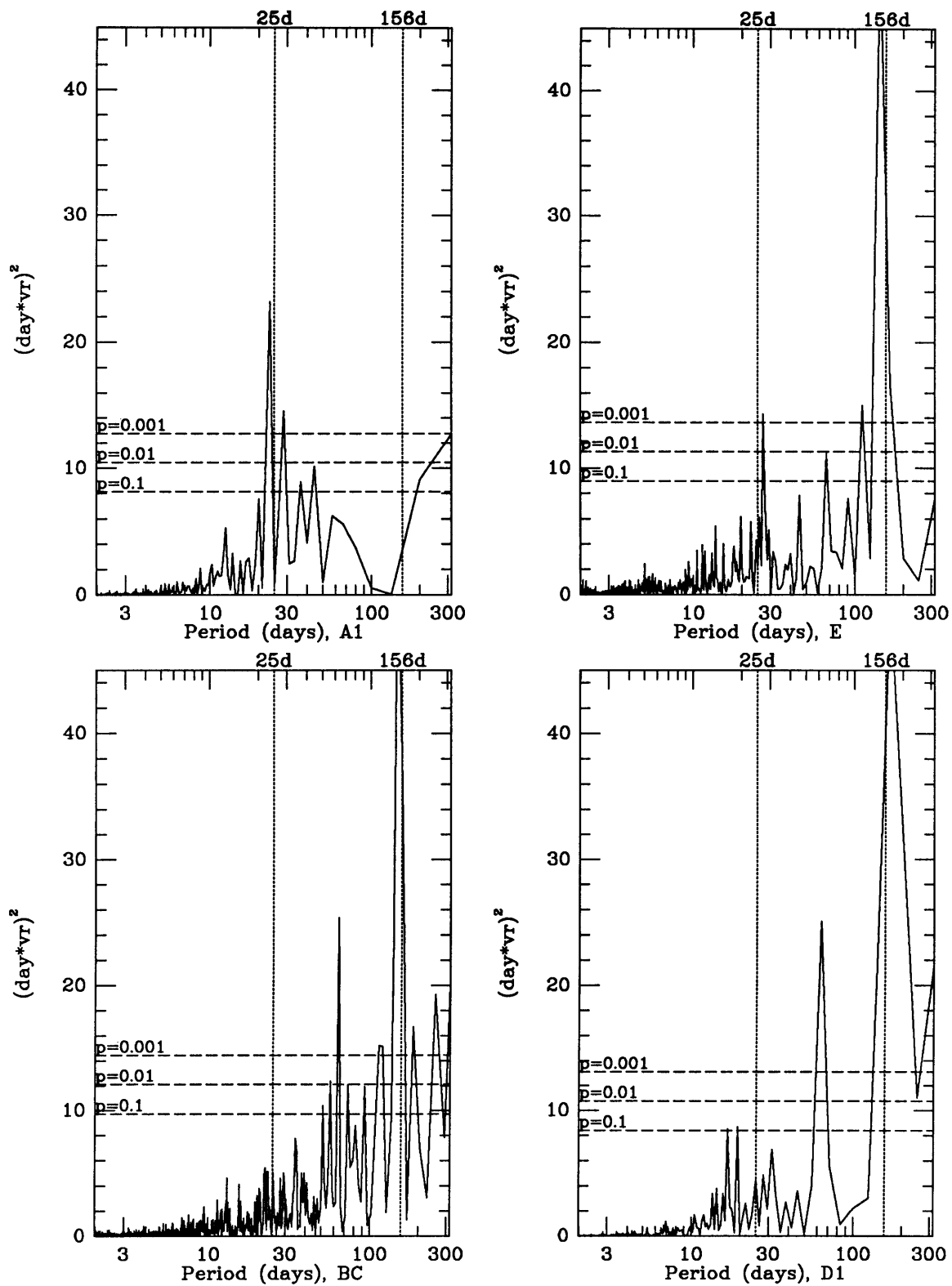Figure 2.7. Density periodograms. Intervals E,F,G,H.

40

Figure 2.8. Radial velocity periodograms. Intervals E,F,G,H.
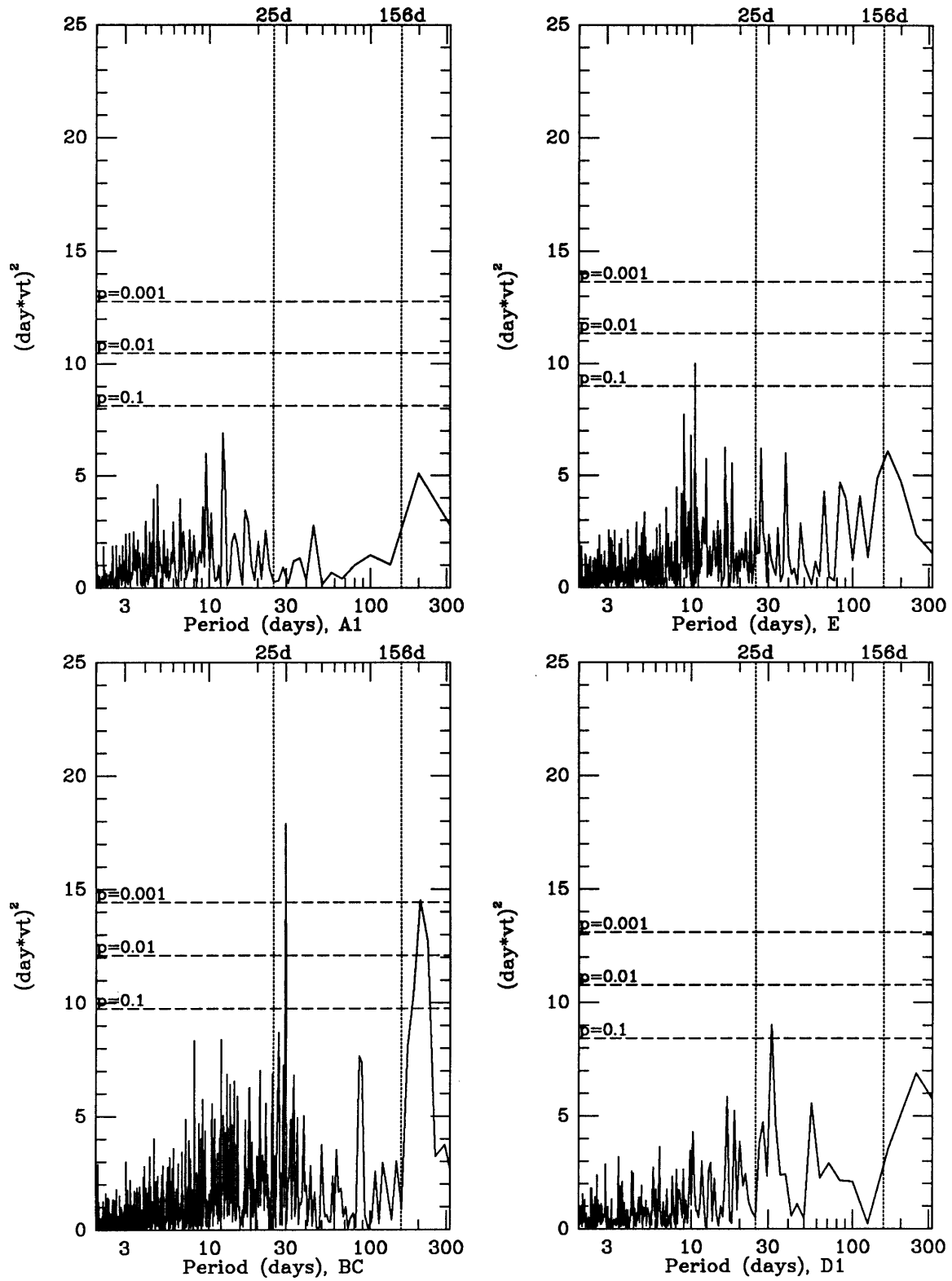
41

Figure 2.9. Tangential velocity periodograms. Intervals E,F,G,H.

PAGES (S) MISSING FROM ORIGINAL
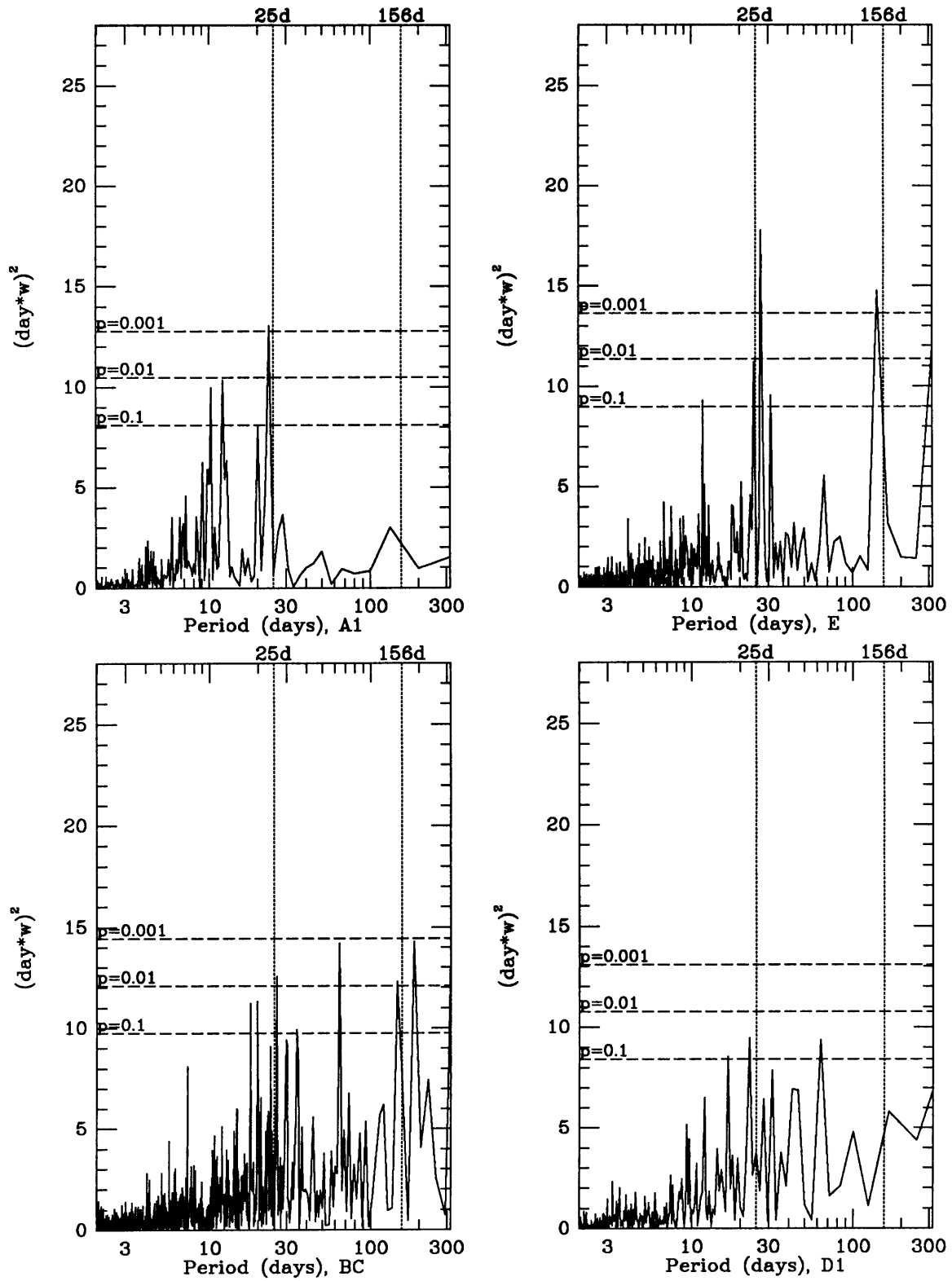
Figure 2.11. Thermal speed periodograms. Intervals E,F,G,H.

The periods from observations in solar flare rates and radiation flux (see chapter introduction) were sought. The 27-day (synodic) periodicity was obviously found so it is ignored here. The closest to the 13-day (also synodic) periodicity is the 13.47 period found in the normalized density in Intervals B and G. A period of 51.2 days was found in the radial velocity only in Interval G. The periods 78 days and 104 days were not seen in any of the time intervals investigated. A period of 128 days was seen in the normalized density during Interval B and in the radial velocity during Interval G. Finally the 154-day period was not seen, but a period of 146.3 days was seen in the radial velocity during Intervals B, C, D, and G. The same is true of the normalized thermal speed except for Interval C

2.6. Conclusion

Rotational modulation of the solar wind appears to be present throughout the 11 years of Voyager 2 data. During solar minimum, rotational modulation of the solar wind was expected to be caused by coronal holes extending from the solar poles to the solar equator. Since coronal holes are the source of high-speed low-density solar wind, one should see large scale structure in the solar wind with the solar rotation period. During solar maximum, the coronal holes retreat to a small regions around the poles, and sporadic CMEs and flares become the dominant source of high-speed solar wind with the polar coronal holes providing a continuous low-speed wind. During this time there should be little periodic structure in the solar wind, at least none with the solar rotation period.

This expected behavior turns out not to be entirely the case. While one does not see solar rotational modulation in the normalized density during Interval A one does see the modulation in the radial velocity (and in the normalized thermal speed) as expected. It seems that the modulation is no longer present during Interval D even though it overlaps the minimum of Solar Cycle 22. However the modulation is present for at least part of this time (interval D1) in the normalized density. As mentioned in the results section solar rotation may be responsible for the 62.63 day periodicity found in the radial velocity and normalized thermal speed. The presence of this period as well as the 1.3-year periodicity found by Richardson et al. [1994] can be used as an argument against the "washing out" of periodic structure in the radial velocity as noted by Gazis [1989].

Nor does this modulation disappear for the intervals B, C, and E which encompass solar maximum. There is still a periodicity present in the normalized density during these times. While this periodicity has seemed to have disappeared for the radial velocity, it is present for the normalized thermal speed for two of the three intervals discussed. The thermal speed is, however, affected by shocks. When one stream of plasma overtakes another, collisions among the ions cause the plasma to heat up at the expense of the velocity difference between the plasma streams. The velocity difference may be small, but it can cause a large increase in the thermal motion of the ions. Thus, shocks can result in large increases in the thermal speed and small changes in velocity.

The tangential velocity shows no significant periods at the solar rotation period (except

46

in the interval 3075-4098), but there are periods ranging from 22 to 33 days. Lastly the normal velocity shows evidence of rotational modulation during all times investigated except the first ~3 years, and there is obvious periodic structure in the in the last part of the data.

Although it seems fairly clear that what is being seen are effects due to time not distance, investigations of the solar wind data from Voyager spacecrafts are hampered by the inability to separate fully the effects of heliocentric distance and time. A way to remove the effect of distance would be to use solar wind data from an Earth-orbiting satellite such as IMP 8. A comparison of the data sets would be most interesting.

2.7. Scargle Periodogram

I discuss aspects of power series analysis using the Scargle periodogram. All of the material in Sections 2.7.1-2.7.3 is taken from the appendices in Scargle [1982], but I have included a modified version here for the convenience of the reader. In Section 2.7.1, the Scargle periodogram is introduced as a generalization of the familiar power spectrum that preserves the exponential behavior of the spectrum in the case of unevenly spaced data. Section 2.7.2 contains a discussion showing the equivalence of the Scargle periodogram and harmonic least-squares analysis (trying to fit the data with sines and cosines), and introducing the Lomb [1975] parameter τ. Finally the definition of τ and its invariance to time shifts is shown in Section 2.7.3.

2.7.1. Relation of Scargle Periodogram to Classical Periodogram

For a set of measurements, x_k, taken at times t_k (k=1, 2,..., N) , The discrete Fourier Transform (DFT) is defined as

$$F(\omega) = \sum_{k=1}^{N} x_k e^{-i\omega t_k} \qquad (2.5)$$

A common assumption is that the interval between successive measurement times is constant (i.e. equally spaced). While the DFT can be evaluated at any frequency, it is usually evaluated only at a set of evenly spaced frequencies, $\omega = 2\pi L/T$ where L is an integer between -N/2 and N/2 and $T = t_n - t_1$. These frequencies are used because the DFT evaluated at these frequencies contains all the information to reconstruct the original data and the DFT can be computed very quickly (if N is a power of 2) using the fast Fourier transform.

48

The power spectrum is defined as

$$P(\omega) = \frac{1}{N\sigma^2}|F(\omega)|^2$$ (2.6)

$$= \frac{1}{N\sigma^2}\left[\left[\sum_{k=1}^{N}x_k\cos(\omega t_k)\right]^2 + \left[\sum_{k=1}^{N}x_k\sin(\omega t_k)\right]^2\right]$$

where N is the number of data points and σ^2 is the variance of the data.

If the data contain a sinusoidal component with frequency ω_0, then then the factors x_k and $e^{-i\omega t_k}$ will be in phase and will make a large contribution to the periodogram for $\omega \approx \omega_0$. At other frequencies the terms will be randomly positive and negative and will add up to a small value of the periodogram due to cancellation. It is important to remember that the data may contain sinusoidal components at more than one frequency.

In addition to detecting sinusoidal components in the data one must be able to have some idea whether or not a large signal in the periodogram is meaningful or statistically significant. As it happens, if the data have a Gaussian distribution, then $z = P(\omega)$ has an exponential distribution [*Kendall*, 1955]. That is

$$P(z>z_0) = e^{-z_0}$$ (2.7)

This simple distribution makes it easy to assign confidence levels to the power spectra.

If the data are not equally spaced in time, the power spectrum loses this important property [Scargle, 1982]. To preserve the exponential distribution of the power spectrum, Scargle [1982] introduced a generalization of the DFT

$$P_x(\omega) = \frac{1}{2\sigma^2} \left[\frac{\left[\sum_{k=1}^{N} x_k \cos[\omega(t_k - \tau)] \right]^2}{\sum_{k=1}^{N} \cos^2[\omega(t_k - \tau)]} + \frac{\left[\sum_{k=1}^{N} x_k \sin[\omega(t_k - \tau)] \right]^2}{\sum_{k=1}^{N} \sin^2[\omega(t_k - \tau)]} \right] \quad (2.8)$$

This new form of the power spectrum which is called the (Scargle) periodogram has three important features. The first of these is that it preserves the exponential behavior of the power spectrum. Second, the parameter τ introduced by Lomb [1975] renders $P_x(\omega)$ invariant to changes in the time origin. Third, if the data are equally spaced in time, then $\tau = 0$, $\sum_{k=1}^{N} \cos^2(\omega t_k) = \sum_{k=1}^{N} \sin^2(\omega t_k) = N/2$, and the periodogram reduces to the power spectrum in Equation (2.5).

2.7.2. Equivalence of Periodogram and Harmonic Least-Squares Analysis

Instead of using the periodogram as defined in Equation (2.5), one can look for sinusoidal components in the data by fitting sine curves of various frequencies. In other words, let the best estimate of x_k at t_k be

$$\hat{x}_k = A\cos(\omega t_k) + B\sin(\omega t_k) \quad (2.9)$$

Fitting in the least-squares sense requires the minimization of the squared difference between x_k and $\hat{x}_k$. If $SSE(\omega)$ represents the sum of squares error (difference) between x_k and $\hat{x}_k$, then the expression to minimize is

$$SSE(\omega) = \sum_{k=1}^{N} [x_k - A\cos(\omega t_k) - B\sin(\omega t_k)]^2 \quad (2.10)$$

Setting the partial derivatives of $SSE(\omega)$ with respect to A and B to zero and rearranging terms yields the following set of equations:

$$\sum_{k=1}^{N} x_k \cos(\omega t_k) = A \sum_{k=1}^{N} \cos^2(\omega t_k) + B \sum_{k=1}^{N} \sin(\omega t_k)\cos(\omega t_k) \tag{2.11}$$

$$\sum_{k=1}^{N} x_k \sin(\omega t_k) = A \sum_{k=1}^{N} \sin(\omega t_k)\cos(\omega t_k) + B \sum_{k=1}^{N} \sin^2(\omega t_k)$$

The solutions to the equations in (2.11) would be simpler if the summations involving the cross-products of sines and cosines were to vanish. To this end Lomb [1975] introduced his parameter τ such that

$$\sum_{k=1}^{N} \cos[\omega(t_k - \tau)]\sin[\omega(t_k - \tau)] = 0 \tag{2.12}$$

Then the solutions for A and B are simply

$$A = \frac{\displaystyle\sum_{k=1}^{N} x_k \cos[\omega(t_k - \tau)]}{\displaystyle\sum_{k=1}^{N} \cos^2[\omega(t_k - \tau)]} \qquad B = \frac{\displaystyle\sum_{k=1}^{N} x_k \sin[\omega(t_k - \tau)]}{\displaystyle\sum_{k=1}^{N} \sin^2[\omega(t_k - \tau)]} \tag{2.13}$$

Now if these values of A and B are inserted into Equation (2.13), they will give the minimum value of SSE(ω) which is denoted by SSE(ω)$_{min}$. Expanding SSE(ω)$_{min}$ and making use of Equation (2.12) gives

$$SSE(\omega)_{min} = \sum_{k=1}^{N} x_k^2 - \frac{\left[\displaystyle\sum_{k=1}^{N} x_k \cos[\omega(t_k - \tau)]\right]^2}{\displaystyle\sum_{k=1}^{N} \cos^2[\omega(t_k - \tau)]} - \frac{\left[\displaystyle\sum_{k=1}^{N} x_k \sin[\omega(t_k - \tau)]\right]^2}{\displaystyle\sum_{k=1}^{N} \sin^2[\omega(t_k - \tau)]} \tag{2.14}$$

Note that except for an additive constant, SSE(ω)$_{min}$ has exactly the same form (except for some minus sign) as P(ω). One can see that when the periodogram is at a maximum, the sum of squares of the residuals to the sine wave fit, Equation (2.10), is minimized. So the results derived from least-squares harmonic analysis and the periodogram are equivalent.

2.7.3. Definition of the Parameter τ and Time Invariance

The parameter τ was introduced by Lomb to simplify the solution of the Equations in (2.11). Using the double angle identity for the sine function, the condition in (2.12) can be rewritten as

$$\sum_{k=1}^{N} \sin[2\omega(t_k-\tau)] = 0 \tag{2.15}$$

If one expands the sum in the argument of the sine function one is lead to the expression for τ:

$$\tan(2\omega\tau) = \frac{\sum\limits_{k=1}^{N} \sin(2\omega t_k)}{\sum\limits_{k=1}^{N} \cos(2\omega t_k)} \tag{2.16}$$

The parameter τ has the additional property in that the periodogram becomes invariant to translations of the time origin. That is if $t_k \rightarrow t_k+T$ then $\tau \rightarrow \tau+T$. This property is easy to show. Merely replace t_k with t_k+T and carry out the expansion:

$$\frac{\sum\limits_{k=1}^{N} \sin[2\omega(t_k+T)]}{\sum\limits_{k=1}^{N} \cos[(2\omega(t_k-T)]} = \frac{\cos(2\omega T)\sum\limits_{k=1}^{N} \sin(2\omega t_k) + \sin(2\omega T)\sum\limits_{k=1}^{N} \cos(2\omega t_k)}{\cos(2\omega T)\sum\limits_{k=1}^{N} \cos(2\omega t_k) + \sin(2\omega T)\sum\limits_{k=1}^{N} \sin(2\omega t_k)} \tag{2.17}$$

Divide numerator and denominator by $\cos(2\omega T)\sum\limits_{k=1}^{N} \cos(2\omega t_k)$ to obtain

$$\frac{\tan(2\omega\tau)+\tan(2\omega T)}{1-\tan(2\omega\tau)\tan(2\omega T)} = \tan[2\omega(\tau+T)] \tag{2.18}$$

which completes the proof.

CHAPTER 3

Ion Velocity Differences

3.1. Introduction

The first two chapters dealt exclusively with the solar wind protons. In this chapter, I also discuss alpha particles and the relation of their motion to that of the protons. The next section focuses on the velocity differences of protons and alpha particles and how those differences relate to the interplanetary magnetic field (IMF), and the Alfvén speed[5] which is a measure of the speed of a transverse wave along the IMF. The final section will deal with proton double streaming (two proton distributions) and will contrast this with the motion of protons relative to alpha particles.

3.2. Alpha Particles

Alpha particles make up about 5% (by number) of the solar wind. They were first identified as the source of the second peak in the Mariner 2 solar wind energy-per-charge spectra by assuming that they traveled at the same speed as the protons [*Neugebauer and Snyder*, 1966]. It was also assumed the helium would be doubly ionized after its passage through the solar corona at ~2×10^6 K. This which corresponds to an electron energy of 170 eV (more than enough to ionize helium into alpha particles).

---

5 The Alfvén speed is defined as $|\vec{B}|/\sqrt{4\pi\rho}$ where $|\vec{B}|$ is the magnitude of the IMF, and ρ is the plasma mass density.

Since the PLS instrument is an electrostatic instrument that measures energy-per-charge, E/q, the technique mentioned in the preceding paragraph is used to identify alpha particles in the Voyager ion spectra. The alpha particles lie at twice the energy-per-charge of the protons as mentioned in Chapter 1, so their identification is relatively easy. Once identified, the same fit procedure that is done to the protons is applied to the alpha particles.

Fitting allows an accurate determination of the alpha particles velocity provided the proton thermal speed is not too great (say not more than ~50 km/s), otherwise the proton signal will so overlap the alpha particle signal that accurate determination of the alpha particle velocity may be difficult, if not impossible. (Figure 3.1). Such a situation may occur, for example, as a result of an interplanetary shock when a faster stream of solar wind overtakes a slower one. In this case the ions from the two streams collide and heat up causing the wide ion signals seen in Figure 3.1.

In the section I present observations of proton and alpha particle velocities when the solar wind protons are cool enough to allow accurate determination of the alpha particle velocities. I investigated vector velocity differences and the alignment of those differences with the IMF. I also compared the magnitude of these velocity differences to the local Alfvén speed.

3.3. Proton and Alpha Particle Velocity Differences

Although it is assumed for purposes of identification that the alpha particles have the same velocity as the protons, it turns out that the alpha particles (and other minor ions
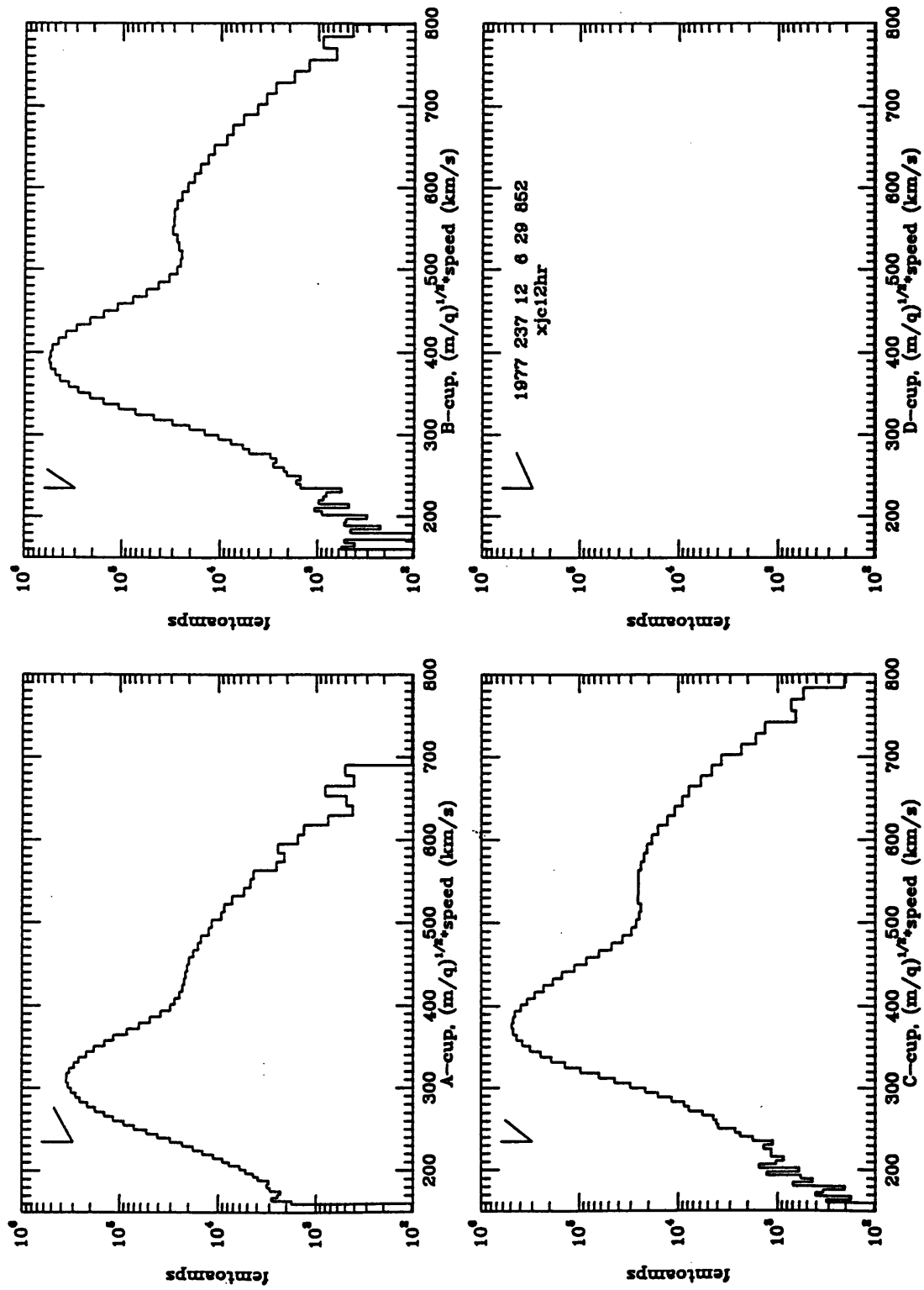
Figure 3.1. Spectrum showing He^{+2} overlapped by hot H^{+}.

such as O^{+6}) and protons travel at different velocities with the alpha particles moving faster. Various mechanisms such as Coulomb drag (the transfer of momentum between ions due to Coulomb collisions [*Bochsler and Geiss*, 1986]), have been proposed to explain why the heavier ions should travel faster than the protons, but so far none has proved totally satisfactory.

The alpha particles velocity cannot differ in an arbitrary way from the proton velocity; any difference must lie along the IMF, $\vec{B}$. That is

$$\Delta\vec{v}_{HeH} = \vec{v}_{He} - \vec{v}_H = \pm\Delta v\hat{B} \qquad (3.1)$$

where $\hat{B}$ is the unit vector along the IMF, and $\Delta v = |\vec{v}_{He} - \vec{v}_H|$. The plus (minus) sign is taken if $\Delta\vec{v}$ is (anti)parallel to $\hat{B}$. The reason why $\Delta\vec{v}$ must lie along $\hat{B}$ is straightforward: the ions and electrons gyrate around magnetic field lines. These gyrations enclose an area containing a quantity of magnetic flux. Now imagine two species of ions gyrating around different but parallel magnetic field lines. If one species of ion tries to move through the other in a direction perpendicular to the magnetic field, the fluxes contained by the ions will change. The changing fluxes will induce currents that resist this change. This is not the case if the two ion species lie on the same field line. In this situation the contained fluxes are unchanged and the ions can move with respect to one another. Since the ions cannot across magnetic field lines, velocity difference must lie along them.

I have checked the alignment of the velocity difference between the protons and alpha particles, $\Delta\vec{v}_{HeH}$, and the IMF, $\vec{B}$, by finding the cosine of the angle between $\Delta\vec{v}_{HeH}$ and $\vec{B}$ for the years 1977-1979 for Voyager 1 and Voyager 2. The results shown in

the top panel of Figure 3.2 reveal the expected alignment of $\Delta\vec{v}_{HeH}$ and $\vec{B}$ in the majority of the cases examined. In fact 74% of the Voyager 1 data and 82% of the Voyager 2 data are within 30° of alignment with the IMF. Many of the unaligned results arise from the distributions of alpha particles and protons not being well separated in energy-per-charge spectra so the direction of $\Delta\vec{v}_{HeH}$ is difficult to determine.

3.4. Velocity Difference and Alfvén Speed

I have noted that the alpha particles often travel faster than the protons. The difference in speed, however, is not arbitrarily large, but is limited by the Alfvén speed V_A (bottom panel of Figure 3.2) which is the speed of a transverse disturbance in the magnetic field traveling along the field line [*Marsch et al.*, 1982][6]. The Alfvén speed depends on the magnitude of the magnetic field and the mass density of the plasma around it. For the solar wind $V_A = 21.83|\vec{B}|/\sqrt{n_H + 4n_{He}}$, where $\vec{B}$ has the units of gammas (10^{-5} gauss), n_H, n_{He} are in cm^{-3}, and V_A is in km/s.

Observations from the Helios 2 spacecraft [*Marsch et al.*, 1982], indicate that between 0.3 and ~1.0 AU, $|\Delta\vec{v}_{HeH}|$ is well aligned with $\vec{B}$, that is the cosine of the angle between $\Delta v v_{\alpha p}$ and $\vec{B}$ is very nearly ±1. During times when the proton bulk speed is greater than about 400 km/s but less than 700 km/s, the magnitude of the velocity difference is about 50 km/s, which is well below the local Alfvén speed of ~150 km/s.

---

6 Why this should be so has not yet been fully quantified.

ALIGNMENT WITH MAGNETIC FIELD
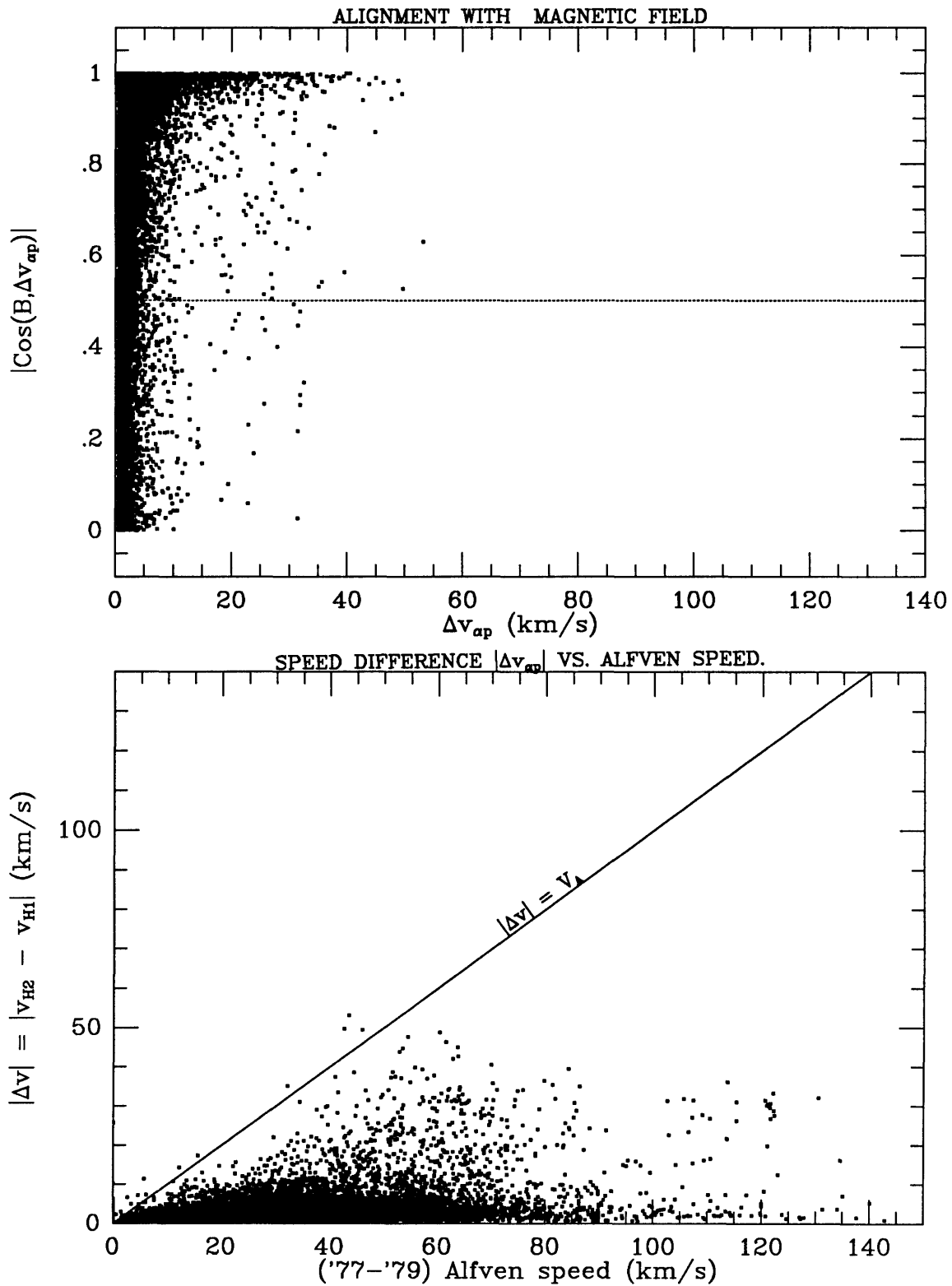
SPEED DIFFERENCE $|\Delta v_{ap}|$ VS. ALFVEN SPEED.

Figure 3.2 Properties of α particle–proton velocity differences

However, when the proton bulk speed is between 700 and 800 km/s, $|\Delta\vec{v}_{HeH}|$ approaches the local Alfvén speed but does not surpass it.

The Voyager 2 data show the results from a distance of 1 AU out to about 5 AU from the Sun. Figure 3.3 consists of four panels, the top one plots the magnitude of the proton and alpha particle velocity difference, $|\Delta v_{HHe}|$. The next panel below shows $|\Delta v_{HHe}|/V_A$. The third panel plots the ratio of the alpha particle number density to the proton number density, and the final panel shows the ratio of the alpha particle and proton thermal speeds. Each of these parameters is plotted against day of year 1977. Figures 3.4 and 3.5 plot the same parameters but for the years 1978 and 1979 respectively. The large gap in the plots for 1979 is due to the Jupiter encounter, when Voyager was in the Jovian magnetosphere.

A word about the selection of the data that went into the previous three plots is in order here. The fitting process gives us the plasma parameters and their uncertainties as well as a goodness of fit, χ^2. The parameters were used only if three criteria were satisfied: the first criterion is that the parameters from a particular fit were used only if the protons and alpha particle distributions were each single Maxwellians (see next section). The next criterion is that the uncertainties in the number density, velocity components, and thermal speed be no greater than 25% of the magnitude of the corresponding parameters. Finally the χ^2 for each ion can be no greater than 95, a number which has been empirically chosen from studying individual spectral fits. Even though these criteria reduce the actual number of data points used, much greater confidence can be place in any conclusions made.
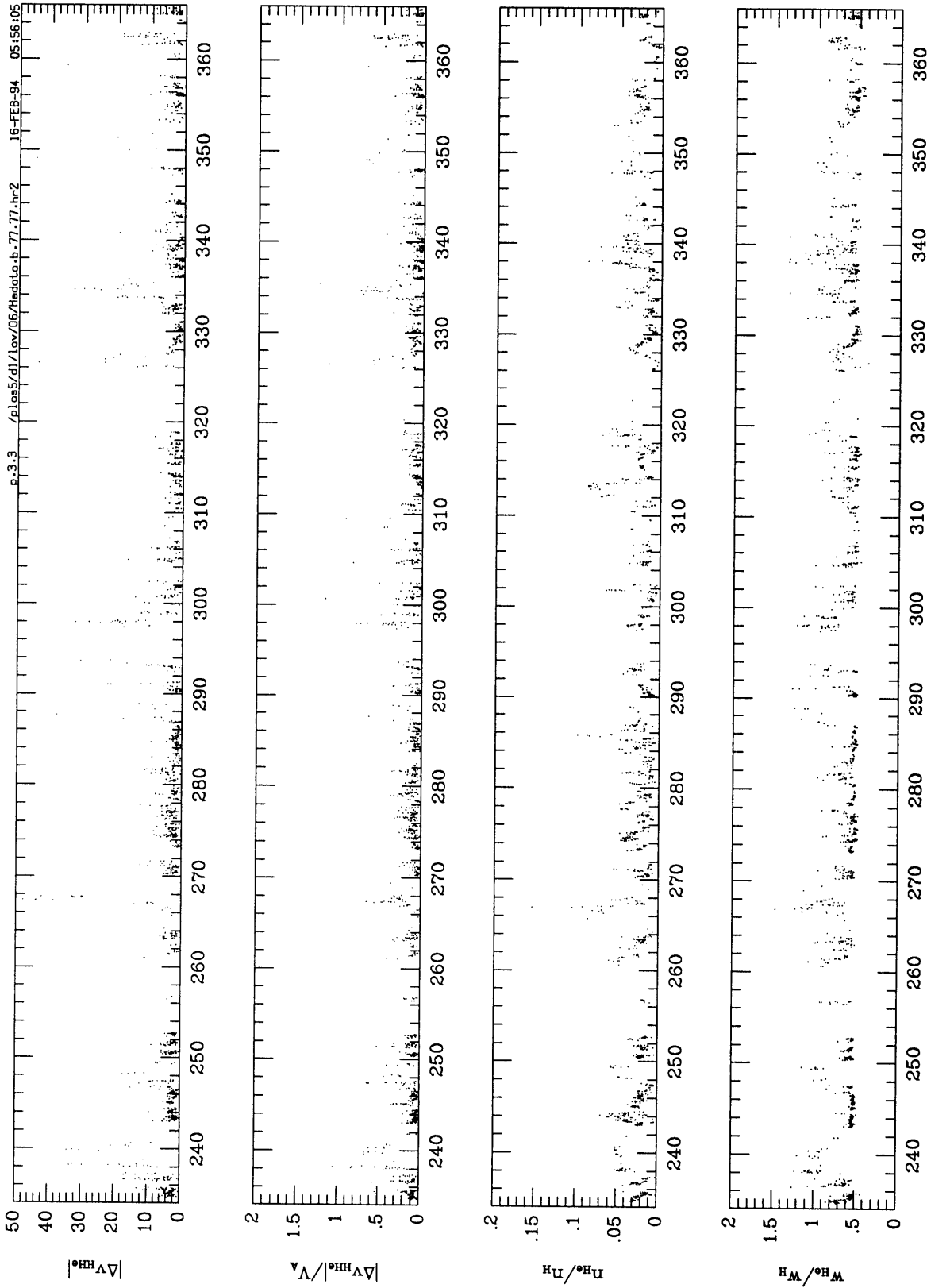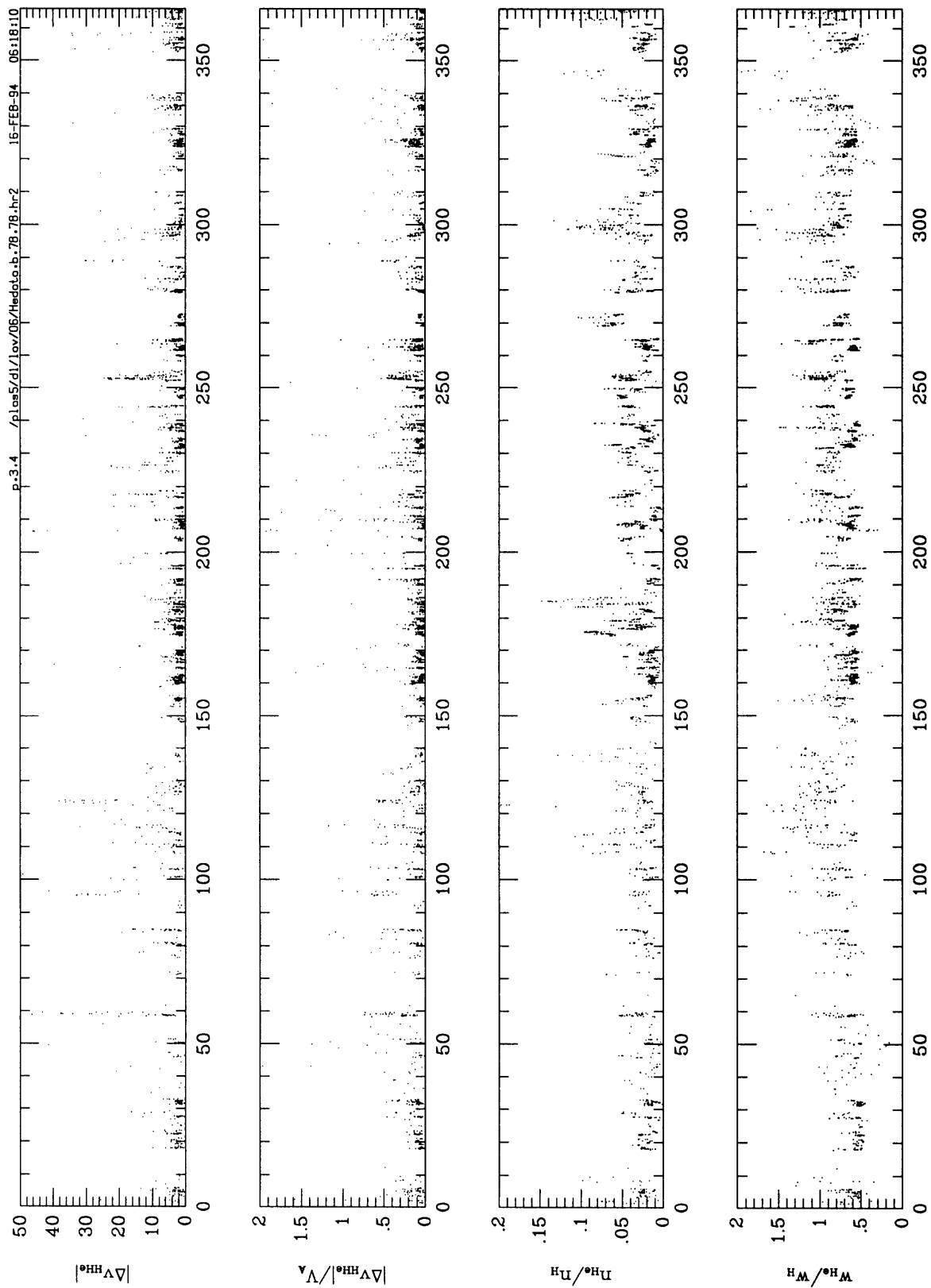
Figure 3.3. He–H parameters plotted against day of 1977.

Figure 3.4. He–H parameters plotted against day of 1978.

61

PAGES (S) MISSING FROM ORIGINAL

These figures show that between 1 and 5 AU, the magnitude of $\Delta\vec{v}_{HHe}$, is usually well below the Alfvén speed. These small velocity differences occur when the solar wind ions are in thermal equilibrium which is shown by $w_{He} = \sim0.5w_H$ (i.e. the ions have equal temperatures), a result that has not been previously reported. Conversely the magnitude of $\Delta\vec{v}_{HHe}$ approaches V_A when the ions have not had a chance to reach an equilibrium state.

The magnitude of $\Delta\vec{v}_{HHe}$ is greatly different from zero when the proton bulk speed is ~500 km/s and greater. I have noted five occasions in 1977 that illustrate this phenomenon: days near 268, 298,320, 334, and 350. At these times the speed of the alpha particles is approximately 20 km/s greater than the proton speed, and the magnitude of the velocity difference reaches 50 km/s. Also the alpha particle thermal speed equals or exceeds the proton thermal speed, and except for day 268, there seems to be no change in the alpha particle number density relative to the proton number density. Why day 268 is an exception is unclear at this time (perhaps it is the result of a CME).

3.5. Proton Double Streaming

I was first alerted to the presence of multiple proton streams by the visual inspection of the Voyager 1 and 2 proton spectra. These spectra showed protons whose velocity distributions were non-Maxwellian. Some were clearly non-Maxwellian, and others were almost indistinguishable from a Maxwellian distribution. The overwhelming majority of these cases involve two proton streams. The remaining cases show

evidence of triple streaming and others that are not so easily classified.

Most of this double streaming behaviors occurs in the inner solar system (< ~5 AU). However, I have spectra that clearly show proton double streaming beyond 5 AU (e.g. in 1986 data near Uranus (20 AU) and beyond Neptune (30 AU) in 1991. Also, when proton double streaming is observed, double streaming in alpha particles is often observed as well[7]. Table 3.1 shows the number of double streaming and single streaming events for protons and alpha particles between 1977 and 1979.

Frequency of Double Streaming

	Voyager 1	Voyager 2
Protons		
Single Peak	17,906	19,531
Double Stream	2,092	2,578
Total	20,456	22,833
Alpha Particles		
Single Peak	11,795	12,808
Double Stream	1,583	2,163
Total	13,378	14,971

Table 3.1

As one can see, proton double streaming occurs ~15% of the time and alpha particle double streaming occurs at least ~8% of the time. The figure for alpha particles is probably larger but their low flux makes it difficult to separate the two streams using the Voyager instrument.

---

7 However, Feldman et al. [1993], using data from IMP 7 and IMP 8, have come to a different conclusion.

Double streaming shows itself as a bump or shoulder attached to what looks like an ordinary Maxwellian signature. The bump may be resolved into a separate peak indicating a great speed difference. I have defined the tallest proton signature as the main signature. If the second proton signature shows itself to the right of the main peak, I call it a right shoulder (RS). If it is to the left, it is a left shoulder (LS). There is another non-Maxwellian signature, which I call a broad peak (BP). At first glance the signature may look Maxwellian, but upon closer inspection, one sees that the sides fall off more rapidly than that of a Maxwellian; the top part is broader than a Maxwellian, hence the name. Figure 3.6 shows a sample of each type of double streaming event. Table 3.2 shows the number and type of double streaming by year from 1977 to 1989 before the Voyager 2 encounter with Neptune. Single stream events (SP) are also included.

Break Down of Numbers of SP, LS, RS, BP by Year

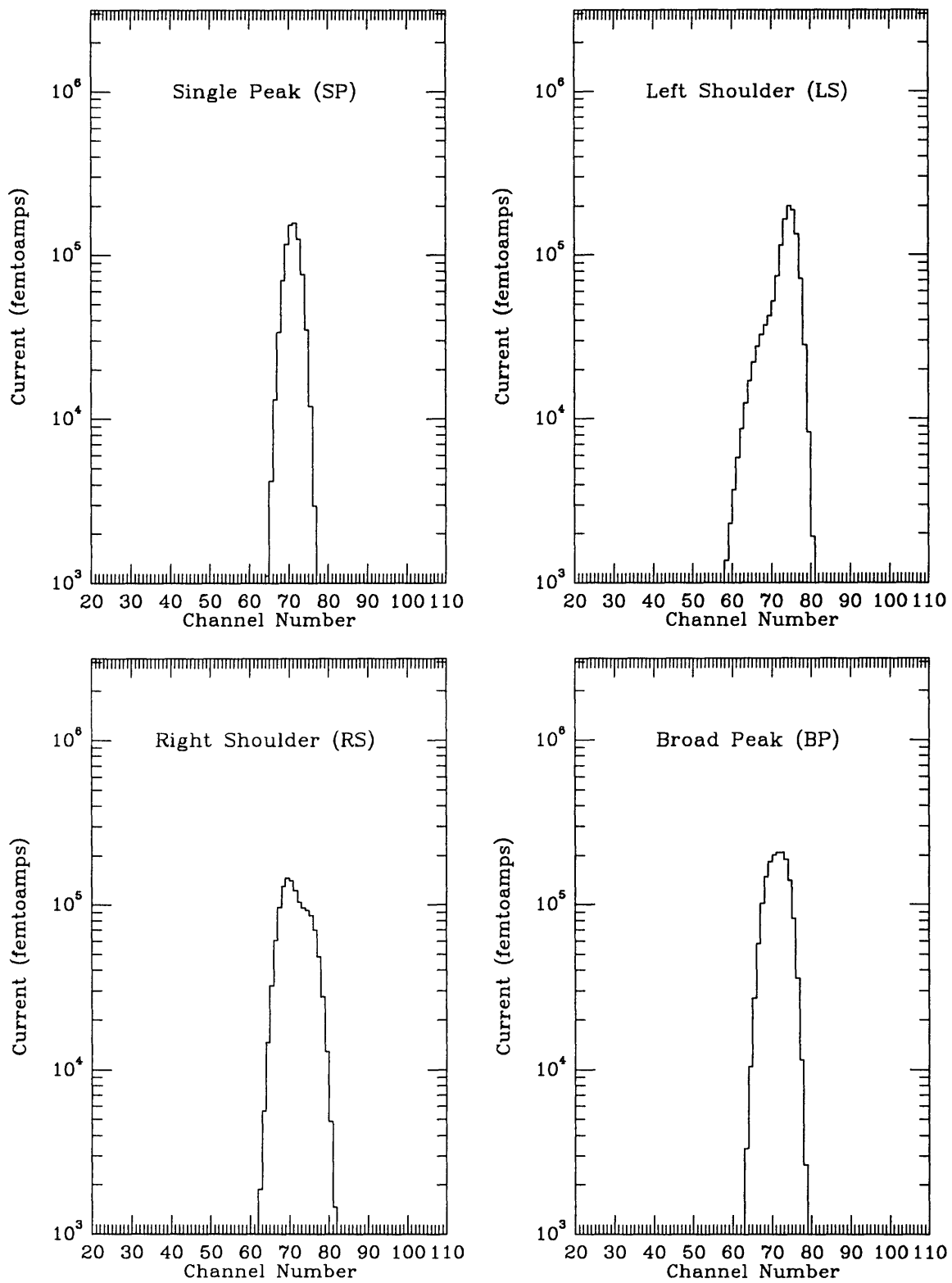| Year	SP	LS	RS	BP	Fraction of total
1977	5234	528	861	366	0.25
1978	12026	912	895	845	0.18
1979	12800	562	426	750	0.11
1980	14589	419	100	439	0.06
1981	15818	354	146	379	0.05
1982	14700	172	151	361	0.04
1983	7076	98	9	141	0.03
1984	4304	66	2	156	0.05
1985	10167	30	4	185	0.02
1986	12807	133	8	175	0.02
1987	14410	55	3	91	0.01
1988	13753	417	2	286	0.05
1989	6976	214	10	125	0.05

Table 3.2

Figure 3.6. Examples of three types of double streaming events with a single stream for comparison.

66

The number of double streaming events does fall with increasing distance from the Sun. I suspect the reason may be that the cooling solar wind and the reduced ion flux (see Section 1.5) combine to produce a narrower signal that cannot be resolved into two proton streams except in cases where the velocity difference is large. Also the number of left shoulder cases clearly dominates in the later years. I believe many of them may be misidentifications.

Although proton signatures of this type are clearly not Maxwellian, I have successfully modeled them as sums of two Maxwellian distributions. This type of model has worked well for most of the double streaming cases. Some cases are are more complex and I cannot model them (e.g. some spectra have "high speed tails" [*Ogilvie*, 1992]).

3.5.1. Proton Speed Difference and the Alfvén Speed

I thought that it would be interesting to compare the proton velocity differences in a way similar to the comparisons of velocity differences between protons and alpha particles (see Section 1.3). The two main points of the velocity difference between protons and alpha particles is that the velocity difference must lie along an IMF line and that the magnitude of the velocity difference is less than or equal to the local Alfvén speed. As one might expect, the velocity difference between two proton streams is aligned with the IMF (Top panel of Figure 3.7). Comparing the magnitude of the velocity difference yielded surprising results. The magnitude of the proton velocity difference often reached twice the Alfvén speed and greater (bottom panel of Figure 3.7). Feldman et al. [1993] also have ion spectra that show proton distributions
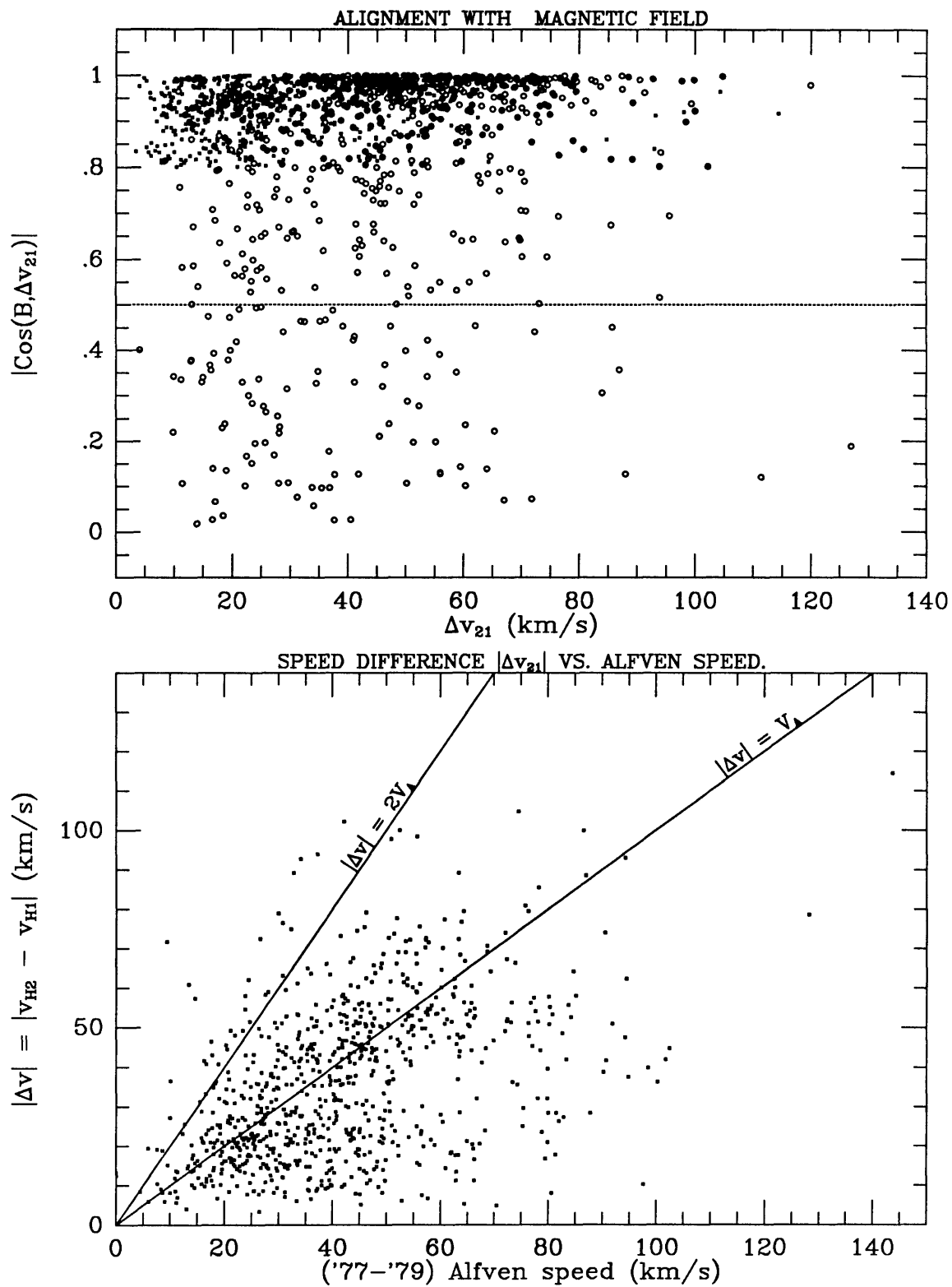
Figure 3.7 Properties of proton–proton velocity differences.

separated by twice the Alfvén speed. Why this should be is not understood at this time. Although an explanation by Joseph Hollweg and Phil Isenberg [private communication] using the center of mass of the two distributions allows the proton speed difference to be as high as twice the Alfvén speed[8], it is not at all clear that it is qualitatively correct, or if it is, why the explanation cannot be applied to proton and alpha particle speed differences.

I have so far made preliminary investigations into the solar wind conditions in which double streaming may occur. I have looked at normalized density, speed, thermal speed, and heliocentric distance to see if there is a relation between these parameters and double streaming. I expected to find something like "double streaming protons occur in high speed streams". So far I have found no such relation.

3.5.2. Models for Proton Double Streaming

There are two main postulated causes of proton double streaming: mixing of streams, and runaway high speed protons not isotropised by Coulomb collisions. The first possible cause is fairly straightforward. Two (or more) streams can interact with each other, provided their magnetic fields are aligned. The two streams are emitted at two different times with one stream overtaking another. The other possibility involves Coulomb collisions[9]. The solar wind protons undergo Coulomb collisions as they expand into the solar system. If there are many such collisions in the time it takes the

---

8 For double streaming events the mass density ρ contains contributions from both proton distributions and what ever alpha particle distributions are present.

9 The information for this paragraph and the following four comes from [Levi and March, 1986].

solar wind to reach perhaps half an AU, then the solar wind will thermalize and have a Maxwellian distribution. If there are few collisions during the solar wind's flight through half an AU, then those protons with speeds greater than the bulk will "run away" and form a second distribution (exactly how this second distribution is formed is unclear).

This competition between collisions and expansion can be quantified. Let τ_e be the expansion time, the time it takes a radially expanding corona to expand through some characteristic distance at a constant speed v. From the definition of τ_e [*Hundhausen,*, 1972] this distance is taken to be 0.5 AU for observations made at Earth orbit. For arbitrary heliospheric distances τ_e is equal to r/2v where r is the distance from the Sun and v is the solar wind bulk speed.

The collision time τ_c is the time it takes particles of different temperatures to come to the same temperature. τ_c is proportional to $T^{3/2}/n$ where T is the kinetic particle temperature and n is the particle number density.

The competition between expansion and collision is given by the ratio $\tau_e/\tau_c = N$. If N is larger than 10, the protons will suffer enough collisions to have become thermalized during their expansion from the Sun. The particle velocity distribution would therefore be Maxwellian. If N < 10, then there would not be enough collisions to keep the protons thermalized by the time the solar wind reaches Earth orbit. In this case, the faster protons could "run away" to form a non-Maxwellian distribution.

70

3.6. Conclusion

I analyzed velocity differences between solar wind protons and alpha particles, and have noted that these differences are aligned with the IMF and that the magnitudes are bounded by the local Alfvén speed. In fact, most of the time the magnitudes of the velocity differences are well below the local Alfvén speed, and at these times, the protons and alpha particles are in thermal equilibrium. I also analyzed velocity differences between two proton populations during double streaming events and found that these differences are also aligned with the IMF, but that the magnitudes are not bounded by the local Alfvén speed and can exceed it by a factor of 2.

Proton double streaming reveals itself in the ion spectra as a proton distribution that appears nonMaxwellian. I divided proton double streaming events into three categories based on the appearance of the proton distribution. Analysis of these categories revealed that the number of proton double streaming events decreases with increasing distance from the Sun and that during proton double streaming alpha particle double steaming occurs about half the time. I believe that the alpha particles may double stream whenever the protons do, but the low flux of these ions makes separating the two streams difficult.

Unfortunately at this time, I have been unable to use results from the Voyager data to decide between either model for proton double streaming or even if both models should be rejected in favor of a third.

More work needs to be done correlating the appearance of double stream events with

other solar wind phenomena such as CME's, flares, and shock. Work also should be done on the fitting program to ensure the correct identification of proton double streams and to improve the identification of alpha particle double streams.

CHAPTER 4

O^{+6} and Other Minor Ions

4.1. Introduction

Minor ions in the solar wind have been studied for more than 20 years [e.g. *Bame, et al.*, 1968, 1970; *Bame*, 1983]. Just as oxygen is the third most abundant constituent in the corona and the cosmos at large, it is the third most abundant constituent of the solar wind [*Bochsler and Geiss*, 1990].

One of the most comprehensive studies of oxygen and other minor ions was carried out by *Bochsler et al.* [1985] using observations from the ion composition instrument (ICI) on the ISEE 3 satellite (later called ISEE 3/ICE) obtained between 1978 and 1982. They studied minor ions in the solar wind with emphasis on the ions O^{+6}, O^{+7}, C^{+5}, and Ne^{+8} and compared their abundances to that of He^{+2}.

During my study of solar wind, one of my colleagues[10] suggested that the signatures of O^{+6} and other minor ions appeared to be present in some of the Voyager ion data. Since the high-resolution data of the Voyager plasma science (PLS) experiments is comparable to the low-resolution data that comprise most of the ISEE 3 data, direct comparisons of observations from ISEE 3 and Voyager were possible.

The data base used in this study was derived from the ion spectra taken from both

---

10 Ralph McNutt Jr. who is currently at the American Physcal Laboratories.

73

Voyagers. The period covered ranges from launch to day 52 of 1979 for both spacecraft. A period from days 48 through 140 of 1978 is excluded for Voyager 1 due to the aforementioned instrument failure.

O^{+6} was observed in about 10% of the 66,356 spectral sets that were analyzed. From among those 10%, I chose the ones that exhibited the clearest signal (the criteria for selection are in the appendix). The total number of sets used in the O^{+6}/minor ion analysis was 1690 or ~2.5% of the total data set.

In this chapter I study the relationship between the flux densities, nV (n is the ion number density and V is the ion speed) of the oxygen ions O^{+6} and O^{+7} and He^{+2} in the solar wind from launch in late 1977 to early 1979 (prior to the Jupiter encounters). For comparison of yearly data, the flux densities are approximately normalized by multiplying them by the square of the spacecraft distance from the Sun in AU. The use of flux densities as well as number densities enables me to make a direct comparison between my results and those of *Bochsler et al.* [1985] or others (e.g., Apollo foil experiments, see *Bochsler et al.* [1989] and references therein). I also study the temporal variation of the ratios, $[He^{+2}]/[H^+]$, $[H^+]/[O^{+6}]$, and $[He^{+2}]/[O^{+6}]$ (where [X] is the number density, cm^{-3}, of ionic species X).

For high-Mach-number flows, the minor ions, together with He^{+2} and H^+, can be detected in a single instrument energy scan. Hence it seemed worthwhile to pursue possible Voyager contributions to the data base of minor ion observations. The Voyager instruments have detected O^{+6} without the use of spectrum averaging out to at

least 6 AU; with averaging, the instrument on Voyager 2 can sometimes detect O^{+6} at least as far as the orbit of Neptune.

I describe the Voyager PLS experiment in some detail and then discuss the observations made with it. Along with minor ion observations, I include a summary of the solar wind proton and alpha particle observations during each of the three years covered by the study (about 1.5 years of near-continuous data). I describe the ion models used by *Bochsler et al.* [1985] and myself and then compare the results from those models.

Finally, in the last section, I include a description of the procedure used to fit the ion spectra in the PLS data base for the period of study.

4.2. The PLS Instrument

The Voyager PLS experiment has already been described in Chapter 1 as being capable of identifying O^{+6} in the solar wind provided the Mach number (ratio of solar wind proton speed into the main sensor to proton thermal speed) is greater than ~15. However, the instrument cannot resolve other minor ions such as O^{+7}, N^{+6}, and C^{+5} (mass to charge ratios m/q of 2.29, 2.33, and 2.40 respectively). In this respect, the Voyager PLS performance is comparable to that of the low-resolution m/q mode of the ion composition instrument on ISEE 3 (3.6% in the range of 1.4 < m/q < 5.8, see *Bochsler et al.* [1985]). If the solar wind is too warm, the widths of the He^{+2} and the unresolved O^{+7}, N^{+6}, and C^{+5} velocity distributions become so great that they mask the presence of the O^{+6} distribution. Still even at large heliocentric distances O^{+6} can be detected

75

by averaging spectra.

The Voyager PLS experiments provide an additional source of information about the solar wind composition near 1 AU during 1977 when the ratio $[He^{+2}]/[H^+]$ was at a minimum in its variation with the solar cycle [Ogilvie, 1985]. From this minimum in 1977, the ratio $[He^{+2}]/[H^+]$ increased sharply during 1978 and 1979 and reached a maximum in 1979 [Ogilvie, 1985]. The Voyager observations presented here provide an opportunity to determine the ratio $[He^{+2}]/[O^{+6}]$ during that portion of the solar cycle.

4.3. Minor Ion Identification

In Figure 4.1, I show one complete spectral set in the form of ion current versus E/q for each of the three cups comprising the main sensor. For the work reported here, I first assume that all ion distributions travel at nearly the same convective velocity. Under this assumption the energy per charge spectra can be interpreted in terms of the mass to charge ratios of the solar wind constituents. Although significant (up to the Alfvén speed) differences in solar wind proton and alpha particle velocities can occur along the local magnetic field [Marsch et al., 1982], the minor species tend to move with the alpha particles. This nearly common velocity has been found for O^{+6} [Ogilvie et al., 1982], Fe ions in low-speed flows [Ipavich et al., 1986; Schmid et al., 1987], and Si ions in low-speed wind [Bochsler, 1989]. I note here that the assumption of nearly equal velocities is borne out by the fits.

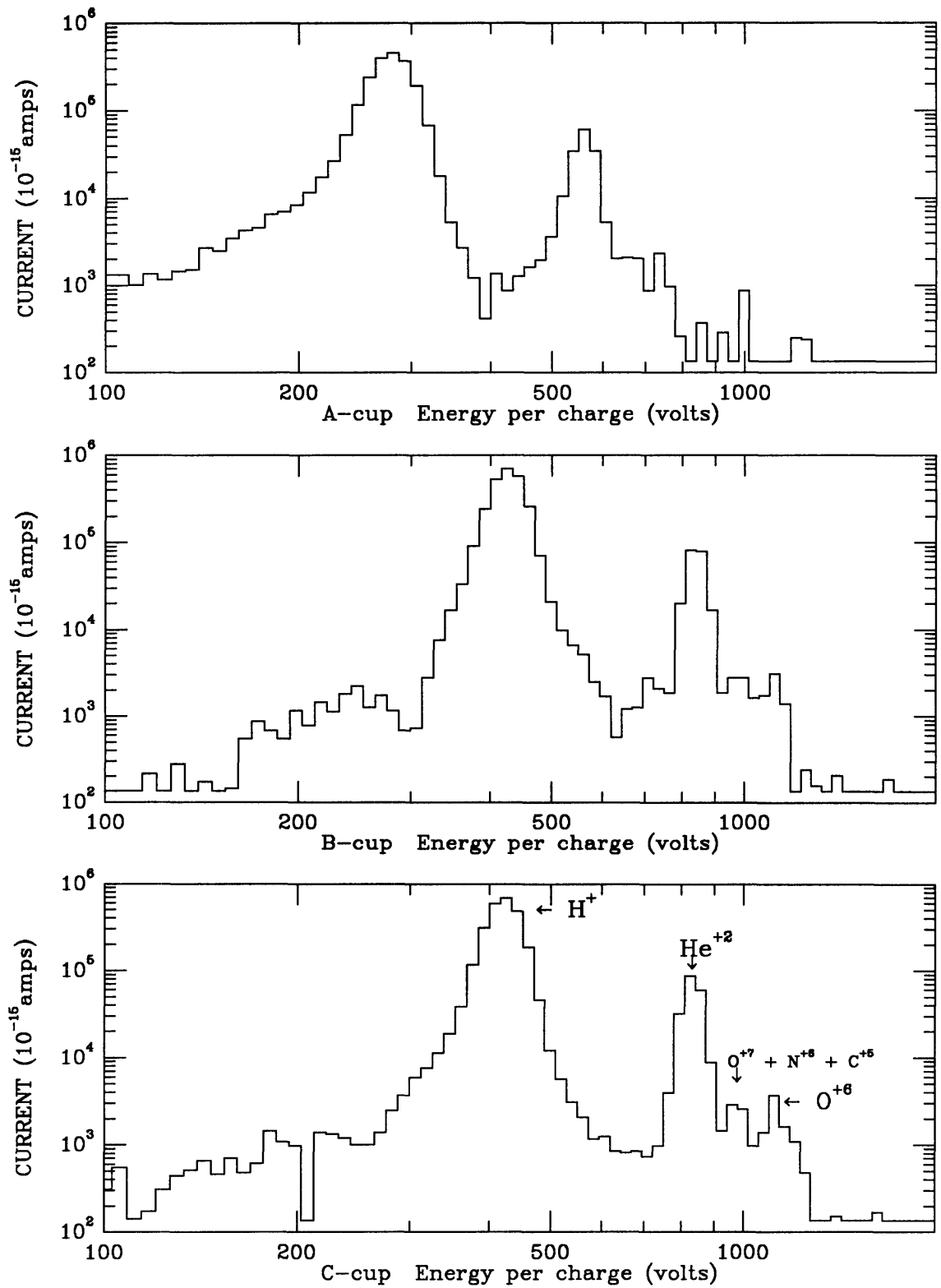At the time of the measurement shown in Figure 4.1, Voyager 2 was 1.0 AU from the

76

Figure 4.1 Voyager M—mode spectrum showing various ion signatures.

Sun. The C cup was pointing most directly into the solar wind, so the ion E/q values have the highest values in that cup. The H^+ peak predominates at an E/q of ~420 V. At about twice this E/q value lies the He^{+2} peak. The peak near 1120 V is consistent with O^{+6}. The peak between He^{+2} and O^{+6} is likely to be dominated by O^{+7}, N^{+6}, and C^{+5} [cf. *Bochsler et al.*, 1986, Figure 1]. The low-energy tail on the proton distribution (which is most pronounced in the A cup) is largely an artifact of the response of the Faraday cup to solar wind entering the cup at a steep angle relative to the cup normal [*Barnett and Olbert*, 1986].

Even though the Voyager PLS instrument can distinguish ions only by energy per charge, one can see that the assumed O^{+6} peak occurs in the correct position relative to the proton peak and that it shifts in energy as the proton peak shifts. (For Figure 4.1, the expected position for O^{+6} is 1175 V). The only likely "contamination" is by ions with mass to charge ratios near 2.67 such as Ne^{+8}, which are too low in abundance to be detected [*Bochsler and Geiss*, 1990].

4.4. Proton and Alpha Particle Observations

To look for biases in the minor ion data set, I first examined the H^+ and He^{+2} parameters determined by the Voyager observations between 1977 and 1979, then compared bulk properties observed when there was a clear O^{+6} signature with bulk properties observed at all other times. The histograms displayed in Figures 4.2 and 4.3 (with means and standard deviations given in Table 4.1 summarize the H^+ observations from Voyagers 1 and 2 respectively. Both sets of histograms have identical
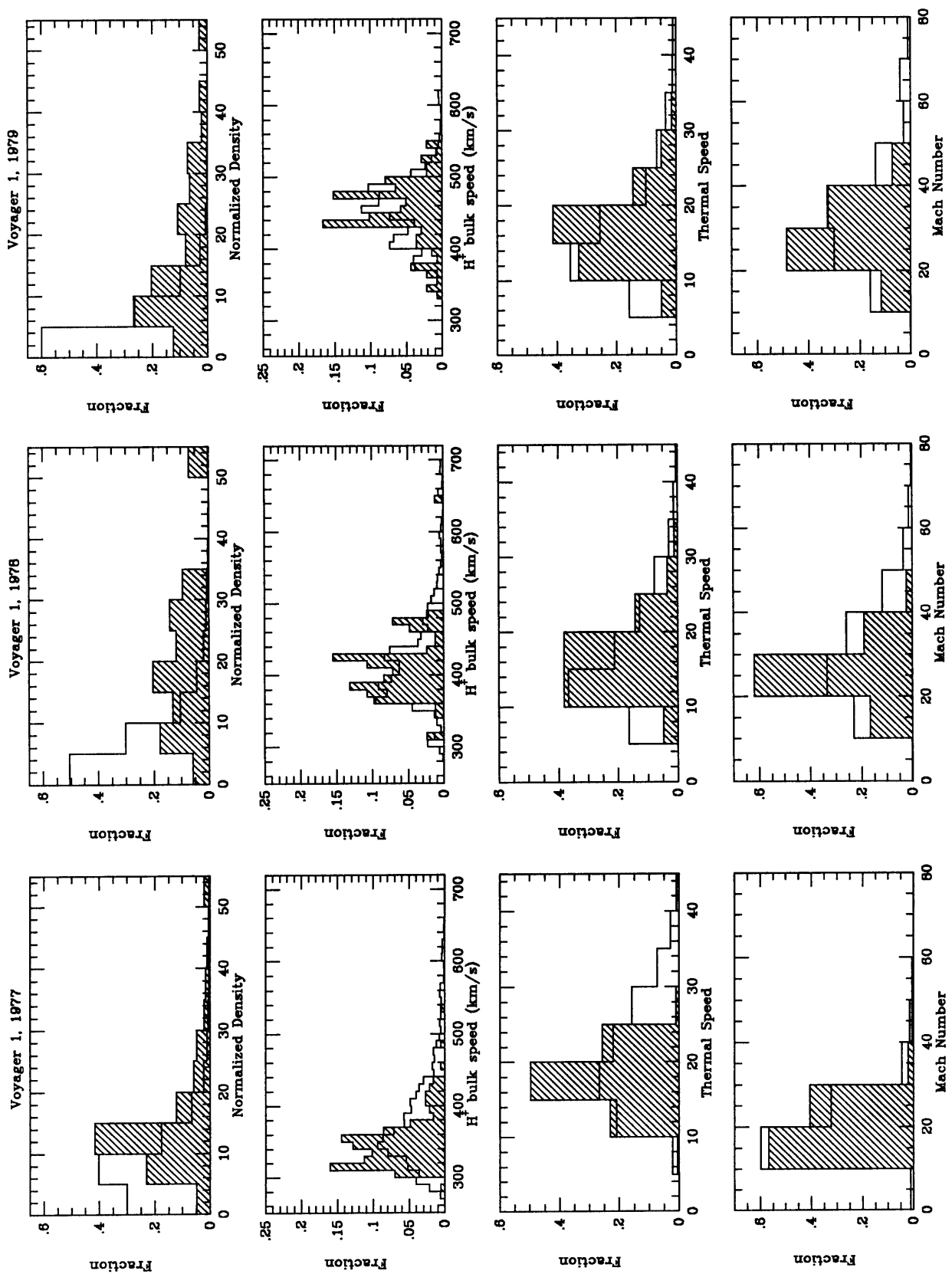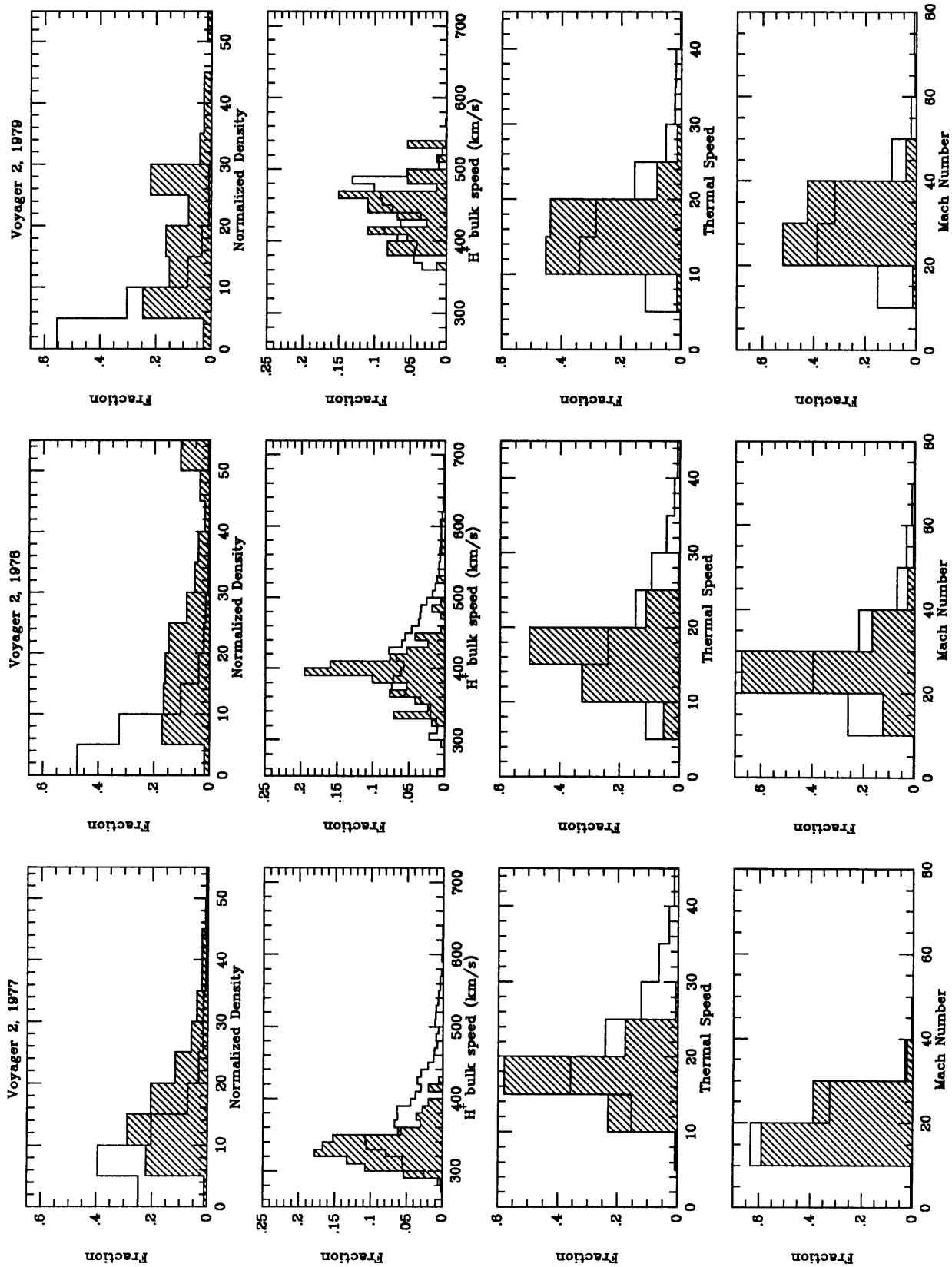
Figure 4.2 Voyager 1 Yearly H⁺ Histograms 1977–1979.

79

Figure 4.3 Voyager 2 Yearly H⁺ Histograms 1977-1979.

80

Voyager 1 H⁺ Parameters

	All Protons						Protons With O^{+6} Present				
	n	V	w_{th}	M	N		n	V	w_{th}	M	N
1977											
Mean	8.85	379.3	21.3	19.8	6,708		15.3	349.1	17.6	20.6	374
σ	6.9	66.9	8.0	6.9			10.2	36.6	3.8	4.8	
1978											
Mean	6.87	418.1	16.4	29.6	11,583		21.5	409.3	16.4	26.4	168
σ	6.7	66.3	7.1	11.6			17.3	45.3	4.5	6.1	
1979											
Mean	6.34	443.8	16.0	32.1	3,619		16.4	451.6	16.6	28.9	73
σ	6.4	57.3	7.4	11.5			12.3	43.9	4.5	7.3	

Voyager 2 H⁺ Parameters

	All Protons						Protons With O^{+6} Present				
	n	V	w_{th}	M	N		n	V	w_{th}	M	N
1977											
Mean	9.76	375.8	21.2	19.1	7,042		17.3	335.1	17.2	20.1	706
σ	8.6	68.6	7.9	11.4			11.5	26.6	3.1	3.9	
1978											
Mean	7.46	426.6	17.9	27.7	17,305		27.7	398.1	16.0	25.9	339
σ	8.6	68.6	7.9	11.4			29.2	43.4	3.4	6.0	
1979											
Mean	6.63	443.2	16.9	30.1	2,493		18.9	443.7	15.5	29.7	54
σ	6.6	50.8	7.3	10.8			10.8	39.9	3.2	6.1	

Table 4.1. Voyager proton parameters, where n is the proton number density in cm^{-3}; V is the proton speed in kilometers per second; w_{th} is the proton thermal speed in kilometers per second; M is the Mach number defined by $M \equiv V/w_{th}$; N is the number of data points.

formats and give distributions of the proton number density, bulk speed, thermal speed, and Mach number, for each year of the data. The densities are approximately normalized to 1 AU by multiplying by the square of the spacecraft heliocentric distance. The value of the quantity displayed is indicated on the horizontal axis and the number fraction on the vertical axis. The subset of proton data which contains a distinct O^{+6} peak is indicated by the hatched region.

The proton density distributions for the two Voyager sets show some differences. The normalized density for the solar wind protons is generally less than 20 cm^{-3}. There are a few times in 1978 (Voyager 2) when the normalized density rises to over 100 cm^{-3} (there is a gap in the Voyager 1 data during the time of these high densities.) However, for each spacecraft, when O^{+6} is seen the mean densities of the protons are larger, and they form a flatter distribution than the solar wind protons in general, especially in the last two years.

The bulk speed histograms reveal that the average solar wind speed is increasing over the 1.5 year period of the study, as expected from the phase of the solar cycle [*Feldman et al.*, 1978]. During each of the three calendar years, many of the spectra containing resolved O^{+6} values come from a broad range of speeds, although the Voyager 2 1978 values come from a narrower speed range.

The proton thermal speeds ($w_{th} \equiv \sqrt{2\,kT/m}$) exhibit a similar range for all 3 years. There is an upper cutoff of ~25 km s^{-1} in thermal speed for those spectra for which the O^{+6} signature is present, since I cannot fit O^{+6} parameters when the solar wind is

"warm" due to overlap from the He^{+2} peak. In general, the thermal speeds decrease with time as Voyager recedes from the Sun [e.g., *Gazis*, 1984; *Gazis et al.*, 1989].

The final row of plots shows the proton Mach number by year. The Mach number increases with spacecraft heliocentric distance for both the overall and subset populations. This increase is expected since the solar wind cools while its speed remains relatively constant.

In summary, in 1977 the warmest solar wind is excluded, and in 1978 and 1979 some low density wind is excluded from the analysis of O^{+6} properties.

I have formed similar histogram plots for the He^{+2} parameters for the 1.5-year period investigated and show them in Figures 4.4 and 4.5 (means and standard deviations are given in Table 4.2. In this case, there are significant differences between the family of all He^{+2} parameters and the subset corresponding to spectra in which an analyzable O^{+6} signature is present. The density plots indicate that there are significantly fewer determinations of O^{+6} parameters when the He^{+2} density is low than there are cases in the parent population.

In general, spectra with clear O^{+6} signatures are characterized by cooler solar wind temperatures associated with a denser and slower wind, as shown in Figures 4.2-4.5. Also, as shown in Figure 4.6, in most of the spectra exhibiting an O^{+6} signature, the major ions tend to have the same temperature. In contrast, the temperature relation of the major ions generally covers the range from equality to $T_{He} = 4T_H$. Therefore the results presented below are biased with respect to "average" solar wind conditions.
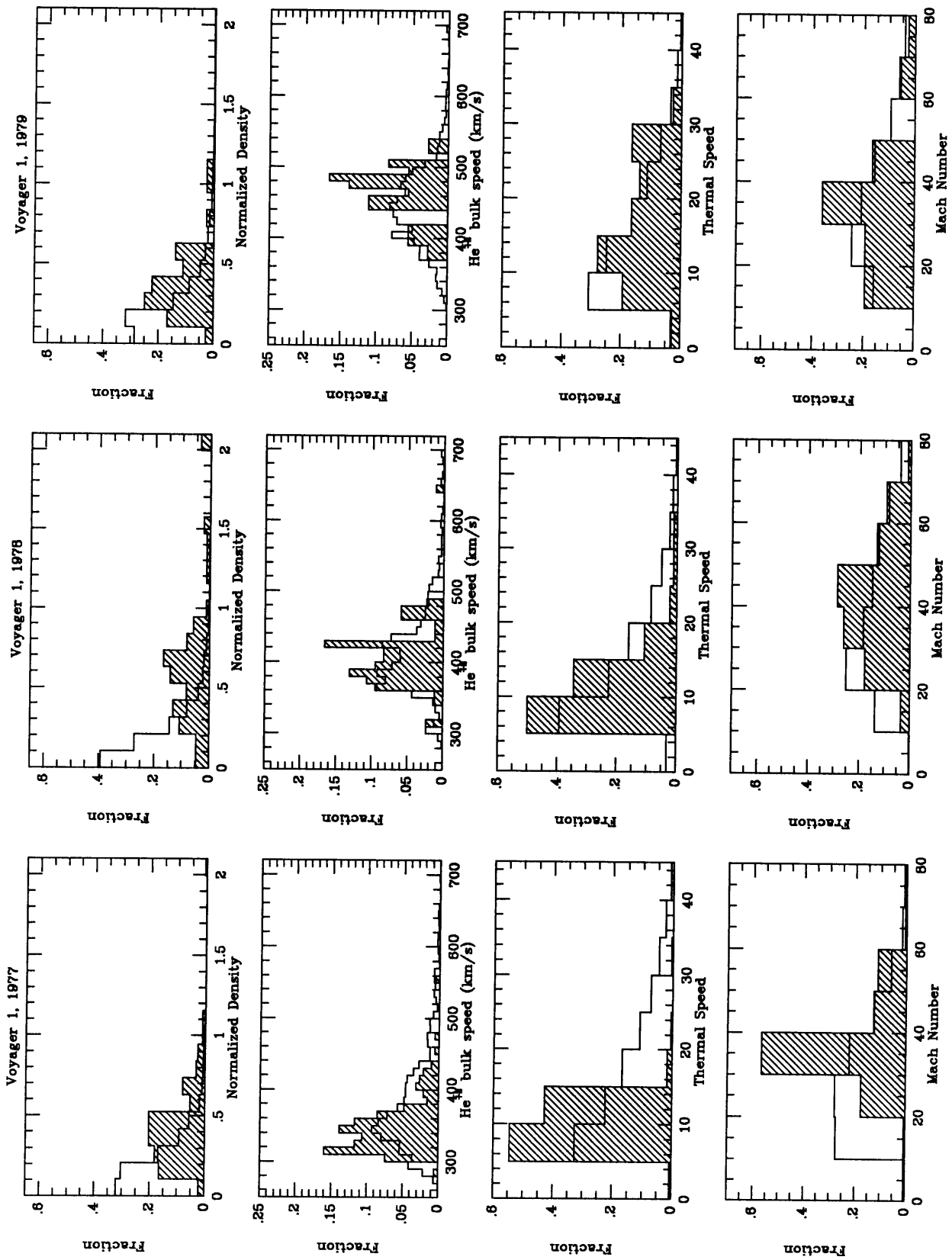
83

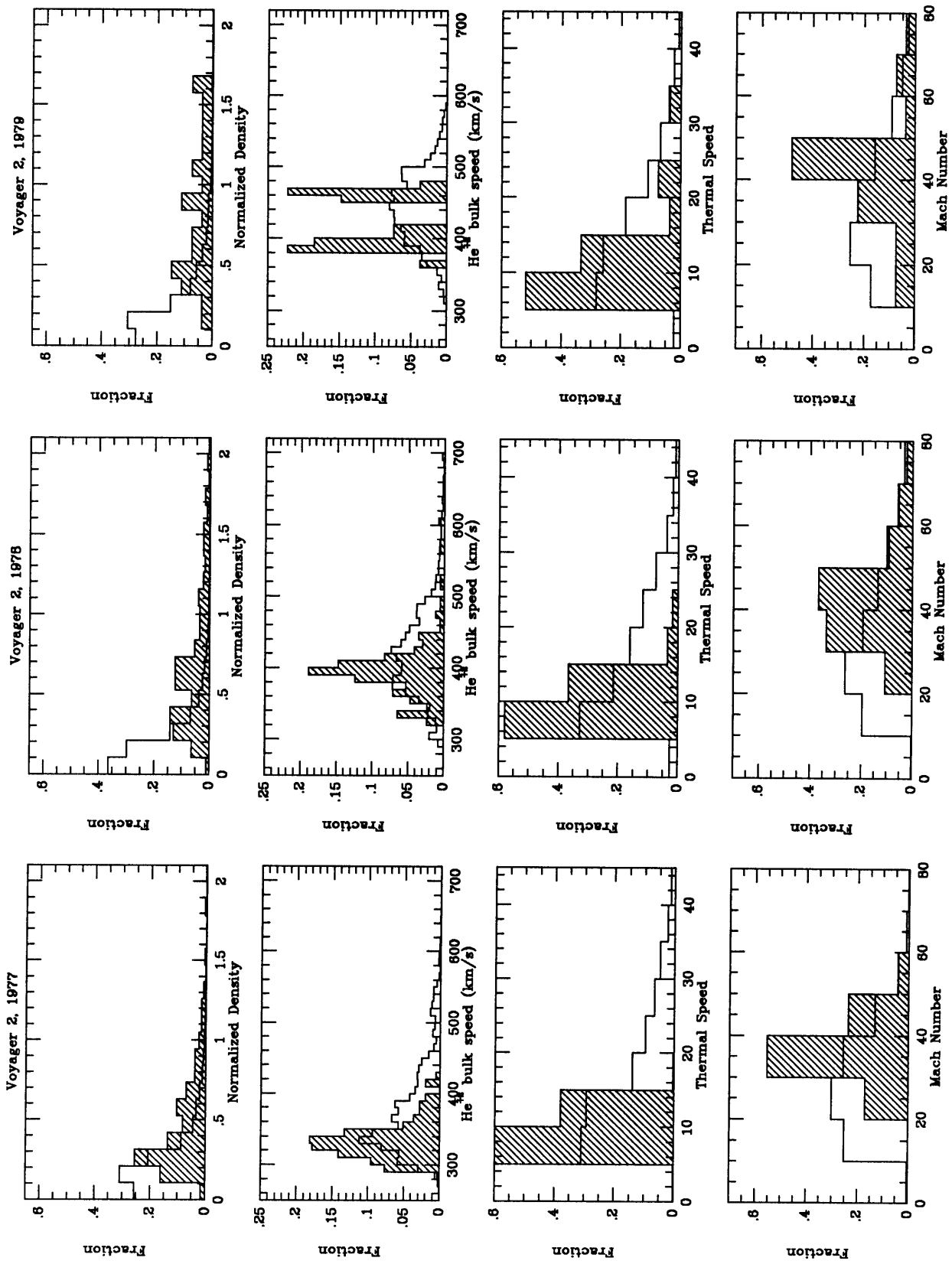Figure 4.4 Voyager 1 Yearly He^{+2} Histograms 1977–1979.

84

Figure 4.5 Voyager 2 Yearly He^{+2} Histograms 1977–1979.

85

Voyager 1 He^{+2} Parameters

	All Alpha Particles						Alpha Particles With O^{+6} Present				
	n	V	w_{th}	M	N		n	V	w_{th}	M	N
1977											
Mean	0.205	380.3	16.0	30.1	6,708		0.410	348.1	9.9	37.0	374
σ	0.190	69.0	9.3	39.3			0.310	36.8	2	9	8.7
1978											
Mean	0.198	418.7	13.8	39.3	11,583		0.638	408.9	11.2	41.3	168
σ	0.212	66.8	8.3	18.4			0.475	45.3	5.0	13.1	
1979											
Mean	0.262	444.5	15.0	38.1	3,619		0.839	451.8	14.0	39.8	73
σ	0.374	57.8	8.3	18.5			0.911	43.6	7.1	17.8	

Voyager 2 He^{+2} Parameters

	All Alpha Particles						Alpha Particles With O^{+6} Present				
	n	V	w_{th}	M	N		n	V	w_{th}	M	N
1977											
Mean	0.235	376.3	15.8	29.3	7,042		0.461	333.9	9.5	36.5	706
σ	0.219	64.3	8.9	11.9			0.357	26.7	1.9	6.9	
1978											
Mean	0.219	427.1	15.5	36.2	17,305		0.695	397.1	10.0	42.5	339
σ	0.276	69.2	9.2	18.5			0.504	43.4	3.0	11.0	
1979											
Mean	0.274	444.5	15.7	36.3	2,493		0.942	443.1	11.2	44.9	54
σ	0.345	51.4	8.6	17.4			0.648	40.1	5.0	13.8	

Table 4.2. Voyager alpha particle parameters, where n is the α particle number density in cm^{-3}; V is the α particle speed in kilometers per second; w_{th} is the α-particle thermal speed in kilometers per second; M is the Mach number defined by M $\equiv$ V/w_{th}; N is the number of data points.
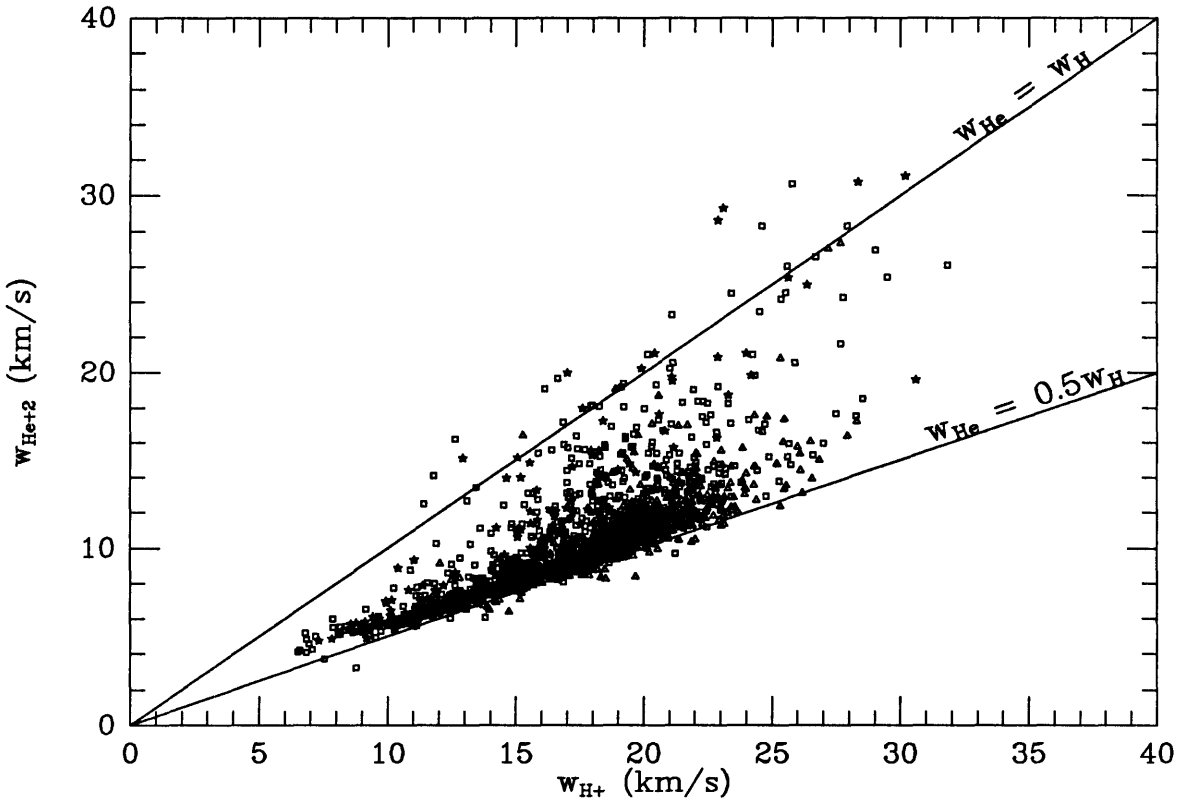
Figure 4.6 H^+ and He^{+2} when O^{+6} is fitted.

Signatures of O^{+6} were observed in about 10% of the spectra examined. The restrictions on Mach number, channel number, and relative uncertainty (see appendix) reduce the number of spectra containing "very clear" O^{+6} signatures to 1690 (~2.5% of the total) from both spacecraft. The two Voyagers are separated in latitude by ~3° and in longitude by ~5°. The distance separation is ~0.5 AU.

4.5. Modeling the Data

My first attempts to determine the plasma parameters for O^{+6} were unsatisfactory. I derived flux densities that were equal to the combined flux densities of O^{+6} and O^{+7} found by *Bochsler et al.* [1985] with ISSE 3 data. The investigation of this problem

revealed that the low flux of O^{+6}, prevented the fitting program from determining the O^{+6} density and thermal speed as accurately as it does for the major ions (i.e. protons and alpha particles). To correct this problem, I increased the number of ions used in the fit by five. Since the PLS instrument cannot clearly resolve the signals of any minor ion except O^{+6}, I looked to the ion model of *Bochsler et al.* [1985] for the initial estimates of the minor ion densities. This model is discussed in the next section, and in the following section is a discussion comparing the two ion models I considered for the computation of the minor ion parameters and which model I decided to use.

4.5.1. The Ion Model of Bochsler and Geiss

The ICI on ISEE 3 uses a stigmatic Wien filter which feeds into a hemispherical electrostatic analyzer. The instrument is capable of cleanly resolving O^{+6} as well as the group consisting of O^{+7}, N^{+6}, C^{+5}, and Mg^{+10} which occupy the m/q range of 2.29 to 2.40 [*Coplan et al.*, 1978]. Almost 50,000 values of the oxygen to helium flux density ratio were derived by fitting to the O^{+6} peak with all other fit parameters constrained (see previous discussion) using 49,000 low-resolution spectra ($\Delta E/E \approx 3.6\%$) and ~1000 high resolution spectra ($\Delta E/E \approx 1.8\%$).

Bochsler et al. [1985] fitted a model to the ICI low-resolution m/q data using the seven minor ions, O^{+6}, O^{+7}, N^{+5}, N^{+6}, C^{+5}, Ne^{+8}, Mg^{+10}, in addition to the ion He^{+2}. All of the ion velocity vectors were set equal to the corresponding He^{+2} velocity vector, and the minor ion thermal speeds were set equal to the O^{+6} thermal speed. The He^{+2} density was a free parameter as was the O^{+6} density. The other ion densities

were constrained to follow an assumed solar wind composition of

$$[C] = [C^{+4}] + [C^{+5}] = 0.63[O]$$

$$[N] = [N^{+5}] + [N^{+6}] = 0.13[O]$$

$$[Ne^{+8}] = 0.15[O]$$

$$[Mg^{+10}] = 0.05[O]$$

where $[O] = [O^{+6}] + [O^{+7}]$ and the ratios $[O^{+7}]/[O^{+6}]$, $[N^{+6}]/[N^{+5}]$, $[C^{+5}]/[C^{+4}]$ were held fixed by assuming a constant coronal temperature of 1.67×10^6 K (note that the corresponding flux density ratios were also held fixed since all ions are constrained to have the same velocity). *Bochsler et al.* [1986] found the average ratio of $[He^{+2}]/[O]$ to be 75 ± 20.

4.5.2. The Equal-Temperature and the Equal-Thermal Speed Models

I fit the Voyager PLS data using two models with six minor ions plus He^{+2}. The ions used were O^{+6}, O^{+7}, N^{+5}, N^{+6}, C^{+5}, and Ne^{+8}. Mg^{+10} was not included because in these models it was indistinguishable from C^{+5} in E/q since the ion masses were taken to be integral multiples of the nucleon mass. Separate velocity vectors were assumed for the He^{+2}, and the O^{+6} ions; the velocities of the other minor ions were set equal to the O^{+6} velocity. The He^{+2} thermal speed was a free parameter in both models.

The two models differed in the assumptions made about the kinetic temperatures of the ions. In the first model, the minor ion thermal speeds were set equal to the O^{+6} thermal speed; i.e., the ion temperatures were proportional to the ion masses (basically the

model of *Bochsler et al.* [1985]). In the second model, all minor ion kinetic temperatures were set equal to the temperature of the He^{+2} ions. Except for the kinetic temperatures, the fitting program used the same procedure to fit the data in both models (see appendix). In particular, I derived number densities and flux densities for O^{+6} and O^{+7} from both models.

Of those spectra that were fitted by both models, the difference in χ^2 was insignificant. To decide which model to use, I looked at the solar wind proton properties when O^{+6} ions were seen (Figures 4.2 and 4.3) and found that most of the O^{+6} data comes from high density plasma streams. Since the ion collision rate is proportional to the ion density [*NRL plasma Formulary*, 1986], and the minor ion data resulted from high density plasma streams, I expected the ions to be in thermal equilibrium from Coulomb collisions. With this expectation I plotted the alpha particle thermal speed $w_{He^{+2}}$ against the proton thermal speed w_{H^+} when O^{+6} was detected and fitted without the presence of other minor ions. As shown in Figure 4.6, $w_{He^{+2}} \approx 0.5 w_{H^+}$. Since the H^+ and He^{+2} ions were at the same temperature, I assumed that the O^{+6} and other minor ions were at the same temperature as the He^{+2} ions. This assumption was supported by data from *Bochsler et al.* [1985]. Although their data indicated that in general the O^{+6} temperature is 4 times the He^{+2} temperature, at low He^{+2} speeds ($< \sim 450$ kms $^{-1}$) there is a subset of the data in which O^{+6} temperatures approach the He^{+2} temperatures [cf. *Bochsler et al.*, 1985, Figure 6]. I therefore decided to use the equal-temperature model.

4.6. Results from the Equal Temperature Model

4.6.1. Flux Densities

The use of additional minor ions allowed an accurate determination of the number densities for both O^{+6} and O^{+7} which can be used to derive the corresponding flux densities for these ions. When the sum of O^{+6} and O^{+7} flux densities (which represents the total oxygen flux density) is plotted against that of He^{+2}, one can see that while the ISEE data show a linear relation between the flux densities of O and He^{+2}, the combined Voyager data exhibit a relation between the He^{+2} and the O flux densities that differs from the one derived the ISEE 3 data (see Figure 4.7). Each panel shows the results from the two spacecraft that have been combined by calendar year. The inclined broken lines indicate constant He^{+2} to O flux density ratios. Also shown within each panel is the average value of $[He^{+2}]/[O]$ for that year. The first value is for Voyager 1 and the second for Voyager 2. Note that except for 1978 the value of $[He^{+2}]/[O]$ for the two spacecraft is similar (the reason for the discrepancy is explained in the next section).

The fluxes from the ISEE 3 data are linearly related as follows

$$\log_{10}[\text{O flux}] = \log_{10}[He^{+2} \text{ flux}] - (1.88\pm0.12) \qquad (4.1)$$

while the Voyager fluxes are better represented by a power law relation of

$$\log_{10}[\text{O flux}] = (0.65\pm0.03)\log_{10}[He^{+2} \text{ flux}] + (2.11\pm0.28) \qquad (4.2a)$$

$$\log_{10}[\text{O flux}] = (0.73\pm0.02)\log_{10}[He^{+2} \text{ flux}] + (1.25\pm0.19) \qquad (4.2b)$$
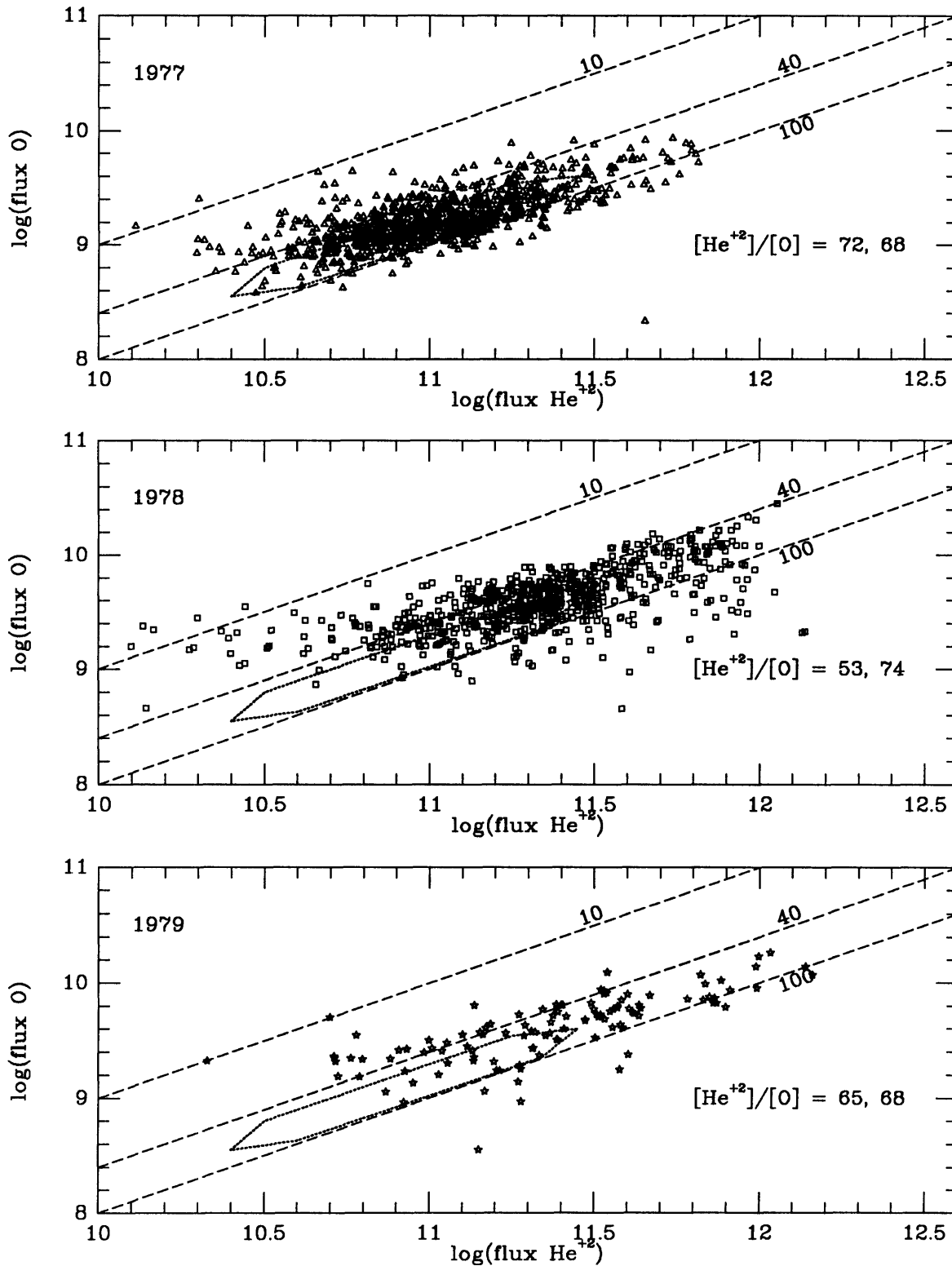
for Voyager 1 and Voyager 2 respectively.

Figure 4.7. O Flux density vs He^{+2}. Polygonal region contains the findings of Bochsler and Geiss.

92

There are four items of note in these results: (1) both the O flux density and the He^{+2} flux density span about two orders of magnitude, (2) unlike the *Bochsler et al.* [1985] results, the Voyager data do not cluster around a line of constant flux ratio[11], (3) despite the difference in their slopes, much of the Voyager data lie in the same region as the data of *Bochsler et al.* [1986], and (4) there seems to be less He^{+2} relative to O at low fluxes. The relatively low amounts of He^{+2} at low fluxes could be due to either problems with the determination of the O^{+6} flux at these low levels or to less effective Coulomb drag (a full discussion of this phenomenon is beyond the scope of this thesis). However, from visual inspection of the ion spectra, I believe that the O values are valid even at low flux values.

I was able to used the ratio of the O^{+6} and O^{+7} densities to determine the temperature of the solar corona by assuming that the steady state corona is determined by the balance of electron impact and radiative and dielectronic recombination [*Shull and van Steenberg*, 1982]. I find an average ratio $[He^{+2}]/[O]$ from the Voyager data to be 66 ± 7 for Voyager 1 and 71 ± 17 for Voyager 2, based upon the 637 and 1053 determinations from Voyager 1 and 2, respectively. For both Voyager spacecraft the average coronal temperature obtained from the ratio $[O^{+7}]/[O^{+6}]$) is $(1.7 \pm 0.1) \times 10^6$ K, the same as the 1.67×10^6 K assumed in the analysis of the ISEE 3 data [*Bochsler et al.*, 1985; *Bochsler and Geiss*, 1990].

---

11 I have since learned that the fit to the ISEE 3 data was performed under the constraint that the O and He^{+2} flux densities (not their logarithms) were linearly related. If this constraint were relaxed then the relationship between the flux densities would be a power law with exponent ~0.80 [*P. Bochsler*, private communication, 1992].
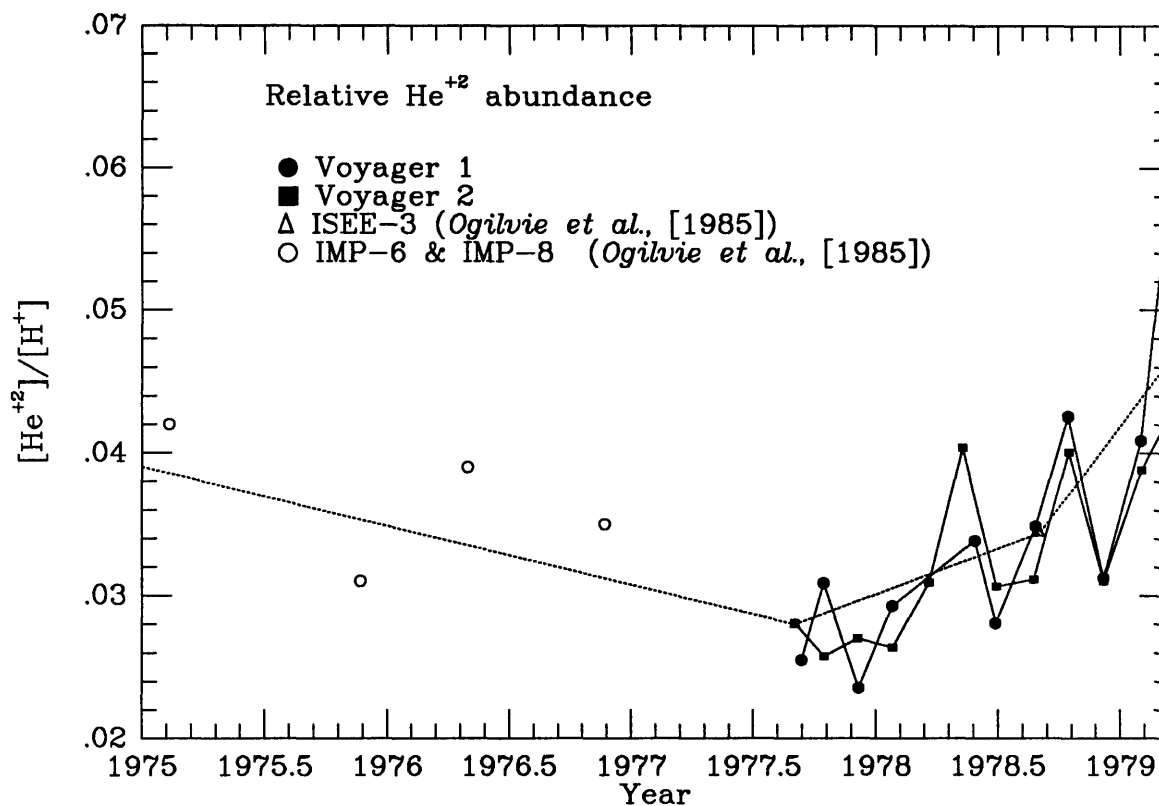
Figure 4.8. He^{+2} abundance from 1975 to early 1979.

4.6.2. Temporal Variations

I have also looked at the temporal variation of the ratios [He^{+2}]/[H^{+}], [H^{+}]/[O], and [He^{+2}]/[O]. In Figure 4.8 I show a plot adapted from *Ogilvie et al.* [1989] of the ratio [He^{+2}]/[H^{+}] from 1977 to early 1979 displaying data from various spacecraft. The results from ISEE 3 are indicated by triangles, and those for IMP 6 and IMP 8 are shown by the open circles. The results from this study are shown by solid circles (Voyager 1) and solid squares (Voyager 2). The error bars are too small to show on the plot. The dashed line is a hand drawn "best fit" line. There are two points to note: (1) from the time of the Voyager launches (September 5, 1977 for Voyager 1

94

and August 20, 1977 Voyager 2) through the first 52 days of 1979, the Voyager 1, Voyager 2, and ISEE 3 ratios are consistent with each other, and (2) Figure 4.8 shows that the ratio $[He^{+2}]/[H^+]$ went through a minimum of ~0.03 in 1977 and rose sharply to ~0.05 in 1978 and 1979, in conjunction with increasing sunspot numbers.

To assess the possibility of temporal variation of the oxygen content of the solar wind, I show in Figure 4.9 the ratios $[H^+]/[O]$ and $[He^{+2}]/[O]$. Average values from the two spacecraft track each other quite well through the beginning of 1979. The ratio $[H^+]/[O]$ declines from late 1977 to about mid-1978. The ratio then rises and reaches a peak in late 1978, after which the ratio declines again. The overall trend of the ratio $[He^{+2}]/[O]$ is fairly constant with the Voyager 2 data showing an abrupt rise and fall in 1978. The peaks mentioned in the previous paragraph arise from density enhancements of H^+ and He^{+2}. In the case of the plot of $[H^+]/[O]$, on day 265 of 1978, Voyager 2 recorded a tenfold increase in proton density. There was no corresponding increase in He^{+2} or O density for about five hours. This increased proton density contributed to the abnormally high value of the 52-day averages of $[H^+]/[O]$ shown in Figure 4.9. There is no correspondingly high value in the $[H^+]/[O]$ 52-day averages from the Voyager 1 data, because only the very beginning of the proton density enhancement was recorded. The rest of the event was lost due to a tracking gap.

The very large value in the 52-day averages of the Voyager 2 52-day averages of $[He^{+2}]/[O]$, arises from a fourfold increase in He^{+2} density on day 113 of 1978. The corresponding increase in oxygen density occurs about 10 hours later (for reasons that are unclear at this time). There is large increase in H^+ density accompanying the He^{+2}
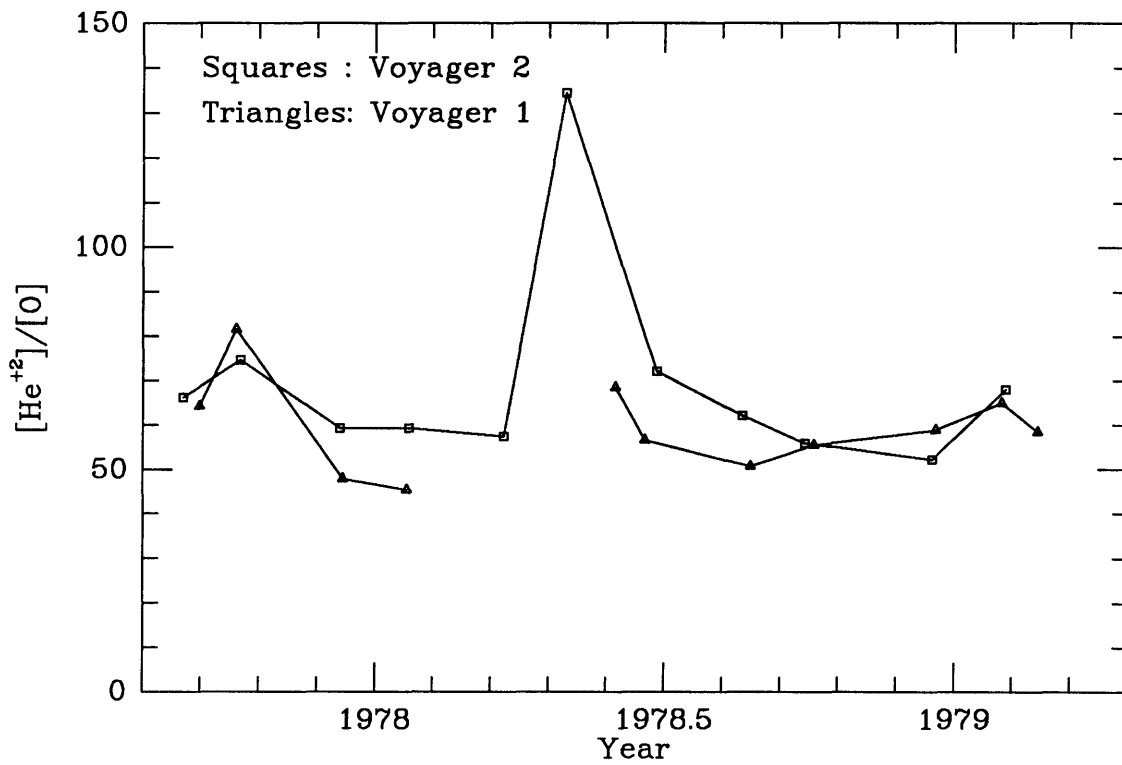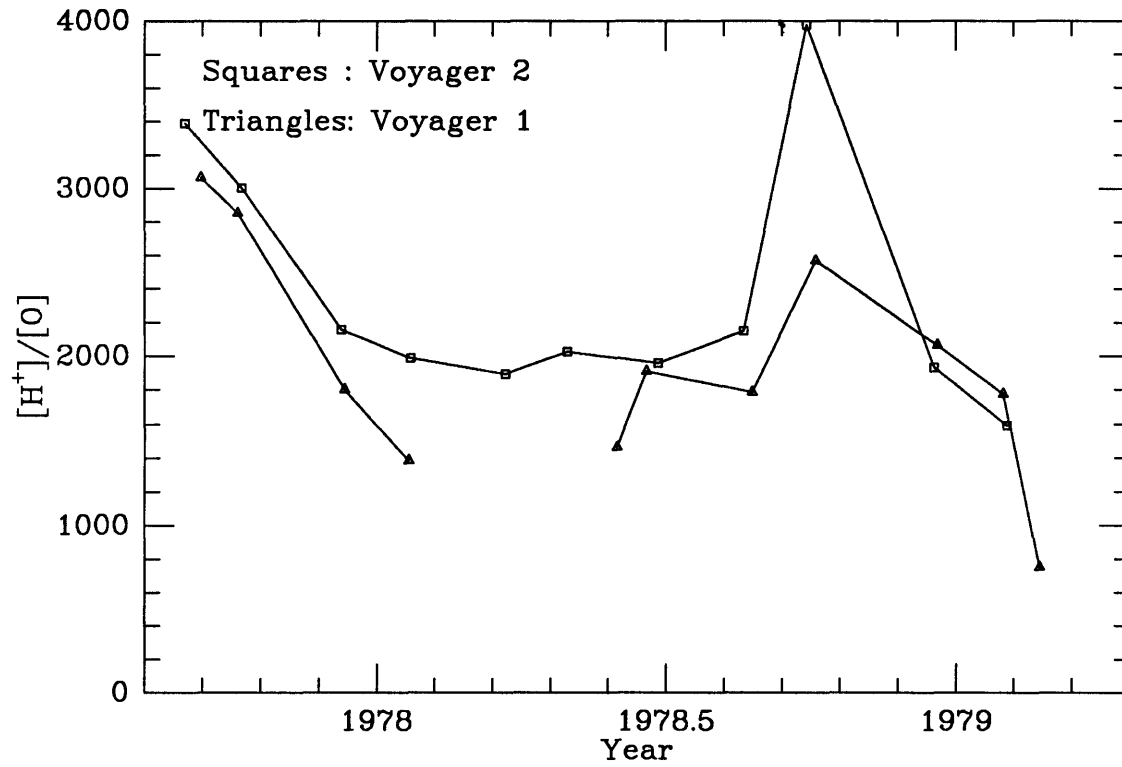
Figure 4.9. [H]/[O] and [He^{+2}]/[O] ratios from 1977 to 1979.

density enhancement. Any increase in He^{+2} density that might have been observed near day 113 by Voyager 1 has been lost due to problems with the PLS instrument. This enhancement of He^{+2} number density explains the large difference in the average value of $[He^{+2}]/[O]$ for Voyagers 1 and 2 (in 1978) as shown in Figure 4.7.

4.7. Conclusions

On the basis of 1690 spectra, I found the average number density ratio $[He^{+2}]/[O]$ to be 66 ± 7 for Voyager 1 and 71 ± 17 for Voyager 2 (based on 637 and 1053 spectra respectively) during the period between late 1977 and early 1979. These results are consistent with the average ratio $[He^{+2}]/[O] = 75 \pm 20$ obtained from ISEE 3 for the period 1978 to 1982 [*Bochsler et al.*, [1985]). I also found an average coronal temperature (determined from the ratio $[O^{+7}]/[O^{+6}]$) of $(1.7 \pm 0.1) \times 10^6$ K. This temperature is the same as that assumed by Bochsler et al. in their ion model.

However, for the Voyager data I see a different relation between the He^{+2} and the O flux densities from the one derived the ISEE 3 data. The ISSE 3 data suggest that the O flux density is proportional to the He^{+2} flux density, whereas the results from the Voyager data indicate that the O flux density and the He^{+2} flux density are related by a power law. Clearly more work needs to be done in the identification of oxygen in the Voyager ion spectra and the subsequent analysis of said spectra.

It is possible that these flux relations are the result of the bulk of the O observations coming from cold (Mach number ≥ ~15), high-density low-speed plasma streams. In low-speed streams the ions would tend to be in thermal equilibrium (see discussion)

97

which would make the equal-temperature

4.8. Description of Starting Values for Six Minor Ion Fit

To obtain the starting values for the fit parameters, the program begins with the output

values from the single ion fits (proton, alpha particle, and O^{+6}). The starting He^{+2}

density, velocity, and thermal speed are taken as the output values from the alpha par-

ticle fit. The starting O^{+6} velocity is taken as the output velocity from the O^{+6} fit. The

starting O^{+6} thermal speed is taken to be one half the He^{+2} thermal speed. This choice

of thermal speed caused me to chose a starting O^{+6} density equal to one half the out-

put density generated by the O^{+6} fit.

The starting velocities and thermal speeds for the other minor ions are set equal to the

O^{+6} starting velocity and thermal speed. The starting densities are chosen to conform

to a coronal temperature of 1.6×10^6 K and a solar wind composition of: $[C] = [C^{+4}]$ +

$[C^{+5}] = 0.63[O]$; $[N] = [N^{+5}] + [N^{+6}] = 0.13[O]$; $[Ne^{+8}] = 0.15[O]$, and $[O] = [O^{+6}]$ +

$[O^{+7}]$. The relative abundances of the various ions were computed from the tables of

Shull and van Steenberg [1982]. The minor ion densities were not held fixed, but

were allowed to vary as independent parameters.

98

REFERENCES

Bai, T., and P. A. Sturrock, The 152-day periodicity of the solar occurrence rate, *Nature, 327*, 601-604, 1992.

Bai, T., and P. A. Sturrock, The 154-day and related periodicities of solar activity as subharmonics of a fundamental period, *Nature, 350*, 141-142, 1991.

Bai, T., and E. W. Cliver, A 154 day periodicity in the occurrence rate of proton flares *Astrophys. J., 363*, 299-309, 1990.

Bame, S. J., Solar wind minor ions - Recent observations, Solar Wind Five, edited by M. Neugebauer, *NASA Conf. Publ., 2280*, 573-589, 1983.

Bame, S. J., A. J. Hundhausen, J. R. Asbridge, and I. B. Strong, Solar wind ion composition, *Phys. Rev. Lett., 20*, 393-395, 1968.

Bame, S. J., J. R. Asbridge, A. J. Hundhausen, and M. D. Montgomery, Solar wind ions: $^{56}Fe^{+8}$ to $^{56}Fe^{+12}$, $^{28}Si^{+7}$, $^{28}Si^{+8}$, $^{28}Si^{+9}$, $^{16}O^{+6}$, *J. Geophys. Res., 75*, 6360-6365, 1970.

Barnes, A., Acceleration of the solar wind, *Reviews of Geophys., 30*, 43-55, 1992

Barnett, A., and S. Olbert, The response function of modulator grid Faraday cup plasma instruments, *Rev. Sci. Instrum., 57*, 2432-2440, 1986.

Bochsler, P., Velocity and abundance of silicon ions in the solar wind, *J. Geophys. Res., 94*, 2365-2373, 1989.

Bochsler, P., and J. Geiss, Composition of the solar wind, in *Solar System Plasma Physics, Geophys. Monogr. Ser.*, vol. 54, edited by J. H. Waite, Jr., J. L. Burch, and R. L. Moore, pp. 133-141, AGU, Washington, D.C., 1990.

Bochsler, P., J. Geiss, and R. Joos, Kinetic temperatures of heavy ions in the solar wind, *J. Geophys. Res.*, *90*, 10,779-10,789, 1985.

Bochsler, P., J. Geiss, and S. Kunz, Abundances of carbon, oxygen, and neon in the solar wind during the period from August 1978 to June 1982, *Solar Phys.*, *103*, 177-201, 1986.

Book, D. L., Revised and enlarged collection of plasma physics formulas and data, *NRL Memo. Rep.*, *3322*, 1986.

Bridge, H. S., J. W. Belcher, R. J. Butler, A. J. Lazarus, A. M. Mavretic, J. D. Sullivan, G. L. Siscoe, and V. M. Vasyliunas, The plasma experiment on the 1977 Voyager mission, *Space Sci. Rev.*, *21*, 259–287, 1977.

Coplan, M. A., K. W. Ogilvie, P. A. Bochsler, and J. Geiss, Ion composition experiment, *IEEE Trans. Geos. Electr.*, *GE-16*, 185-191, 1978. Donnelly, R. F. and L. C. Puga, Thirteen-day periodicity and the center-to-limb dependence of UV, EUV, and X-ray emission of solar activity, *Sol. Phys.*, *130*, 369-390, 1990.

Feldman, W. C., J. T. Gosling, D. J. McComas, and J. L. Phillips, Evidence for ion jets in the high-speed solar wind, *J. Geophys. Res.*, *98*, 5593-5605, 1993.

Feldman, W. C., J. R. Asbridge, S. J. Bame, and J. T. Gosling, Long-term variations of selected solar wind properties: Imp 6, 7 and 8 results, *J. Geophys. Res.*, *83*, 2177-2189, 1978.

Gabriel, S., R. Evans, and J. Feynman, Periodicities in the occurrence rate of solar

proton events, *Sol. Phys., 128*, 415-422, 1990.

Gazis, P. R., Observations of plasma bulk parameters and the energy balance of the solar wind between 1 and 10 AU, *J. Geophys. Res., 89*, 775-785, 1984.

Gazis, P. R., J. D. Mihalov, A. Barnes, A. J. Lazarus, and E. J. Smith, Pioneer and Voyager observations of the solar wind at large heliocentric distances and latitudes, *Geophys. Res. Lett., 16*, 223-226, 1989.

Gloeckler, G., J. Geiss, H. Balsiger, P. Bedini, J. C. Cain, J. Fischer, L. A. Fisk, A. B. Galvin, F. Gliem, D. C. Hamilton, J. V. Hollweg, F. M. Ipavich, R. Joos, S. Livi, R. Lundgren, U. Mall, J. F. McKenzie, K. W. Ogilvie, F. Ottens, W. Rieck, E. O. Tums, R. von Steiger, W. Weiss, and B. Wilken, The solar wind ion composition spectrometer, *Astron. Astrophys. Suppl. Ser., 92*, 267-289, 1992.

Hundhausen, A. J., Sizes and locations of coronal mass ejections: SMM observations from 1980 and 1984-1989. *J. Geophys. Res., 98*, 13,777, 1993.

Hundhausen, A. J., *Coronal Expansion and the Solar Wind*, Springer-Verlag, New York, 1972.

Horne, J. H. and S. L. Baliunas, A prescription for period analysis of enequally sampled time series, *Astrophys. J., 302*, 757-763, 1986.

Ipavich, F. M., A. B. Galvin, G. Gloeckler, D. Hovestadt, S. J. Bame, B. Klecker, M. Scholer, L. A. Fisk, and C. Y. Fan, Solar wind Fe and CNO measurements in high-speed flows, *J. Geophys. Res., 91*, 4133-4141, 1986.

Kendall, M. G., *The Advanced Theory of Statistics. Vol II*, Charles Griffen & Co., Ltd, London, 1955.

Levi, S. and E. Marsch, Generation of solar wind tails and double beams by

coulomb collisions, *J. Geophys. Res., 92*, 7255-7261, 1987.

Lomb, N. R., *Astrophys. J., 39*, 447, 1976.

Marsch, E., K.-H. Muhlhauser, H. Rosenbauer, R. Schwenn, and F. M. Neubauer, Solar wind ions: observations of the Helios solar probes between 0.3 and 1 AU, *J. Geophys. Res., 87*, 35-51, 1982.

Neugebauer, M. and C. W. Snyder, Mariner 2 observations of the solar wind, 1, average properties, *J. Geophys. Res., 71*, 4469-4484, 1966.

Ogilvie, K. W., J. Geiss, and G. Gloeckler, High-velocity tails on the velocity distribution of solar wind ions, *J. Geophys. Res., 87*, 3605, 1993.

Ogilvie, K. W., M. A. Coplan, P. Bochsler, and J. Geiss, Solar wind observations with the ion composition instrument aboard the ISEE 3/ICE spacecraft, *Sol. Phys., 124*, 167, 1989.

Ogilvie, K.W., Analysis of O^{+7}/O^{+6} observations in the solar wind, *J. Geophys. Res., 90*, 9881-9884, 1985.

Ogilvie, K. W., M. A. Coplan, and R. D. Zwickl, Helium, hydrogen, and oxygen velocities observed on ISEE 3, *J. Geophys. Res., 87*, 7363-7369, 1982.

Ogilvie, K. W., P. Bochsler, J. Geiss, and M. A. Coplan Observations of the velocity distributions of solar wind ions, *J. Geophys. Res., 86* 6069-6074, 1980.

Pap, J., W. K. Tobiska, and S. D. Bower, Periodicities of solar irradiance and solar activity indices, I, *Sol. Phys., 129*, 165-189, 1990.

Richardson, J. D., J. W. Belcher, K. I. Paularena, and A. J. Lazarus, Solar wind oscillations with a 1.3 year period, *submitted to J. Geophys. Res.*, 1994.

Rohatgi, V. K., *Statistical Inference*, Wiley, New York NY, 1984.

Scargle, J., Studies in astronomical time series analysis II. Statistical aspects of spectral analysis of unevenly spaced data, *Astrophys. J.*, *263*, 835-853, 1982.

Schmid, J., P. Bochsler, and J. Geiss, Velocity of iron ions in the solar wind, *J. Geophys. Res.*, *92*, 9901-9906, 1987.

Shull, J. M., and van Steenberg, The ionization equilibrium of astrophysically abundant elements, *Astrophys. J. Suppl.*, *48*, 95, 1982.

The Astronimcal Almanac for the Year 1994, U.S. Govt. Printing Office, 1993.

Sonett, C. P., M. S. Giampapa, and M.S. Matthews, ed., *The Sun in Time*, The University of Arizona Press, Tuscon, 1991.

Vasyliunas, V. M., Deep space plasma measurements, *Methods of Experimental Physics*, edited by R. H. Lovbergs, *Methods of Exp. Phys.*, *9B*, 49-88, Academic Press Inc., New York NY, 1971.

Wolff, C. L. and W. R. Hoegy, Periodic solar EUV flux monitored near Venus *Sol. Phys.*, *123*, 7-20, 1989.

Zwickl, R. D., J. R. Asbridge, S. J. Bame, W. C. Feldman, and J. T. Gosling, He^+ and other unusual ions in the solar wind: A systematic search covering 1972-1980, *J. Geophys. Res.*, *87*, 7379-7388, 1982.